CFD ANALYSIS OF MISSILE SHROUD SEPARATION

A THESIS SUBMITTED TO
THE GRADUATE SCHOOL OF NATURAL AND APPLIED SCIENCES
OF
MIDDLE EAST TECHNICAL UNIVERSITY

BY

HASAN ERKAN ÇELİKER

IN PARTIAL FULFILLMENT OF THE REQUIREMENTS
FOR
THE DEGREE OF MASTER OF SCIENCE
IN
AEROSPACE ENGINEERING

FEBRUARY 2015

Approval of the thesis

CFD ANALYSIS OF MISSILE SHROUD SEPARATION

submitted by **HASAN ERKAN ÇELİKER** in partial fulfillment of the requirements for the degree of **Master of Science in Aerospace Engineering Department, Middle East Technical University** by**,**

Prof. Dr. Gülbin Dural Ünver
Dean, Graduate School of **Natural and Applied Sciences**

Prof. Dr. Ozan Tekinalp
Head of Department, **Aerospace Engineering**

Assoc. Prof. Dr. Sinan Eyi
Supervisor, **Aerospace Engineering Dept., METU**

Examining Committee Members:

Prof. Dr. Nafiz Alemdaroğlu
Aerospace Engineering Dept., METU

Assoc. Prof. Dr. Sinan Eyi
Aerospace Engineering Dept., METU

Prof. Dr. Serkan Özgen
Aerospace Engineering Dept., METU

Assoc. Prof. Dr. Oğuz Uzol
Aerospace Engineering Dept., METU

Emrah Gülay, M.Sc.
Senior Engineer, ROKETSAN

Date: 05/02/2015

I hereby declare that all the information in this document has been obtained and presented in accordance with academic rules and ethical conduct. I also declare that, as required by these rules and conduct, I have fully cited and referenced all material and results that are not original to this work.

Name, Last name : Hasan Erkan ÇELİKER

Signature :

ABSTRACT

CFD ANALYSIS OF MISSILE SHROUD SEPARATION

Çeliker, Hasan Erkan
M.S., Department of Aerospace Engineering
Supervisor: Assoc. Prof. Dr. Sinan Eyi

February 2015, 90 Pages

In this thesis, shroud separation on generic missile is performed by using the Computational Fluid Dynamics (CFD). This study is divided into two main parts. In the first part, aerodynamic coefficients of generic missile are calculated and store separation is performed. Additionally, the numerical analyses results are compared respectively with the experimental results in order to validate of CFD analyses method. Three-dimensional steady/unsteady Navier-Stokes equations are solved and three different turbulence models which are one-equation Spalart-Allmaras, two-equation Realizable k-ε, and two-equation k-ω SST methods are used. Aerodynamic coefficients results are validated with a HB generic missile and multi body dynamic simulation is validated with an EGLIN store separation test case by using Chimera grid method. Aerodynamic coefficients and store position/angle changes results are compared with experimental data respectively and all of them are in good agreement. As a result of all this validation, in the second part, a parametric study for shroud separations on generic missile is carried out in order to investigate altitude, Mach number, angle of attack, side-slip angle and ejection moment effects during the separation, and results of CFD simulation are presented.

Keywords: Computational Fluid Dynamics, Shroud Separation, Store Separation, Aerodynamic Coefficients, Multi Body Dynamic Simulation, Chimera Grid, CFD++

ÖZ

FÜZE AERODİNAMİK ÖRTÜ AYRILMASINA YÖNELİK YAPILAN HAD ANALİZLERİ

Çeliker, Hasan Erkan
Yüksek Lisans, Havacılık ve Uzay Mühendisliği Bölümü
Tez Yöneticisi: Doç. Dr. Sinan Eyi

Şubat 2015, 90 Sayfa

Bu tezde, Hesaplamalı Akışkanlar Dinamiği (HAD) kullanılarak jenerik füze üzerinden aerodinamik örtü ayrılması gerçekleştirilmiştir. Bu çalışma iki ana konuya ayrılmıştır. Çalışmanın ilk kısmında jenerik füzenin aerodinamik katsayıları hesaplanmış, harici yük ayrılması yapılmıştır. Çalışmada kullanılan sayısal yöntemlerin doğrulanması için sırasıyla analiz sonuçları deney verileriyle karşılaştırılmıştır. Üç boyutlu zamandan bağımsız/bağlı Navier-Stokes denklemleri çözülmüş ve üç farklı türbülans modeli (bir denklemli Spalart-Allmaras, iki denklemli Realizable k-ε ve iki denklemli k-ω SST metotları) denenmiştir. Aerodinamik katsayı sonuçları HB jenerik füze analiziyle doğrulanmıştır. Çoklu gövde dinamik analizleri ise Chimera çözüm ağı kullanılarak EGLIN harici yük ayrılması denek taşı ile doğrulanmıştır. Sırasıyla aerodinamik katsayılar ve harici yük konum/açı değişimleri deney verileriyle karşılaştırılmış, bütün değerler için birbiriyle örtüşen sonuçlar elde edilmiştir. Bütün bu doğrulamalar sonucunda tezin ikinci kısmında ise jenerik füze üzerinden aerodinamik örtü ayrılması sırasında, irtifanın, Mach sayısının, hücum açısının, yanal sapma açısının ve uygulanan ayrılma momentinin ayrılmaya etkisi parametrik çalışmayla incelenmiş ve analiz sonuçları gösterilmiştir.

Anahtar Kelimeler: Hesaplamalı Akışkanlar Dinamiği, Aerodinamik Örtü Ayrılması Harici Yük Ayrılması, Aerodinamik Katsayılar, Çoklu Gövde Dinamik Simülasyonu, Chimera Çözüm Ağı, CFD++

To My Family

ACKNOWLEDGEMENTS

I wish my deepest gratitude to my supervisor Assoc. Prof. Dr. Sinan Eyi for his guidance, advice, criticism and encouragements throughout the thesis.

I am very thankful to my parents Mrs. Zeynep Çeliker, Mr. Muhammed Çeliker for their love, help and motivation. Without them this work would not be completed.

I want to express my best wishes to Mr. Kıvanç Arslan, Mr. Tuğrul Aydemir, Mr. Adem Candaş and Mr. Ozan Göker for their friendship and support during this study.

I also wish to thank my manager Mr. Ali Akgül for his guidance and support during this study. I also would like to thank my colleagues in Aerodynamics Department of ROKETSAN for all their help and support during the thesis.

I finally would like to thank anyone who has supported my thesis effort in any way.

TABLE OF CONTENTS

LIST OF FIGURES

FIGURES

LIST OF TABLES

TABLES

CHAPTER 1

INTRODUCTION

Missiles have higher speed, altitude and maneuvering capability compared to the airplanes. These increased performance parameters may introduce new aerodynamic problems which are aerodynamic heating, higher dynamic pressures, higher maneuvering accelerations, operating in the non-linear region of high angle of attacks, etc. Due to the requirements of different mission, various types of missiles are designed to compensate arising aerodynamic related problems. Especially air-to-air missiles are designed to operate at high Mach numbers. At these flow regimes, the missile’s nose is exposed to significant aerodynamic heating, and it can cause ablation phenomena and damage the electronics inside the body. Therefore, using an additional front cover to protect the missile’s nose and its separation during the flight are important topics particularly for air-to-air and /surface-to-air (due to high flight velocity) type missiles. Missile classification is given briefly in the following part.

1.1 Classification of Missiles

Type of guidance system, propulsion system, launching and impact, trajectory and, trim and control device can be used for classifying the missiles. The points of launching and impact classify the missiles in five groups:

AAM	Air-to-air missile
ASM	Air-to-surface missile
SAM	Surface-to-air missile
SSM	Surface-to-surface missile
UUM	Underwater-to-underwater missile

1.1.1 Air-to-Air Missiles (AAM)

Air-to-Air Missiles (AAM) are fired from an aircraft to another one. Small payload carrying capacity, relatively short range and high maneuverability requirement are the general characteristics of the AAM. Long and thin cylinders structure reduces the cross sectional area of the AAM, so drag force can be decreased. The flight time is relatively short because the missile can reach high supersonic speeds.

1.1.2 Air-to-Surface Missiles (ASM)

Air-to-Surface Missiles (ASM) are mounted on bombers, attack aircraft, fighter aircraft etc. for destroying land or sea targets which are near or hundreds kilometers away. Maneuverability requirement is low. ASMs operate at subsonic or transonic speeds depending on the requirements.

1.1.3 Surface-to-Air Missiles (SAM)

Surface-to-Air Missiles (SAM) are used for destroying aircraft, helicopters or, other missiles from the ground. It can be used in both short and long ranges. Ramjet or other air breathing power plants are used in long range missiles to reduce the weight. SAMs are suitable for air defense against the high speed threats because of their maneuverability and high speed requirements.

1.1.4 Surface-to-Surface Missiles (SSM)

Surface-to-Surface Missiles (SSM) are fired from a sea or land based platform to attack another sea or land units. For example ballistic missiles and artillery batteries are called as SSM. Hand-held, vehicle mounted systems or fixed installations options are available for firing the SSMs. Maneuverability requirement is relatively weak. While they are effective in long range as offensive purpose, at short range they are used for supporting the ground units. The fin and/or wing are usually used lifting and providing stability.

1.1.5 Underwater-to-Underwater Missiles (UUM)

Underwater-to-Underwater Missiles (UUM) are fired from one submerged submarine, they travel at high speeds to the area of the distant submarine, and then delivers an antisubmarine payload usually a torpedo. It creates an underwater bubble in which it could travel under rocket power, at speeds greatly faster than a torpedo.

1.2 Missile with Shroud

Many flight vehicles and in particular air-to-air missiles are designed to operate at supersonic velocities. At these flow regimes, the missile's nose is exposed to significant aerodynamic heating, and it is common to use an additional front cover to protect the payload from these hostile conditions. Moreover, a typical seeker configuration requires a blunt nose if expensive transparent materials required for the seeker lens are avoided. The wave drag on the nose makes a significant effect on the range of missile (for a given thrust and fuel weight), the nose design of medium to long range air-to-air missiles is traditionally optimized for low drag [1]**.**

To further emphasize this point; until the missile seeker is locked on target, removable shrouds can be used to cover the sensitive parts of the seeker system. Avoiding aerodynamic drag force and protecting of the seeker against aerodynamic heating effects at midcourse phase are the essential advantages of the shroud concept [2]**.**

1.3 Aim of Thesis

Accurate prediction of missile shroud separation trajectory is important for shroud design since an unsuccessful separation may damage the missile and lead to a catastrophic failure. Originally these trajectory predictions are made by using wind tunnel and flight tests. However, high cost and complexity seen in free flight and wind tunnel testing lead the missile designers to find faster and reliable methods. For this aim, with the increasing computer technology, researches have been concentrated on numerical methods of multi body dynamic simulations where the motivation of the thesis comes from. In order to solve multi body dynamic problem CFD++ solver is used. Computational analysis is performed in reasonable time by using parallel computer clusters. The applied engineering approach was validated using EGLIN Store Separation test case [3] and HB test case [4]. The results were compared with reference studies. After validating the method, shroud separation analyses for a generic missile configuration was performed.

The aim the thesis is to investigate the effects of different parameters such as altitude, Mach number, angle of attack, side-slip angle and ejection moment on the safe separation of shroud from a generic missile.

1.4 Literature Survey

Various missiles in service and next-generation missile systems use the advantages of modern infra-red seekers. One drawback of IR-systems is their limitation due to the aerodynamic heating of missiles at high supersonic speed. Constant heat transfer and high recovery temperatures can be dangerous for the seeker. According to Oswald et al. [2] this issue can be handled, when the missile seeker is protected with shrouds. The shrouds cover the seeker while providing lower aerodynamic drag. The shroud leaves from the missiles at the homing phase. Defining the release vector to eject the shrouds is the significant problem for engineer to make safer the shroud separation process. For this purpose, they performed three dimensional CFD simulations under free-flight flow conditions. Predefined force vector is applied on the center of gravity of the shroud before the releasing time. Separating of the shroud from the missile comes after the releasing, so CFD grid has to be adapted because of the free motion of the shroud.

A shroud is used to protect the payload on the ground and during launch from external environments. The original Polaris shroud, used for STARS I flights, uses a single circumferential base separation system, which requires complex, energy absorbing maneuvers to accomplish separation. Whalley [5] developed a bi-sector shroud in which the two halves are effected perpendicular to the flight path in order to increase STARS II launch vehicle capability. The shroud consists of a base ring machined from aluminum alloy, two bi-sectors that use Kevlar/epoxy and graphite/epoxy laminate construction, and a Teflon nose cap. The two bi-sectors are joined longitudinally by two thrusting separation rails and the external surface of the shroud is coated with an ablative heat shield to maintain the structure at an acceptable temperature.

Hypersonic interceptors require a removable shroud to protect the vital seeker components from the extreme heating loads of the fly-out environment and to provide a more aerodynamic shape for the vehicle in the lower atmosphere. Panetta et al. [6] designed self-contained shroud jettison devices in order to remove a shroud prior to the commencement of end-game activities by applying forces to the shroud in a passive or active manner. These forces cause the shroud petals to commence separation and move away from the vehicle. They have demonstrated a number of jettison techniques. Each design is dependent on the aerodynamic forces acting on the shroud and the physical constraints of the vehicle. For example, pneumatic/hydraulic systems are generally reserved for exo-atmospheric deployments. Pyrotechnics are used to separate a portion of the shroud (nose-tip, hinge, split-line, etc.), and either contain the explosion in an inflatable bladder or utilize ram air to separate the shroud and relevant figure can be seen in Figure 1.1.

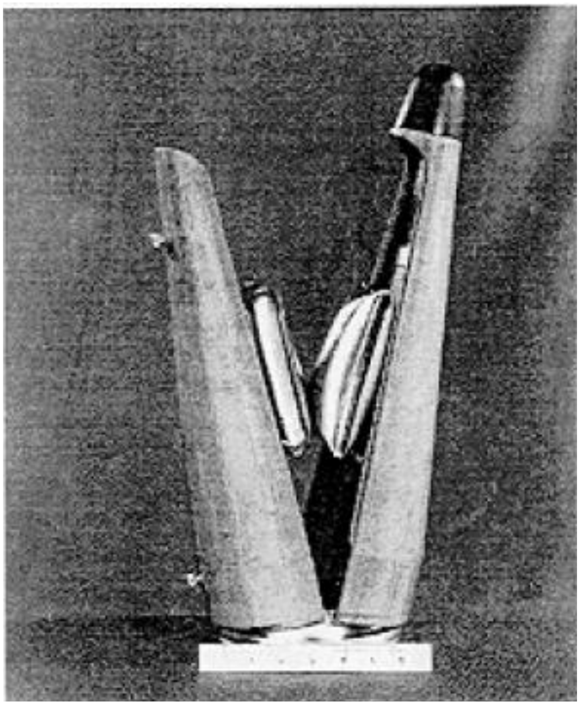

Figure 1.1 Inflatable Bladder for Shroud Separation [6]

Also according to Anandhanarayanan [7] shroud panels are attached to the vehicle through a hinge at the end of panels and they are opened using pyro mechanism to a small angle against the external aerodynamic forces. As the flow rushes through, the panels open up further due to the aerodynamic load. The panels should be detached at an optimum angle for safe separation from the launch vehicle and relevant figure can be seen in Figure 1.2.

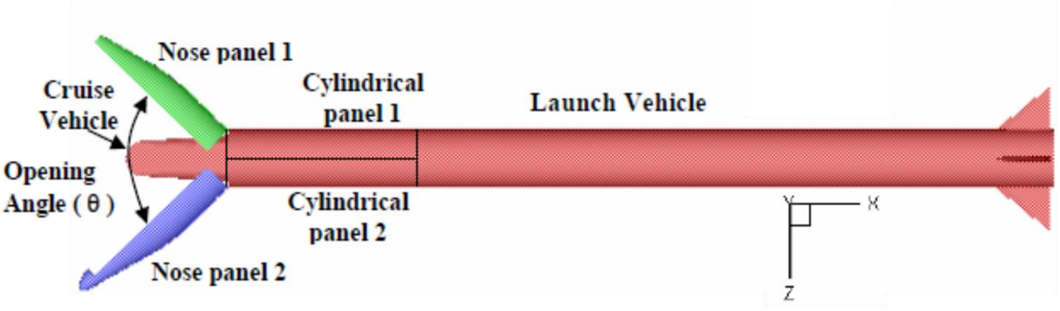

Figure 1.2 Launch Vehicle with Nose Panels [7]

It is necessary to estimate the minimum opening angle required to initiate the opening and the maximum angle at which the panels can be separated safely without hitting the launch vehicle. It is very difficult and expensive to simulate such separation studies through experiments. Therefore, he has carried out a CFD study in order to estimate the aerodynamic loads and moments acting on the nose panels at different opening angles.

The HEDI shroud design employs four petals, hinged at their base, and a two-piece nose cap. An ordnance device provides the energy to separate the two halves of the nose cap. As soon as the moment about the hinge due to the internal loads exceeds the moment about the hinge due to external loads, the petals separate from the interceptor. According to Lumb [8] shroud configurations tested included three and four petals design, 15 and 30 degree hinge release angles. Using the results the shroud design had become four petals with a split nose cap. The petals were oriented that the seam was above the sensor window. The hinges released after 30 degree of rotation in order to ensure safe separation.

The shroud system for the HEDI vehicle consisted of an aerodynamic shroud which covered the HEDI forebody. According to Resch et al. [9] the shroud was designed to impart no asymmetric loads to the vehicle during the separation process. The shroud petals were mounted to the forebody via a hinge ring assembly. The nose cap contained an explosive thruster which separated the nose cap into two sections and radially propelled each section away from the vehicle. The exposed cavity between the shroud petals and the forebody was then pressurized due to the dynamic pressures of the flow. The pressure differential across the petals caused the petals to pivot about the hinge ring and away from the forebody. After pivoting approximately 15 degrees, the four petals were released from the hinge ring and moved radially away from the forebody.

According to Cavallo and Dash [10] CFD predictions were performed to support test of the shroud deployment at hypersonic velocities in wind tunnel. While overset mesh Chimera methods have been the traditional approach for simulating such separation problems; they suggest that unstructured methods are more readily able to treat complex geometries and possess the additional advantage of being able to adapt to evolving flow features. Missile and separated shroud covers can be seen in Figure 1.3 that was used for CFD analysis.

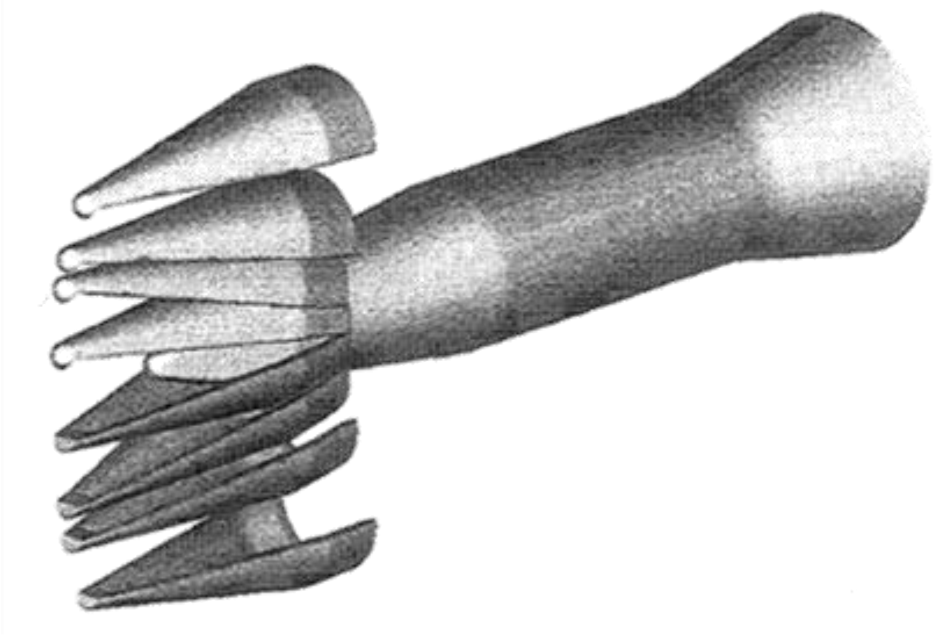

Figure 1.3 Missile with Shroud Covers [10]

CHAPTER 2

METHODOLOGY

Methodology used in the calculations of the numerical simulation is explained in this chapter. Firstly, governing equations of the fluid flow is given. After that, numerical tools and simulation procedures are discussed.

2.1 Governing Equations

In this study, compressible and steady/unsteady form of Reynolds-Averaged Navier-Stokes (RANS) equations are used. Several turbulence models are also examined.

2.1.1 Fluid Dynamics

In this problem, the solution domain consists of three domains; two inners and one outer. The inner domains are the moving domains and the outer domain is the stationary domain. In the non-inertial references frame, the integral forms of the equations are defined for all domains. These governing equations are given below [11].

Continuity:

$$\frac{\partial}{\partial t}\int_{\Omega}\rho d\Omega + \oint_{S}\rho\left(\vec{V} - \vec{V}_{C.V.}\right)\cdot d\vec{S} = 0 \tag{2.1}$$

Here,

$$\vec{V} = u\vec{\imath} + v\vec{\jmath} + w\vec{k} \tag{2.2}$$

$$\vec{V}_{C.V.} = u_{C.V.}\vec{\imath} + v_{C.V}\vec{\jmath} + w_{C.V.}\vec{k} \tag{2.3}$$

$\vec{V}$ is the fluid velocity, $\vec{V}_{C.V.}$ is the moving volume velocity, Ω and S are the surface enclosed to this finite volume.

Conservation of momentum:

$$\frac{\partial}{\partial t}\int_{\Omega}\rho\vec{V}d\Omega+\oint_{S}\left(\rho\vec{V}\otimes\vec{V}+P\bar{\bar{I}}-\rho\vec{V}\otimes\vec{V}_{C.V.}\right)\cdot d\vec{S}=\oint_{S}\tau_{ij}\cdot d\vec{S} \qquad (2.4)$$

Here, $\vec{V}\otimes\vec{V}$ is the tensor product, P is the pressure.

Conservation of energy:

$$\frac{\partial}{\partial t}\int_{\Omega}\rho E d\Omega+\oint_{S}\left(\rho E\vec{V}+P\vec{V}-\rho E\vec{V}_{C.V.}\right)\cdot d\vec{S}=\oint_{S}\left(\tau_{ij}\cdot\vec{V}-\dot{q}\right)\cdot d\vec{S} \qquad (2.5)$$

In Eq. (2.5) E is the total energy, $\dot{q}$ is the heat transfer rate $\tau_{ij}$is the viscous shear stress tensor defined as:

$$\tau_{ij}=\mu\left[\left(\partial_j V_i+\partial_i V_j\right)-\frac{2}{3}\left(\vec{\nabla}\cdot\vec{V}\right)\delta_{ij}\right] \qquad (2.6)$$

Integral Compact Form of Governing Equations

The suitable form of governing equations for finite volume method is given below.

$$\frac{\partial}{\partial t}\int_{\Omega}\vec{U}d\Omega+\oint_{S}\vec{F}\cdot d\vec{S}=\oint_{S}\vec{Q}\cdot d\vec{S} \qquad (2.7)$$

Where, $\vec{U}$ is the conservation variables, $\vec{F}$ is the convective flux and $\vec{Q}$ is the viscous diffusive flux vectors. These vectors are as follows:

$$\vec{U} = \begin{bmatrix} \rho \\ \rho u \\ \rho v \\ \rho w \\ \rho E \end{bmatrix}$$

$$\vec{F} = \begin{bmatrix} \rho\left(\vec{V} - \vec{V}_{C.V.}\right) \\ \left(\rho\vec{V} \otimes \vec{V} + P\bar{\bar{I}} - \rho\vec{V} \otimes \vec{V}_{C.V.}\right) \\ \left(\rho E\left(\vec{V} - \vec{V}_{C.V.}\right) + P\vec{V}\right) \end{bmatrix} \tag{2.8}$$

$$\vec{Q} = \begin{bmatrix} 0 \\ \tau_{ij} \\ \left(\tau_{ij} \cdot \vec{V} - \dot{q}\right) \end{bmatrix}$$

The convective flux vector $\vec{F}$can be defined as follows:

$$\vec{F} = F\vec{\imath} + G\vec{\jmath} + H\vec{k} \tag{2.9}$$

Where;

$$F = \begin{bmatrix} \rho(u - u_{C.V.}) \\ \rho u(u - u_{C.V.}) + p \\ \rho v(u - u_{C.V.}) \\ \rho w(u - u_{C.V.}) \\ (\rho E + p)(u - u_{C.V.}) + u_{C.V.}p \end{bmatrix}$$

$$G = \begin{bmatrix} \rho(v - v_{C.V.}) \\ \rho u(v - v_{C.V.}) \\ \rho v(v - v_{C.V.}) + p \\ \rho w(v - v_{C.V.}) \\ (\rho E + p)(v - v_{C.V.}) + v_{C.V.}p \end{bmatrix} \tag{2.10}$$

$$H = \begin{bmatrix} \rho(w - w_{C.V.}) \\ \rho u(w - w_{C.V.}) \\ \rho v(w - w_{C.V.}) \\ \rho w(w - w_{C.V.}) + p \\ (\rho E + p)(w - w_{C.V.}) + w_{C.V.}p \end{bmatrix}$$

The diffusive flux vector $\vec{Q}$ can be defined as follows:

$$\vec{Q} = \frac{M_\infty}{Re_L}\left(Q_x\vec{\imath} + Q_y\vec{\jmath} + Q_z\vec{k}\right) \tag{2.11}$$

Here;

$$\begin{gathered}
Q_x = \begin{bmatrix} 0 \\ \tau_{xx} \\ \tau_{xy} \\ \tau_{xz} \\ \tau_{xx}u + \tau_{xy}v + \tau_{xz}w + \dot{q}_x \end{bmatrix} \\
Q_y = \begin{bmatrix} 0 \\ \tau_{yx} \\ \tau_{yy} \\ \tau_{yz} \\ \tau_{yx}u + \tau_{yy}v + \tau_{yz}w + \dot{q}_y \end{bmatrix} \\
Q_x = \begin{bmatrix} 0 \\ \tau_{zx} \\ \tau_{zy} \\ \tau_{zz} \\ \tau_{zx}u + \tau_{zy}v + \tau_{zz}w + \dot{q}_z \end{bmatrix}
\end{gathered} \tag{2.12}$$

The viscous shear stress tensors are given below.

$$\begin{gathered}
\tau_{xx} = 2(\mu + \mu_t)\frac{\partial u}{\partial x} - \frac{2}{3}(\mu + \mu_t)\left(\frac{\partial u}{\partial x} + \frac{\partial v}{\partial y} + \frac{\partial w}{\partial z}\right) \\
\tau_{yy} = 2(\mu + \mu_t)\frac{\partial v}{\partial y} - \frac{2}{3}(\mu + \mu_t)\left(\frac{\partial u}{\partial x} + \frac{\partial v}{\partial y} + \frac{\partial w}{\partial z}\right) \\
\tau_{zz} = 2(\mu + \mu_t)\frac{\partial w}{\partial z} - \frac{2}{3}(\mu + \mu_t)\left(\frac{\partial u}{\partial x} + \frac{\partial v}{\partial y} + \frac{\partial w}{\partial z}\right) \\
\tau_{xy} = \tau_{yx} = (\mu + \mu_t)\left(\frac{\partial u}{\partial y} + \frac{\partial v}{\partial x}\right) \\
\tau_{xz} = \tau_{zx} = (\mu + \mu_t)\left(\frac{\partial u}{\partial z} + \frac{\partial w}{\partial x}\right) \\
\tau_{yz} = \tau_{zy} = (\mu + \mu_t)\left(\frac{\partial v}{\partial z} + \frac{\partial w}{\partial y}\right)
\end{gathered} \tag{2.13}$$

The heat conductions are given below.

$$\begin{aligned}\dot{q_x} &= -\frac{1}{(\gamma-1)}\left(\frac{\mu}{Pr}+\frac{\mu_t}{Pr_t}\right)\frac{\partial T}{\partial x}\\ \dot{q_y} &= -\frac{1}{(\gamma-1)}\left(\frac{\mu}{Pr}+\frac{\mu_t}{Pr_t}\right)\frac{\partial T}{\partial y}\\ \dot{q_z} &= -\frac{1}{(\gamma-1)}\left(\frac{\mu}{Pr}+\frac{\mu_t}{Pr_t}\right)\frac{\partial T}{\partial z}\end{aligned} \tag{2.14}$$

Finally, the pressure is defined as perfect gas.

$$P = (\gamma-1)\left[E-\frac{1}{2}\rho(u^2+v^2+w^2)\right] \tag{2.15}$$

Free stream temperature(T_∞), density(ρ_∞), speed of sound(a_∞), viscosity (μ_∞) and reference length$\left(L_{ref}\right)$ are used non-dimensionalized of the equations.

2.2 Numerical Tools and Numerical Simulation Methodology

In this part flow solvers, chimera grid technique and Six-Degree of Freedom (6DOF) methodology used in this study will be covered.

2.2.1 Computational Fluid Dynamics Solver

When the governing equations for fluid motion are examined, it is obvious that these equations are highly nonlinear and for very limited problems exact solutions can be acquired [12].

In this study CFD++, a commercial Navier-Stokes solver, was used for the calculations in three dimensional, density-based and compressible flow conditions with unstructured-mesh. CFD++ is based on unified grid, unified physics and unified computing methodology in an advanced numerical discretization and solution framework [13]. The unified grid framework unifies the treatment of different cell shapes and grid topologies so that the flow solver becomes equally applicable to all cell topologies. The unified physics treatment provides the flexibility to solve many combinations of governing equation sets from incompressible flow to hypersonic flow, with additional equation sets for the modeling reactions, turbulence acoustics. The unified computing capability allows total portability between different computing platforms, including multi-CPU machines [13].

Commercial tools which are GAMBIT and TGRID are used to generate solid models and solution domains. These grid generation programs have different capabilities. According to the capabilities, GAMBIT is used for generation of the surface grids and volume grids also boundary layer grids are created with TGRID. Surface grids of the models are comprised of triangular elements. Boundary layer grids are type of wedge elements and volume grids are type of tetrahedral elements. Grid generation procedure is illustrated in Figure 2.1.

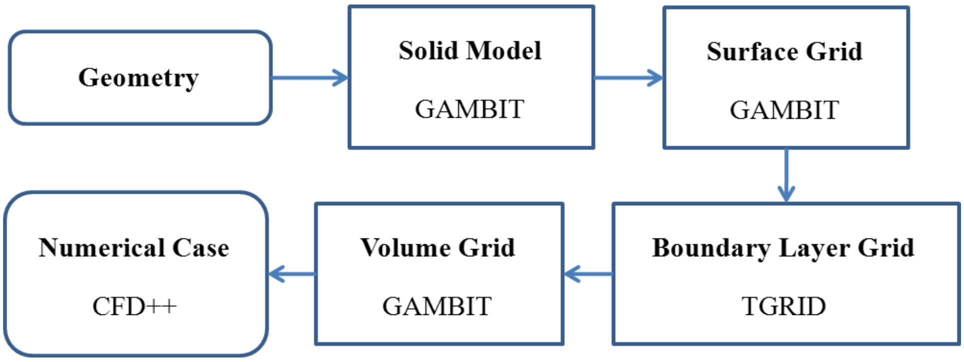

Figure 2.1 Grid Generation Procedure

2.2.2 Turbulence Modeling

Turbulence, by virtue of the range of manifested scales, remains one of the greatest challenges in computational fluid dynamics. In most flows at even modest Reynolds numbers, non-linear inertial effects in the Navier-Stokes equations tend to overwhelm the damping effects of viscosity. This causes a growth of (apparently) random disturbances, leading to a chaotic flow pattern which is usually described only in terms of its statistics, since the finest scales of motion are typically much too small to be directly resolved. The foundation for the subject of modern turbulence modeling is the contention that this fine-scale turbulence obeys certain universal rules, the effects of which can, to a large extent, be reproduced by mathematical models [13].

CFD++ provides various different options of turbulent models. In this thesis only RANS based turbulence models are considered in turbulence modeling since they are more proper for practical industrial applications.

2.2.2.1 One-equation Spalart-Allmaras Model

The Reynolds stresses are given as

$$-\overline{u_i'u_j'} = v_t S_{ij} \tag{2.18}$$

With

$$S_{ij} = \left(\frac{\partial U_i}{\partial x_j} + \frac{\partial U_j}{\partial x_i} - \frac{2}{3}\frac{\partial U_k}{\partial x_k}\delta_{ij}\right) \tag{2.19}$$

The eddy viscosity is formulated as follows:

$$\begin{gathered} v_t = \tilde{v} f_{v1} \\ f_{v1} = \frac{x^3}{x^3 + c_{v1}^3} \\ x \equiv \frac{\tilde{v}}{v} \end{gathered} \tag{2.20}$$

Transport equation for $\tilde{v}$

$$\begin{gathered} \frac{D\tilde{v}}{Dt} = c_{b1} f_{r1} (1 - f_{t2}) \tilde{S} \tilde{v} + \frac{1}{\sigma}\{\nabla.[(v + \tilde{v})\nabla\tilde{v}] + c_{b2}(\nabla\tilde{v})^2\} \\ - \left(c_{\omega 1} f_{\omega} - \frac{c_{b1}}{\kappa^2} f_{t2}\right)\left(\frac{\tilde{v}}{d}\right)^2 + f_{t1}\Delta U^2 \end{gathered} \tag{2.21}$$

Where the rotation function accounting for rotation and curvature effects is

$$f_{r1} = (1 + c_{r1})\frac{2r^*}{1 + r^*}[1 - c_{r3}\tan^{-1}(c_{r2}\tilde{r})] - c_{r1} \tag{2.22}$$

Where

$$r^{*} = \frac{\hat{S}}{\omega}$$

$$\tilde{r} = \frac{2\omega_{ik}\hat{S}_{jk}}{D^4}\left[\frac{D\hat{S}_{ij}}{Dt} + \left(\varepsilon_{imn}\hat{S}_{jn} + \varepsilon_{jmn}\hat{S}_{in}\right)\Omega_m\right]$$

$$\hat{S}_{ij} = \frac{1}{2}\left(\frac{\partial u_i}{\partial x_j} + \frac{\partial u_j}{\partial x_i}\right)$$

$$\omega_{ij} = \frac{1}{2}\left(\frac{\partial u_i}{\partial x_j} + \frac{\partial u_j}{\partial x_i}\right) + \varepsilon_{jmn}\Omega_m \qquad (2.23)$$

$$\hat{S}^2 = 2\hat{S}_{ij}\hat{S}_{ij}$$

$$\omega^2 = 2\omega_{ij}\omega_{ij}$$

$$D^2 = \frac{1}{2}\left(\hat{S}^2 + \omega^2\right)$$

It should be noted that in CFD++, the Lagrangian derivative of the strain rate tensor, $\frac{D\hat{S}_{ij}}{Dt}$, does not include the time derivatives, nevertheless changes of velocity derivatives with time will be present, albeit indirectly.

The modified strain rate is

$$\tilde{S} = S + \frac{v}{(\text{ϗ}d)^2}f_{v2}$$

$$f_{v2} = 1 - \frac{\chi}{\chi f_{v1}} \qquad (2.24)$$

The sink term involves

$$f_{\omega} = g\left(\frac{1 + c_{\omega3}^6}{g^6 + c_{\omega3}^6}\right)^{1/6} \qquad (2.25)$$

$$g = r\left[1 + c_{\omega2}\left(r^5 - 1\right)\right]$$

$$r = \frac{\tilde{v}}{\tilde{S}(\text{ϛ}d)^2}, r \leq 10$$

To allow for laminar regions, the sink term includes

$$f_{t2} = c_{t3} exp(-c_{t4}\chi^2) \tag{2.26}$$

In the above

$d = distance\ to\ nearest\ wall$
$S_{ij} = mean\ strain\ tensor$
$v = kinematic\ molecular\ viscosity$
$v_t = eddy\ viscosity$
$\omega = vorticty\ magnitude$
$\vec{\Omega} = system\ rotation\ vector$

Boundary conditions: $\tilde{v} = 0$
Model constants:
$c_{b1} = 0.1355$ $c_{b2} = 0.1355$ $\sigma = 2/3$ $\text{ϛ} = 0.41$ $c_{\omega 1} = c_{b1}/\text{ϛ}^2 + (1 + c_{b2})/\sigma$ $c_{\omega 2} = 0.3$ $c_{\omega 3} = 2$ $c_{v1} = 7.1$ $c_{t3} = 1.1$ $c_{t4} = 2$ $c_{r1} = 1.0$ $c_{r2} = 12.0$ $c_{r3} = 1.0$ $f_{t1} \equiv 0$

2.2.2.2 Two-equation Realizable k-ε Model

In CFD++'s realizable k-ε model, the Boussinesq relation is used to obtain Reynolds-stresses (algebraically) from the modeled eddy viscosity (μ_t) and the available mean-strain tensor:

$$\rho \overline{u_i u_j} = \frac{2}{3}\delta_{ij}\rho k - \mu_t S_{ij} \tag{2.27}$$

Where

$$S_{ij} = \left(\frac{\partial U_i}{\partial x_j} + \frac{\partial U_j}{\partial x_i} - \frac{2}{3}\frac{\partial U_k}{\partial x_k}\delta_{ij}\right) \tag{2.28}$$

The model consist of the following transport equations for k and ε:

$$\begin{aligned} \frac{\partial(\rho k)}{\partial t} + \frac{\partial}{\partial x_j}\left(U_j \rho k\right) &= \frac{\partial}{\partial x_j}\left[\left(\mu + \frac{\mu_t}{\sigma_k}\right)\frac{\partial k}{\partial x_j}\right] + P_k - \rho\varepsilon \\ \frac{\partial(\rho\varepsilon)}{\partial t} + \frac{\partial}{\partial x_j}\left(U_j \rho\varepsilon\right) & \\ &= \frac{\partial}{\partial x_j}\left[\left(\mu + \frac{\mu_t}{\sigma_\varepsilon}\right)\frac{\partial \varepsilon}{\partial x_j}\right] + \left(C_{\varepsilon 1} P_k - C_{\varepsilon 2}\rho\varepsilon + E\right)T_t^{-1} \end{aligned} \tag{2.29}$$

In which the rate of production of turbulence energy,

$$P_k = -\rho\overline{u_i u_j}\frac{\partial U_i}{\partial x_j} \tag{2.30}$$

Realizable estimate of the turbulence timescale,

$$\begin{gathered} T_t = \frac{k}{\varepsilon}\max\{1, \varsigma^{-1}\} \\ \varsigma = \sqrt{R_t/2} \end{gathered} \tag{2.31}$$

And the turbulence Reynolds number,

$$R_t = \frac{\rho k^2}{\mu\varepsilon} \tag{2.32}$$

The additional term, E, in the dissipation-rate equation is designed to improve the model respond to adverse pressure-gradient flows. This term has the form:

$$E = A_E \rho\sqrt{\varepsilon T_t}\Psi \max\left\{k^{\frac{1}{2}}, (\nu\varepsilon)^{\frac{1}{4}}\right\} \tag{2.33}$$

$$\Psi = \max\left\{\frac{\partial k}{\partial x_j}\frac{\partial \tau}{\partial x_j}, 0\right\}$$

$$\tau = \frac{k}{\varepsilon}$$

The model constants are given by:

$C_\mu = 0.09$, $C_{\varepsilon 1} = 1.44$, $C_{\varepsilon 2} = 1.92$, $\sigma_k = 1.0$, $\sigma_\varepsilon = 1.3$, $A_E = 0.3$

The eddy viscosity is obtained from:

$$\mu_t = \min\left\{C_\mu f_\mu \frac{\rho k^2}{\varepsilon}, \frac{2\rho k}{3S}\right\} \tag{2.34}$$

Where $S = \sqrt{S_{kl}\frac{S_{kl}}{2}}$ is the dimensional strain magnitude and f_μ is a low-Reynolds number function, designed to account for viscous and inviscid damping of turbulent fluctuations in the proximity of solid surfaces:

$$f_\mu = \frac{1 - e^{-0.01R_t}}{1 - e^{-\sqrt{R_t}}} \max\left\{1, \left(\frac{2}{R_t}\right)^{\frac{1}{2}}\right\} \tag{2.35}$$

2.2.2.3 Two-equation k-ω SST Model

The Reynolds stresses are given by

$$\rho\overline{u_i u_j} = \frac{2}{3}\delta_{ij}\rho k - \mu_t S_{ij} \tag{2.36}$$

In which

$$S_{ij} = \left(\frac{\partial U_i}{\partial x_j} + \frac{\partial U_j}{\partial x_i} - \frac{2}{3}\frac{\partial U_k}{\partial x_k}\delta_{ij}\right) \tag{2.37}$$

In the above S_{ij} is the mean strain and eddy viscosity is given as

$$\nu_t = \frac{a_1 k}{\max\{a_1\omega, SF_2\}} \tag{2.38}$$

The ingredients of this formula are as follows:

Turbulence kinetic energy transport equation

$$\frac{D(\rho k)}{Dt} = \widetilde{P_k} - \beta^* \rho k \omega + \nabla.[(\mu + \sigma_k \mu_t)\nabla k] \tag{2.39}$$

Turbulence inverse time-scale transport

$$\begin{aligned}\frac{D(\rho\omega)}{Dt} = \frac{\gamma}{\widehat{\nu_t}} P_k - \beta\rho\omega^2 + \Delta.[(\mu + \sigma_\omega \mu_t)\nabla\omega] \\ + 2(1 - F_1)\rho\sigma_{\omega^2}\frac{1}{\omega}\nabla k.\nabla\omega\end{aligned} \tag{2.40}$$

First $k - \varepsilon \rightarrow k - \omega$ blending function

$$F_1 = \tanh\left\{\left\{\min\left[\max\left(\frac{\sqrt{k}}{\beta^*\omega d}, \frac{500\nu}{d^2\omega}\right), \frac{4\rho\sigma_{\omega^2} k}{CD_{k\omega} d^2}\right]\right\}^4\right\} \tag{2.41}$$

Where

$$CD_{k\omega} = \max\left(2\rho\sigma_{\omega^2}\frac{1}{\omega}\nabla k.\nabla\omega, 10^{-10}\right) \tag{2.42}$$

Second blending function:

$$F_2 = \tanh\left\{\left[\max\left(\frac{2\sqrt{k}}{\beta^*\omega d}, \frac{500\nu}{d^2\omega}\right)\right]^2\right\} \tag{2.43}$$

Turbulence generation term

$$P_k = \left[\mu_t\left(\frac{\partial U_i}{\partial x_j} + \frac{\partial U_j}{\partial x_i} + \frac{2}{3}\frac{\partial U_k}{\partial x_k}\delta_{ij}\right) - \frac{2}{3}\delta_{ij}\rho k\right]\frac{\partial U_i}{\partial x_j} \tag{2.44}$$

Limited generation used in k equation:

$$\widetilde{P_k} = \min(P_k, 10\beta^*\rho k\omega) \tag{2.45}$$

Blending of constants:

$$\phi = \phi_1 F_1 + \phi_2(1 - F_1) \tag{2.46}$$

where ϕ stands for the various model constants.

In the above

$\sigma_{k1} = 0.85$, $\sigma_{\omega 1} = 0.5$, $\beta_1 = 0.075$,

$\gamma_1 = \beta_1/\beta^* - \sigma_{\omega 1} K^2/\sqrt{\beta^*}$,

$\sigma_{k2} = 1.0$, $\sigma_{\omega 2} K^2/\sqrt{\beta^*}$

$\beta^* = 0.09$, $K = 0.41$, $a_1 = 0.31$

Smooth wall boundary conditions with $y^+ < 3$

$$\begin{gathered} k = 0 \\ \omega = 800\frac{\nu}{(\Delta y_1)^2} \end{gathered} \tag{2.47}$$

Where $\Delta y_1$is the distance to the first centroid away from the wall. Also, d is the distance to the nearest wall; S is the invariant measure of strain rate, $\nu = \mu/\rho$

The following limited eddy viscosity is used in the ω equation:

$$\hat{\nu_t} = \max(\nu_t, 10^{-8}) \tag{2.48}$$

2.2.3 Chimera Grid Methodology

Chimera overset grid scheme is a domain decomposition approach where a full configuration is meshed using a collection of independent overset grids. This allows each component of the configuration to be gridded separately and overset into a main grid [15]. In Chimera, overset grids can move relative to each other without disturbing the grids in other zones. Since different zones are not required to align with each other, zonal grids can then be produced completely independently [16].

In this study, the Chimera methodology is used for allowing the moving body calculations. The computational domain of the body itself is constructed using patched grid. The methodology behind Chimera approach is described in the following sections.

In the following sections, process of Chimera methodology, hole-cutting process and intergrid communication are discussed.

2.2.3.1 Hole Cutting

In the Chimera grid system, intergrid communication is accomplished through data interpolation. Therefore a hole needs to be cut in each grid in the regions that overlap with solid bodies or any other non-flow regions which belong to the other grid of the overset grid system. Afterwards interpolation stencil have to be formed for cells which lie along the hole boundaries and also for other interpolation boundaries in each grid. In the present method, in order to allow flexible grid interactions, the overset grids are allowed to overlap each other in an arbitrary manner [17]. This procedure is a complex procedure and several steps are required and outlined as follows with help of an illustrative case shown in Figure 2.2.

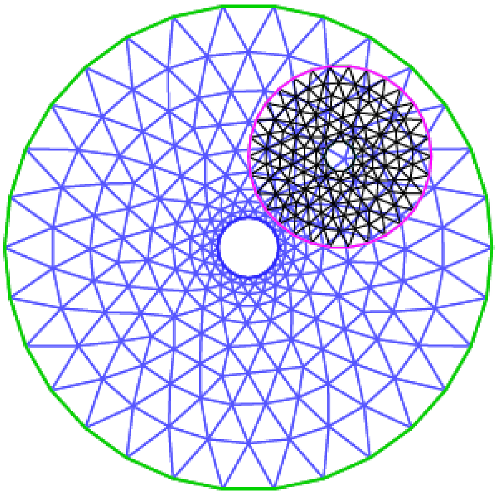

Figure 2.2 Illustration of a Chimera Grid System [18]

1. Determine the bounding boxes of all component grids and wall boundary (WB) faces;
2. If the bounding box of a component grid, let's call it A, overlaps with that of a WB face in another component grid, let's call it B, then prepare an Alternating Digital Tree (ADT) so that it will provide the coordinates of A's cells which are located on the bounding box of the overlapped WB face; as repeating this step for each face in the WB face list in grid B and identify all such cells.
3. Find out if one or more edges of the cells (identified step 2) intersect with any WB face in grid B; then decide the intersection points. The cell that contain such intersecting-edge(s) are named as cut-cells;
4. Review each edge of the cut-cells and classify the status of its two end points are either IN (if this points inside WB) or OUT (if this point is outside WB).
5. Once the status of the end points of all edges that intersect the WB faces is checked, as shown in Figure 2.3, propagate the status checking to other edges of the cut-cells and then to the adjacent cells until all the grid points that are IN are identified, as shown Figure 2.4.

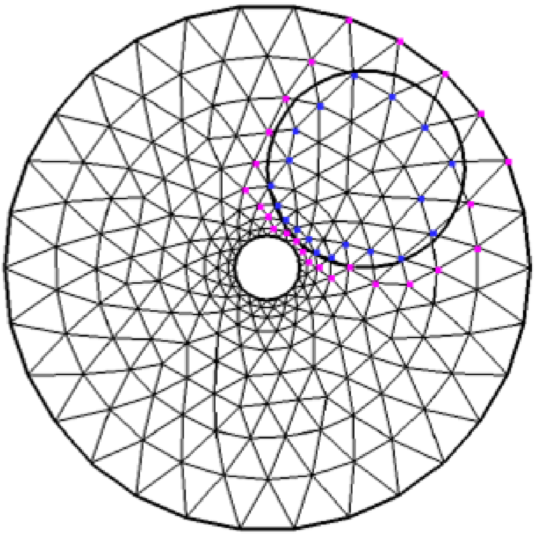

Figure 2.3 Assignment of IN/OUT Status to End Points [18]

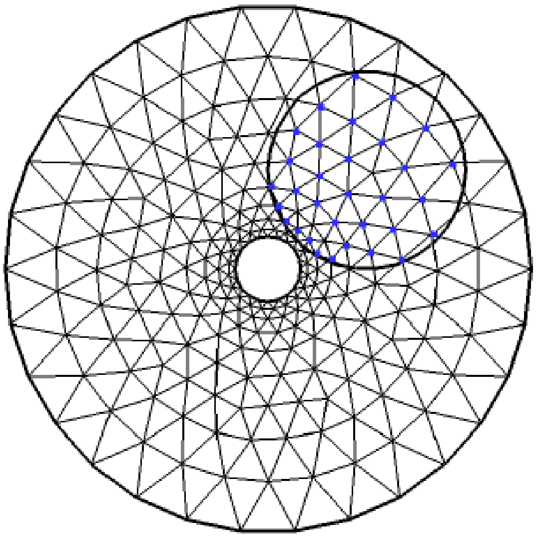

Figure 2.4 Cut-Cells of the Grid Blanketing all Grid Points [18]

6. Blank out the cells that contain IN points, as shown in Figure 2.5, therefore the hole is generated. The limiting boundary of the hole is established by the cut-cells. The cells which lie outside the WB, adjacent to the hole are identified as fringe boundary cells, as shown in Figure 2.6.

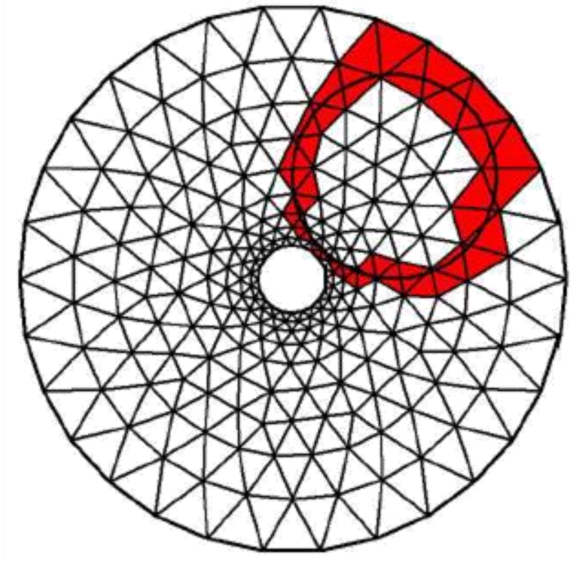

Figure 2.5 A Hole Cut in the Grid With Respect to the Given WB [18]

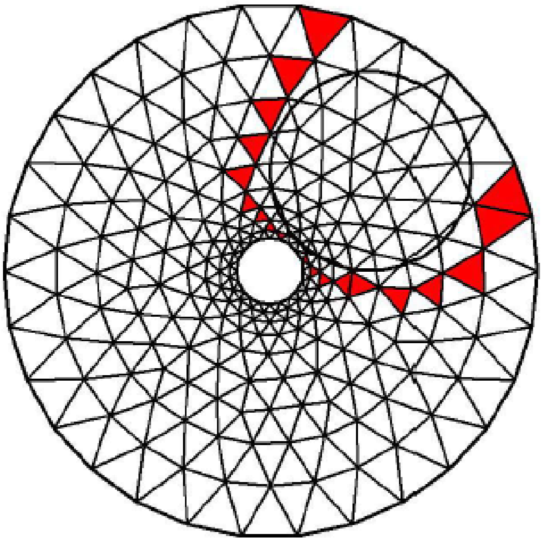

Figure 2.6 Fringe Boundary Cells Adjacent to the Cut Hole [18]

7. Repeat the steps 2-6 until all the component grids in the Chimera grid system are processed.

2.2.3.2 Intergrid Communication

In the Chimera grid method it is required to transfer information between the overlapping grids by interpolation. For each computational node that is a component grid, we need to determine if there exist some grid elements in different component grids from which the flow variables should be interpolated. In the Chimera grid system, each component grid may comprise interpolation boundary cells and/or fringe boundary cells. They represent the linkage between the component grids in the Chimera grid system. All of these are named intergrid boundary cells (IGBCs). Intergrid communication happens by interpolating data to IGBCs in each grid from the respective donors in another grid. A donor is a cell which overlaps with the interpolation boundary cells or fringe boundary cells and provides and interpolation stencil [17]. The intergrid communication is guided as follows:

1. Search all the other grids and identify the cells whose bounding boxes overlap with that of the interpolation boundary or fringe boundary.
2. Using these candidates, determine the cell that overlaps with the centroid of the interpolation boundary cell or fringe boundary cell. This cell is a donor. If more than one valid donor is found, then choose the donor with the smallest control volume.
3. Once donor cells are identified, values of the cell at the interpolation or fringe boundaries are determined from its donor cells as well as their neighboring cells by a weighted average method either inverse-distance or least-squares.

2.2.4 6DOF Methodology

One of the capabilities of CFD++ solver is moving body analysis. CFD++ is used for unsteady and time accurate problems such as shroud separation. This capability requires the rigidity of the body and the grids of the moving body. The motion of the body can be determined by a 6DOF calculation or it can be prescribed by the user.

6DOF is based on the fluid flow solution in CFD++. In order to determine forces and moments acting on the body, pressure and shear stresses are used. To calculate translational and rotational displacements of the body, forces and moments which are acting on the body are used in the general equations of motion.

The equations of motion for a rigid body with constant mass and mass moments of inertia are solved in order to obtain the linear and angular velocities and the displacements of the body in a delta time step size. These equations are given below.

$$\vec{F} = m\frac{d\vec{v}}{dt} \tag{2.49}$$

$$\vec{M} = \frac{\partial \vec{h}}{\partial t} + \vec{\omega} \times \vec{h} \tag{2.50}$$

Where m is the body mass, $\vec{v}$ is the linear velocity of the center of gravity, $\vec{h}$ is the angular momentum, $\vec{\omega}$ is angular velocity about the body's center of gravity. The force Eq. 2.49 is in the inertial frame of reference. The momentum Eq. 2.50 is in the body fixed frame of reference. The moments of inertia are completely based on the body rotating about an axis passing through its center of gravity. The main steps that include these computations are presented in Figure 2.7. This figure also summarizes the steps of the flow solver with the 6DOF calculations.

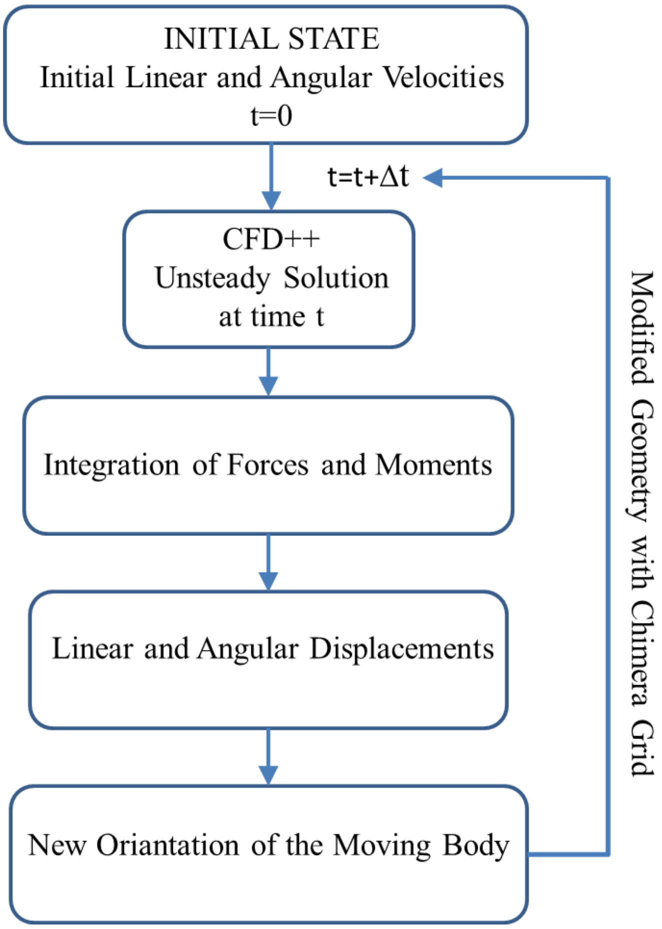

Figure 2.7 Steps of the Flow Solver with 6DOF Calculations

CHAPTER 3

VALIDATION OF TEST CASES

In this chapter, HB-1 test case is used to validate an engineering approach which is used for aerodynamic coefficient calculation [4]. Furthermore, EGLIN test case is used to validate an engineering approach which is used for the multi body CFD analysis to simulate store separation at transonic and supersonic speeds [3]. Details of these test cases are given in the following sections.

3.1 HB-1 Supersonic and Hypersonic Test Case

HB-1 Test Case model is hypersonic ballistic correlation model which is used for data evaluation and calibration in test facilities. The main target of this test case is used to examine the capabilities of CFD analysis tool by comparing results with the wind tunnel test data.

The HB-1 test case model has conical nose with cylindrical body. Basic dimensions of the configurations with respect to body diameter are presented in Figure 3.1.

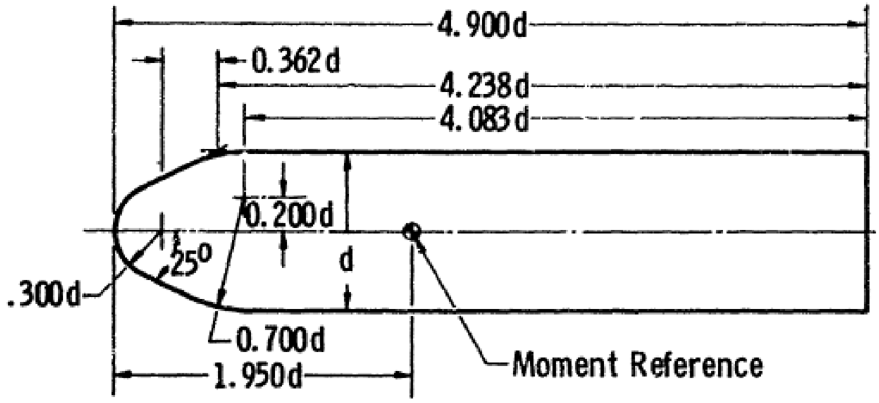

Figure 3.1 Geometry of the HB-1 Test Case

The test model was used in wind tunnel experiments which was conducted at the Arnold Engineering Development Center in Aerodynamic Wind Tunnel in 1964 [4]. The test conditions, which are used for comparisons are given in the Table 3.1.

Table 3.1 Test Conditions

Mach Number	1.5-5
Angle of Attack	$-2° < \alpha < 12°$

3.1.1 Numerical Simulation

The corresponding numerical simulation of the experiment is performed for a steady-state, compressible and turbulent flow using commercial software which is CFD++.

3.1.2 Solid Model

Solid model and computational domain are created using GAMBIT commercial software. The generated solid model and computational grid are shown in Figure 3.2.

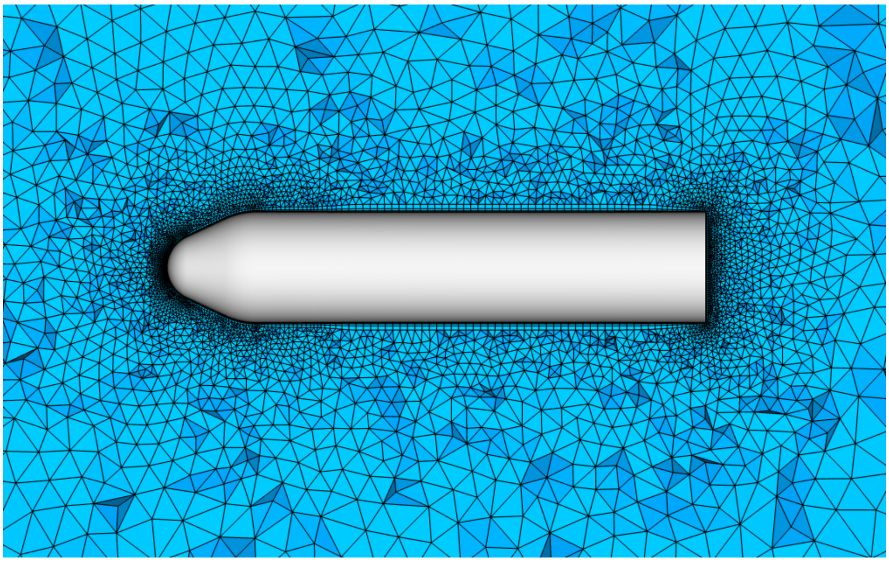

Figure 3.2 Solid Model and Computational Grid for HB-1

3.1.3 Boundary Conditions

The computational domain is large enough to minimize flow effects between model and boundaries. Outer boundaries of the computational domain are set as far-field, with sea level temperature and pressure free stream conditions are calculated with respect to Reynolds number. Table 3.2 shows Reynolds number with respect to Mach number. Solid surfaces were modeled as a no-slip, adiabatic wall boundary condition. Solution domain and defined boundary conditions are shown in the Figure 3.3.

Table 3.2 Reynolds Number With Respect to Mach Number [4]

Mach number	**Reynolds number**
1.5	990000
2	820000
3	1210000
4	600000
5	440000

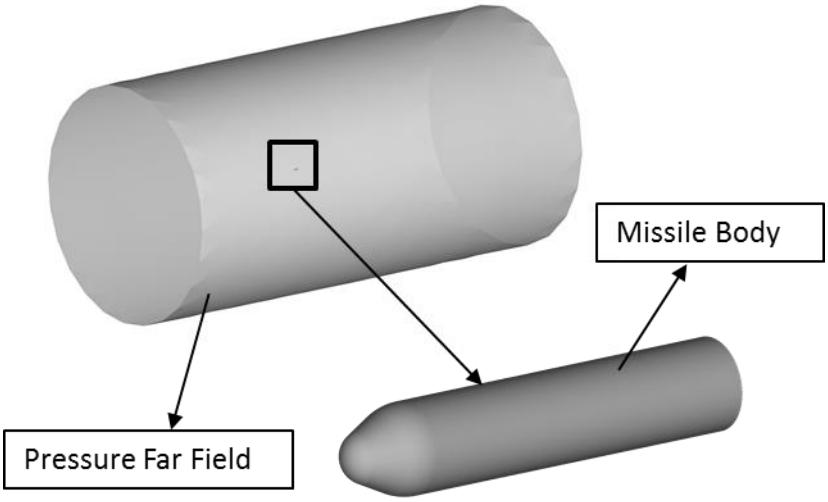

Figure 3.3 Solution Domain and Defined Boundary Condition for HB-1 Test Case

3.1.4 CFD Grid Independence Study

Grid sensitivity analyses conduct to get results independent of grid size before using the results of the numerical simulation. Three different fluid domain grids are examined to decide the minimum grid size with acceptable accuracy for this test case.

In order to capture the geometry better, unstructured grids are preferred in this study. Unstructured hybrid grids are generated by the GAMBIT. Boundary layer grid is created by TGRID. Unstructured triangular elements are used for surface grids and 30 prismatic elements are created to resolve boundary layer flow. First point of the surface is chosen to give y^+ value of about 1.0 for boundary layer grid modeling. Tetrahedral elements are used for the volume grids and the mesh growth rate is preserved below 1.15.

Three different grids are used for the grid independence study. Generated coarse, medium and fine, surface and volume grids are shown in Figure 3.4.

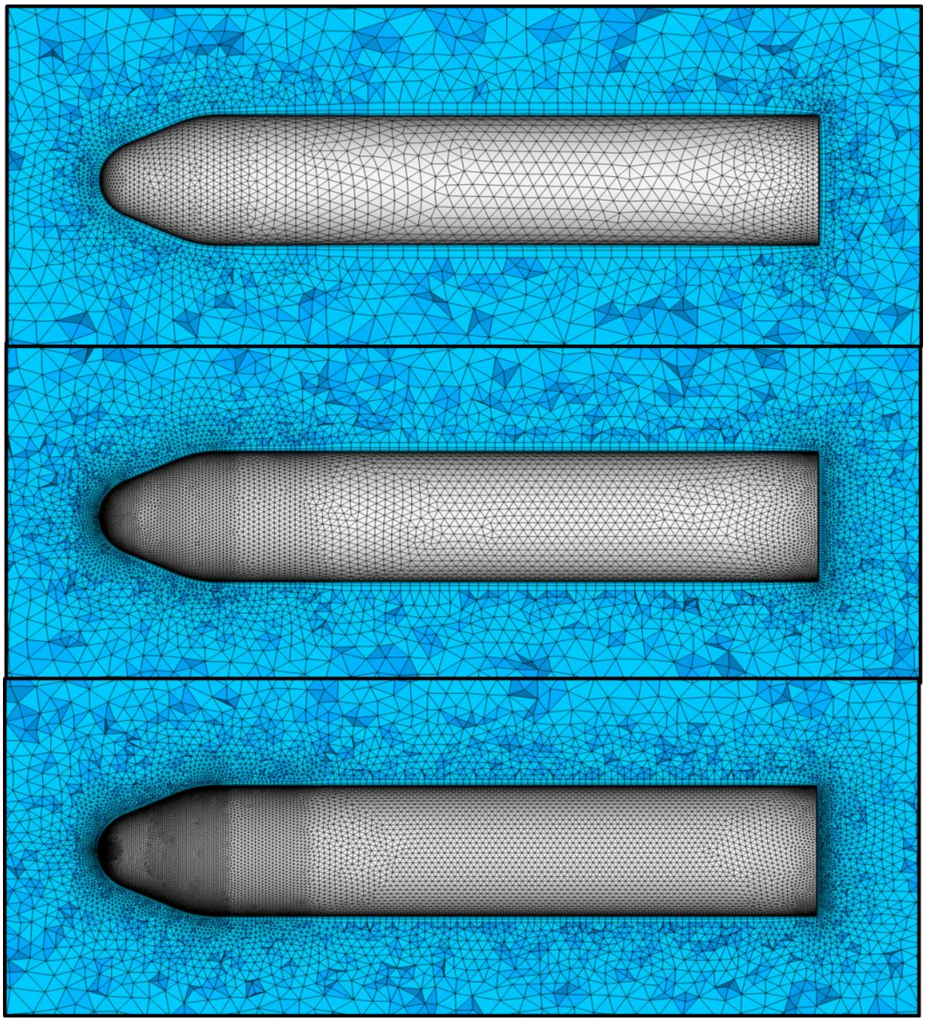

Figure 3.4 Coarse, Medium and Fine Grid

Element numbers of coarse, medium and fine grids are given in Table 3.3.

Table 3.3 Number of Elements for Different CFD Grids

Grid	Number of Elements on the Surface	Total Number of Elements
Coarse	8520	671928
Medium	25850	1496934
Fine	47692	2399480

For grid independence study, realizable k-ε turbulence model is used. Turbulence model study is carried out in the following section. CFD analyses are performed for several Mach numbers at angle of attack of 8°. CFD analysis results of grid independence study are shown in Figure 3.5, Figure 3.6 and Figure 3.7.

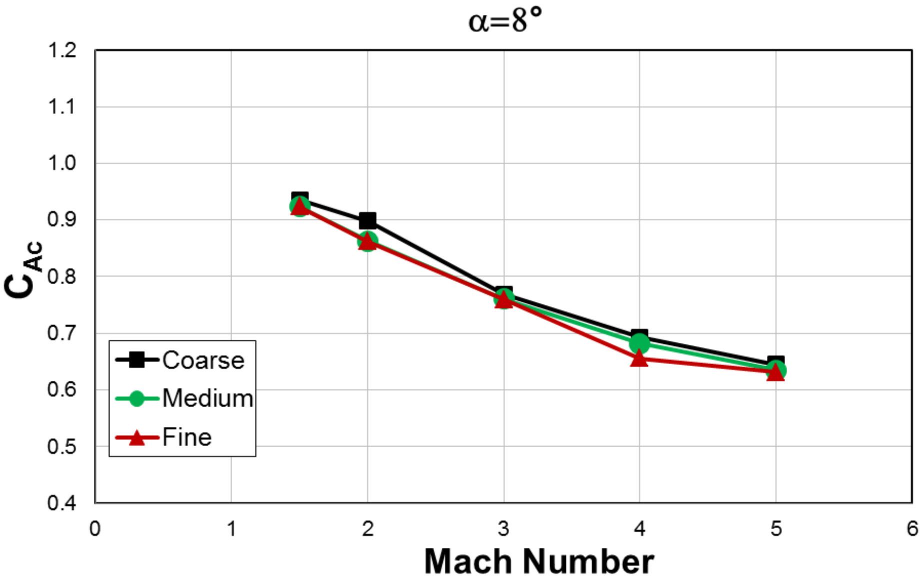

Figure 3.5 HB-1 Axial Force Coefficient with Respect to Mach for Different Grids

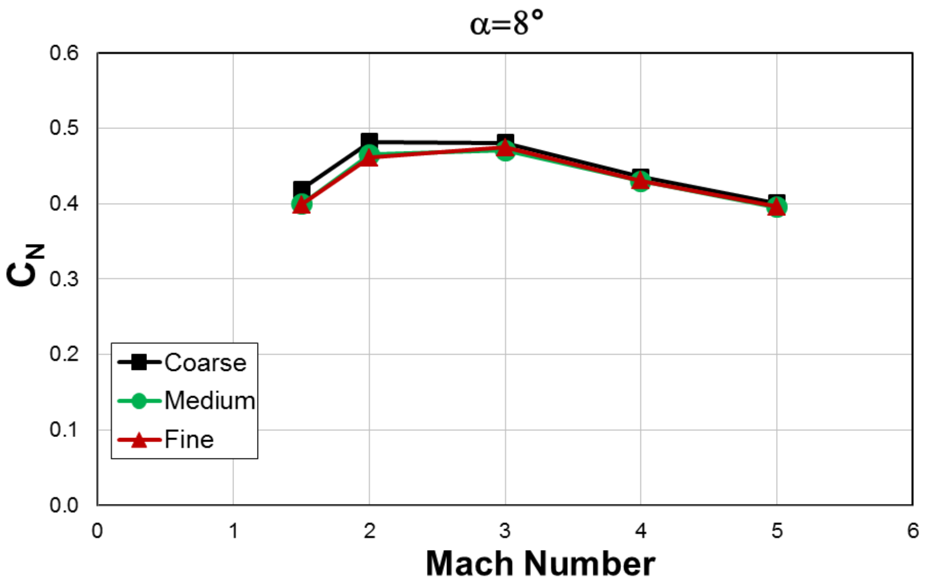

Figure 3.6 HB-1 Normal Force Coefficient with Respect to Mach for Different Grids

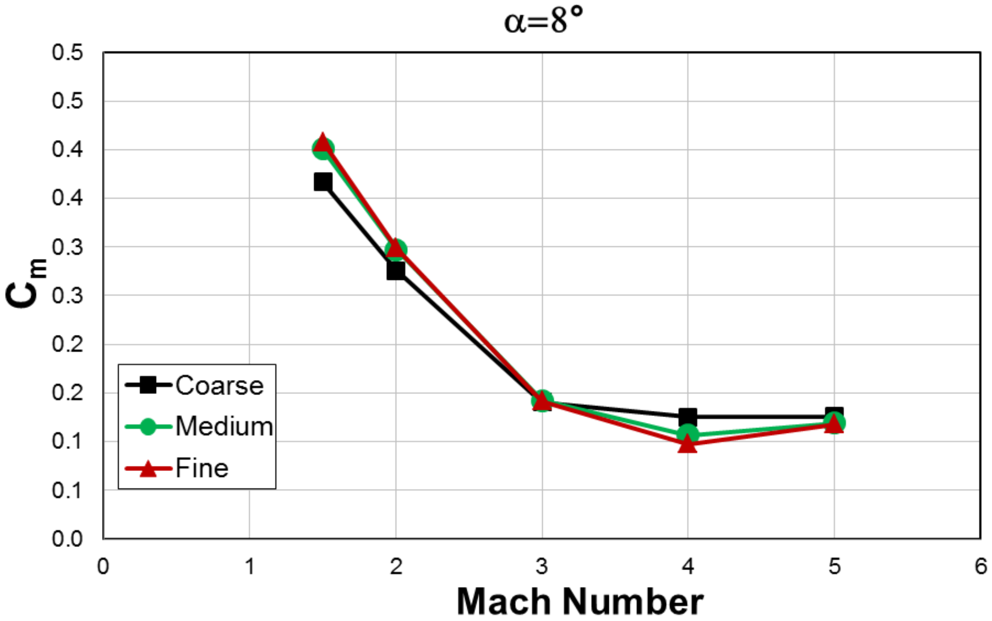

Figure 3.7 HB-1 Pitch Moment Coefficient with Respect to Mach for Different Grids

Fine and medium grids give similar results for the aerodynamic coefficient which are CA_c, CN, and Cm. However coarse gird gives different results. In order to save both time and computational power, medium gird is chosen for the rest of the thesis work.

3.1.5 Turbulence Model Selection

Results obtained using three different turbulence models; Spalart-Allmaras, Realizable k-ε and k-ω SST, are compared with experimental data in order to show the effect of turbulence model on the aerodynamic coefficients. The results for normal force and pitching moment coefficients are presented in Figure 3.8 and Figure 3.9 respectively. For body axial force coefficient, error values are calculated with respect to experiment value for each turbulence model considered in analyses and shown in Table 3.4.

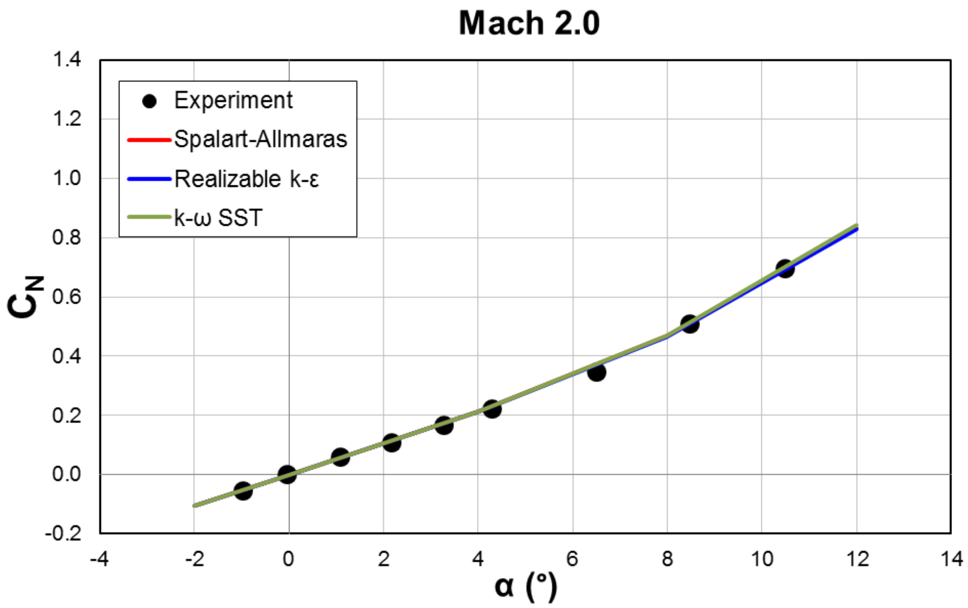

Figure 3.8 Normal Force Coefficient with Respect to Angle of Attack for Different Turbulence Models (M=2.0)

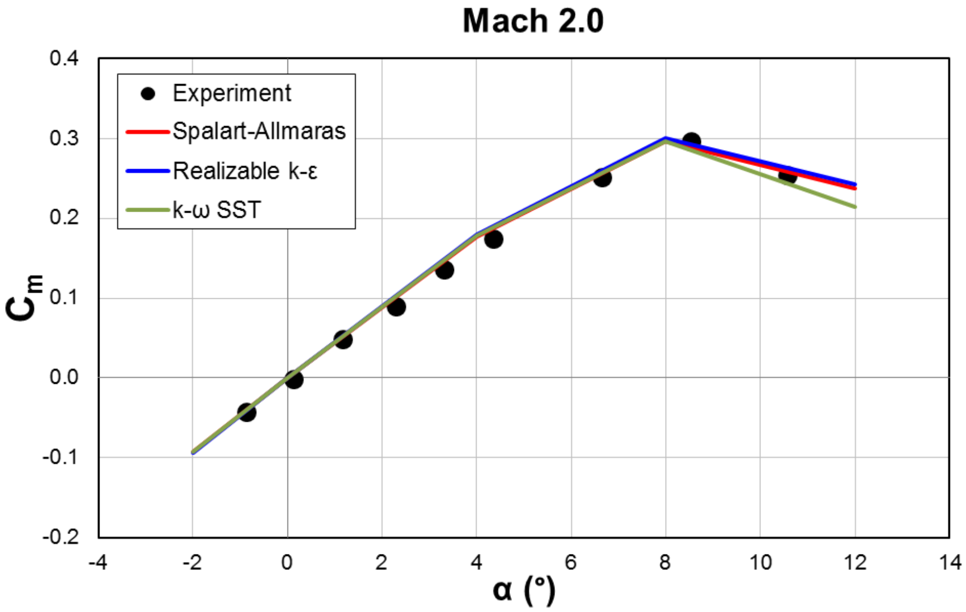

Figure 3.9 Pitch Moment Coefficient with Respect to Angle of Attack for Different Turbulence Models (M=2.0)

Table 3.4 Body Axial Force Coefficient Error for Different Turbulence Models (M=2.0, α=0°)

	Error Percentage (%)		
Coefficient	Spalart-Allmaras	Realizable k-ε	k-w SST
C_{Ac}	6.7	6.8	7.5

According to CFD results, these three turbulence models give similar results for the aerodynamic coefficients with the experimental data. However, for the CA_c coefficient k-ω SST turbulence model gives poor result when compared to other turbulence models. It can be said that Spalart-Allmaras and Realizable k-ε give satisfactory results.

3.1.6 Solution Domain Flow Visualization

Mach number and static pressure contour for HB-1 Test Case are given in Figure 3.10.

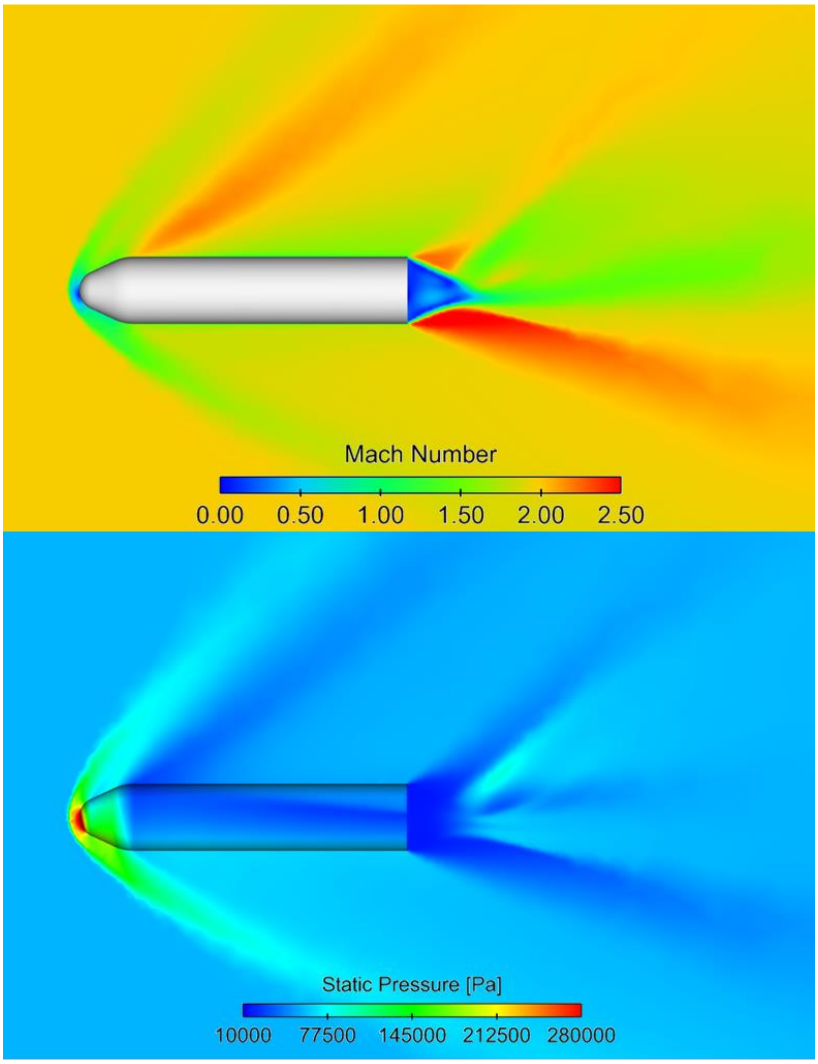

Figure 3.10 Mach number and Static Pressure Contour for HB-1 Test Case (M=2.0, α=12°)

3.2 EGLIN Store Separation Test Case

The test case model has three parts; wing, pylon and finned body. The wing consisted of a clipped delta wing with 45° sweep and a constant NACA 64a010 airfoil section. The pylon has an ogive-flat plate-ogive cross section shape. The store body was an ogive-cylinder-ogive with an aft cylindrical sting. The fins on the store consisted of a clipped delta wing with a 45° sweep and a constant NACA 0008 airfoil section. Gap between pylon and finned body is 0.07 in. The wind tunnel model was assumed to be 1:20 scale. The geometric specifications of body are presented in Figure 3.11. All dimensions are given in inches [19].

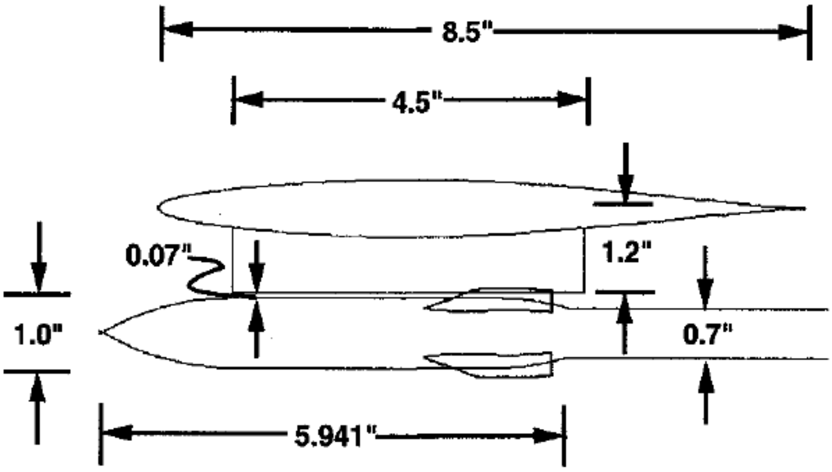

Figure 3.11 Geometry of the EGLIN Test Case

This test model is used in wind tunnel experiments conducted at the Arnold Engineering Development Center in Aerodynamic Wind Tunnel in 1990. Sketch of the EGLIN test case model and sting used in the wind tunnel test are represented in Figure 3.12 [19].

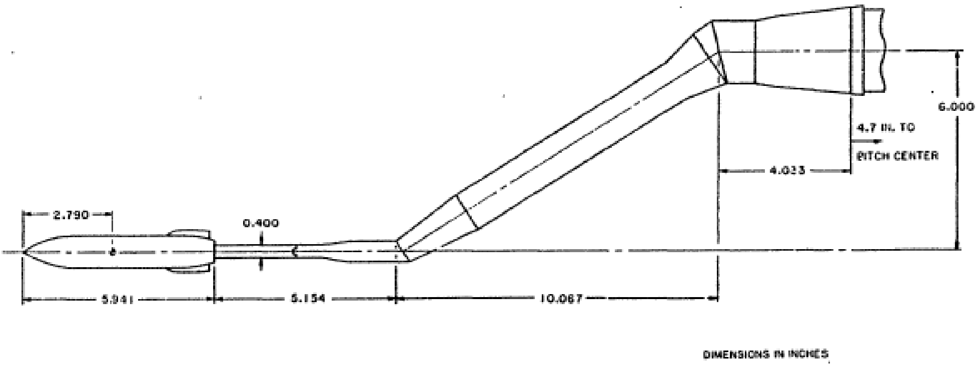

Figure 3.12 Sketch of the EGLIN Test Case Wind Tunnel Test

Experiment conducted in transonic regime (M=0.95) and supersonic regime (M=1.2). During experiments position and angle change of store is obtained for both flow regimes.

In the test, aft and forward ejector forces are applied to store to provide safe separation. The ejector characteristics and other full-scale store parameters are presented in Table 3.5 [3].

Table 3.5 Store and Ejector Information

Weight	907 kg
Center of Gravity	1417mm (aft of store nose)
Roll moment of inertia	27 kg.m^2
Pitch moment of inertia	488 kg.m^2
Yaw moment of inertia	488 kg.m^2
Forward ejector location	1237.5mm (aft of store nose)
Aft ejector location	1746.5mm (aft of store nose)
Forward ejector force	10.7kN
Aft ejector force	42.7kN

3.2.1 Numerical Simulation

The related numerical simulation of the experiment is performed for a transient, compressible and turbulent flow using CFD++ with chimera grid methodology.

3.2.2 Solid Model

Solid model and computational domain are created using GAMBIT commercial software. The generated solid models are shown in Figure 3.13. Sting geometry was not used in CFD modeling because the effect of sting was corrected for wind tunnel measurement.

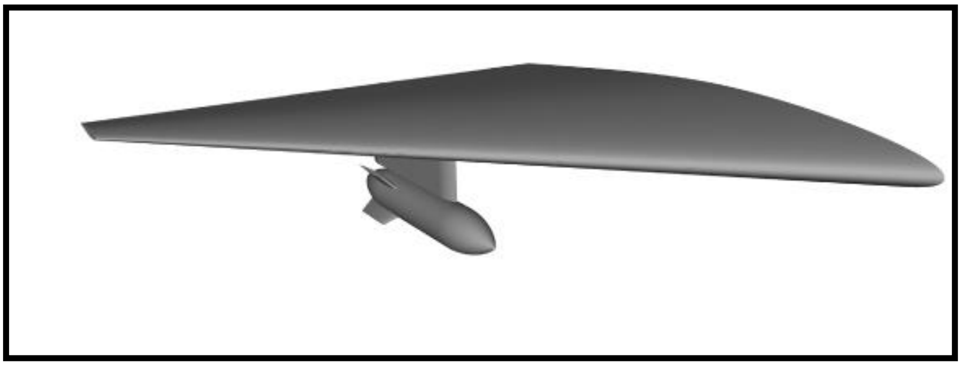

Figure 3.13 Solid Model of EGLIN Test Case

3.2.3 Boundary Conditions

The computational domain is large enough to minimize flow effects between model and boundaries. The computational domain inlet was located 17 model wing length upstream from center of body, outlet was located 25 wing length downstream from the center of body, above boundary was located 17 model length from the center of the body, below boundary was located 25 model length from the center of the body and side boundary was located 17 model length from the center of the body. Downstream, upstream, and all side boundaries except right side were set as pressure far-field, using standard atmosphere model at 26000 ft altitude for temperature and pressure free stream conditions. Right side boundary was defined as symmetric. Solid surfaces were modeled as a no-slip, adiabatic wall boundary condition. Solution domain and defined boundary conditions are shown in the Figure 3.14. Numerical simulation of the experiment model is conducted at Mach number of 1.2.

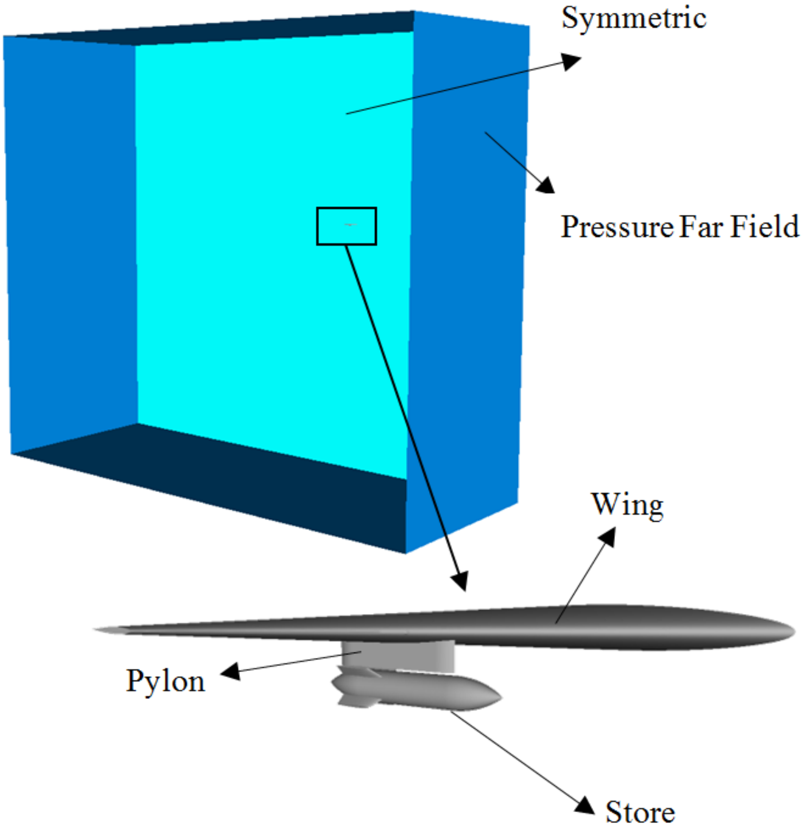

Figure 3.14 Solution Domain and Boundary Conditions for EGLIN Test Model

3.2.4 Turbulence Model Selection

CFD analyses are performed for three different turbulence models to investigate effect of turbulence model for store separation on EGLIN Test Model. CFD results (distance and angle) are compared with experimental data and given in Figure 3.15 and Figure 3.16.

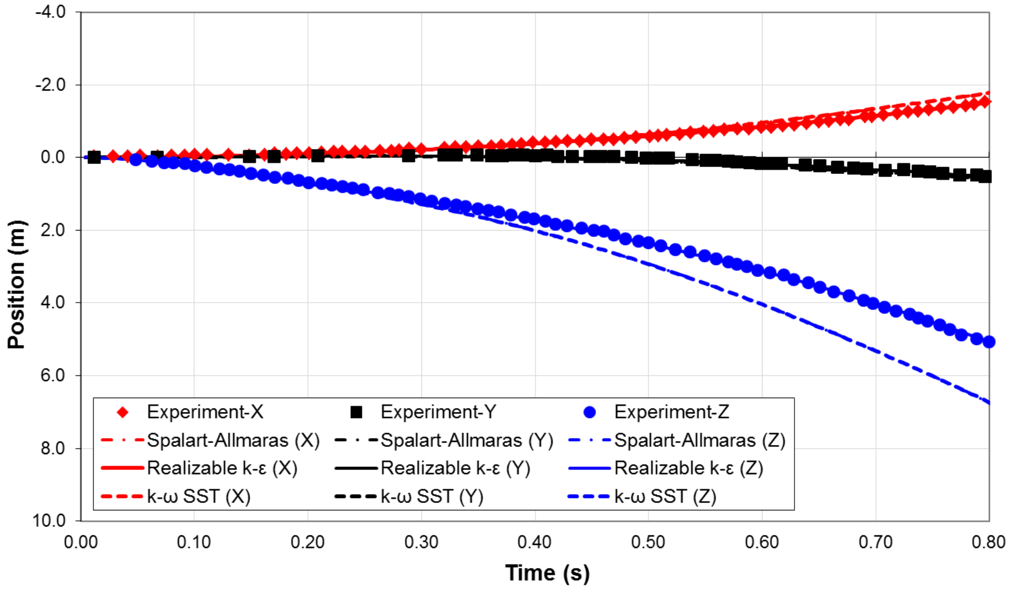

Figure 3.15 Store Position Change Results and Experimental Data with respect to Time for Different Turbulence Models [3]

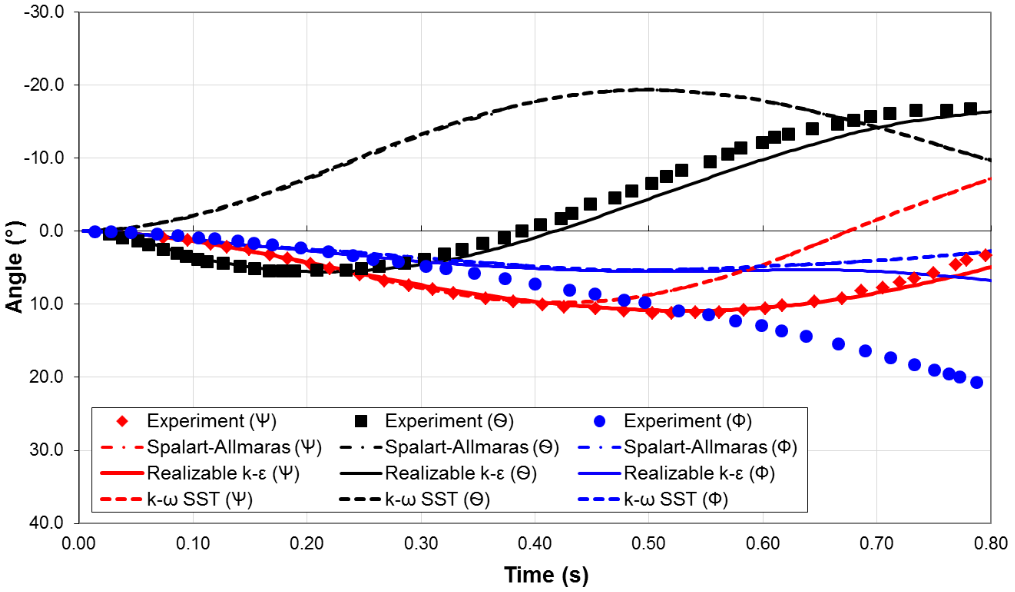

Figure 3.16 Store Angle Change Results and Experimental Data with respect to Time for Different Turbulence Models [3]

As presented in figures, solutions obtained by k-ε turbulence model are more accurate than solutions of the other two models compared to the experimental data.

3.2.5 CFD Simulation Results

Store separation is simulated for EGLIN test case. Transient CFD analysis is performed for given flight condition in Table 3.6.

Table 3.6 Flight Condition for Store Separation

Static Pressure [Pa]	20646
Temperature [K]	217
Mach Number	1.2

Time dependent position and angle changes are obtained from CFD simulation and results are compared with experimental data [3]. Results are given in Figure 3.17 and Figure 3.18.

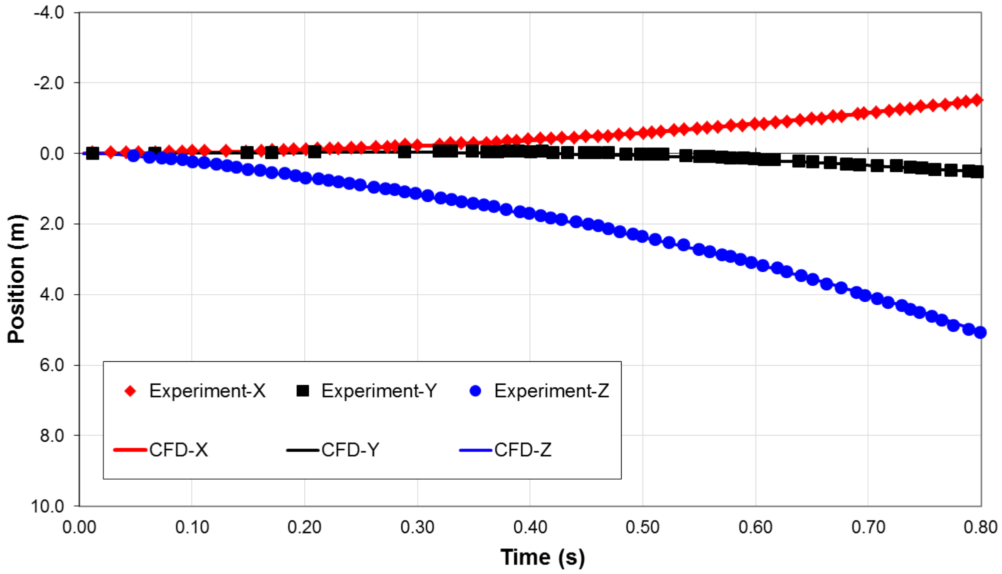

Figure 3.17 Store Position Change and Experimental Data With Respect to Time

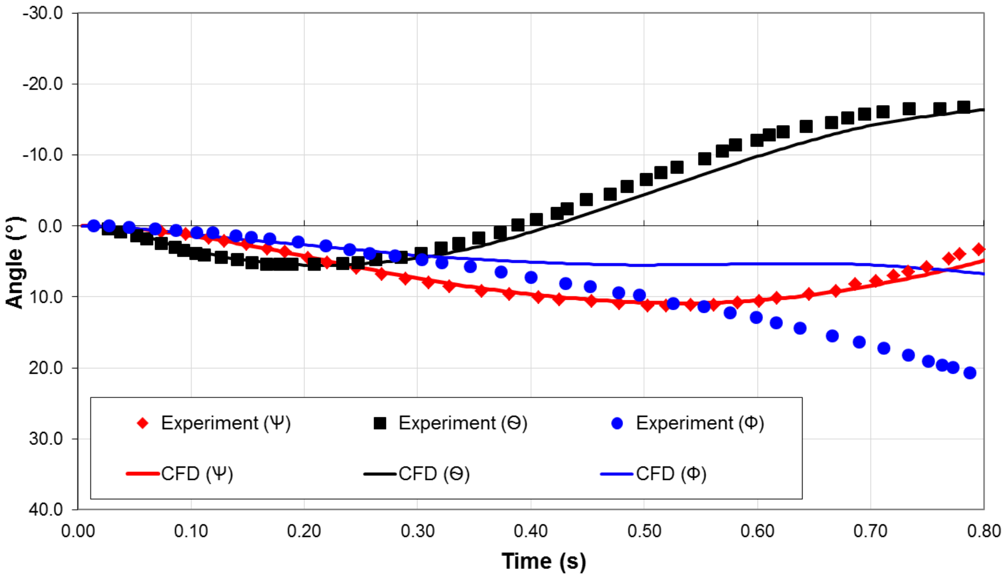

Figure 3.18 Store Angle Change and Experimental Data With Respect to Time

As shown in the Figure 3.17 the store position changes are very similar with the experimental data. Also in the Figure 3.18 store pitch and yaw angle changes are in good agreement with experimental data. On the other hand the store rolls continuously outboard throughout the first 0.8 seconds of the separation. This trend is under-predicted by the CFD, and the curve tends to diverge from the experiments after approximately 0.3 seconds. The roll angle is especially difficult to model because the moment of inertia about the roll axis is much smaller than that of the pitch and yaw axes. Consequently, roll is very sensitive to errors in the aerodynamic force prediction.

In addition CFD analysis is initialized as steady analysis. After convergence of steady run, transient CFD analysis is continued on steady CFD analysis data file to achieve easier convergence. Time step is selected as 0.0001 s and 25 sub-iterations are made for transient CFD analysis.

Also, visual presentation of CFD and experimental results is given in Figure 3.19, and pressure distribution on store and wing with respect to time is given in Figure 3.20.

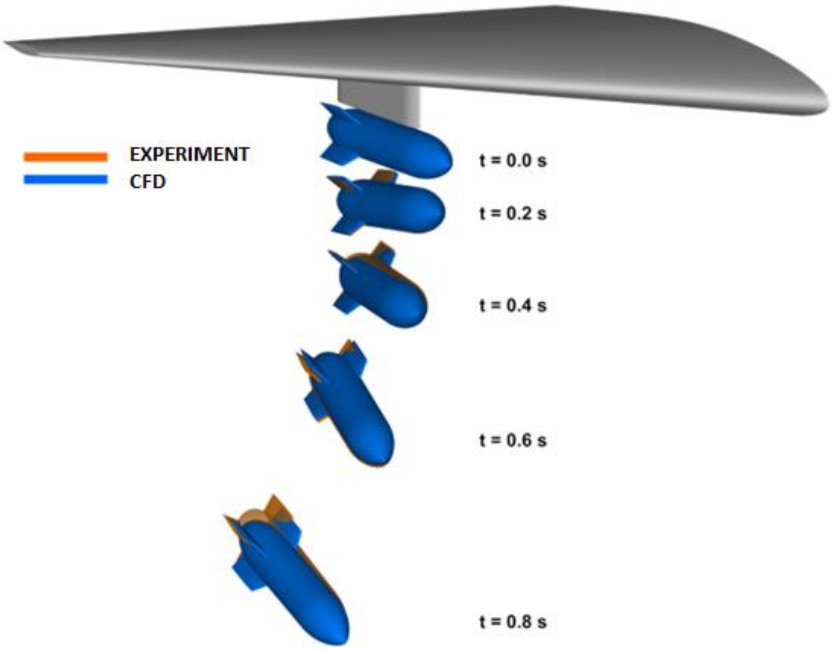

Figure 3.19 Visual Presentation of CFD and Experimental Results

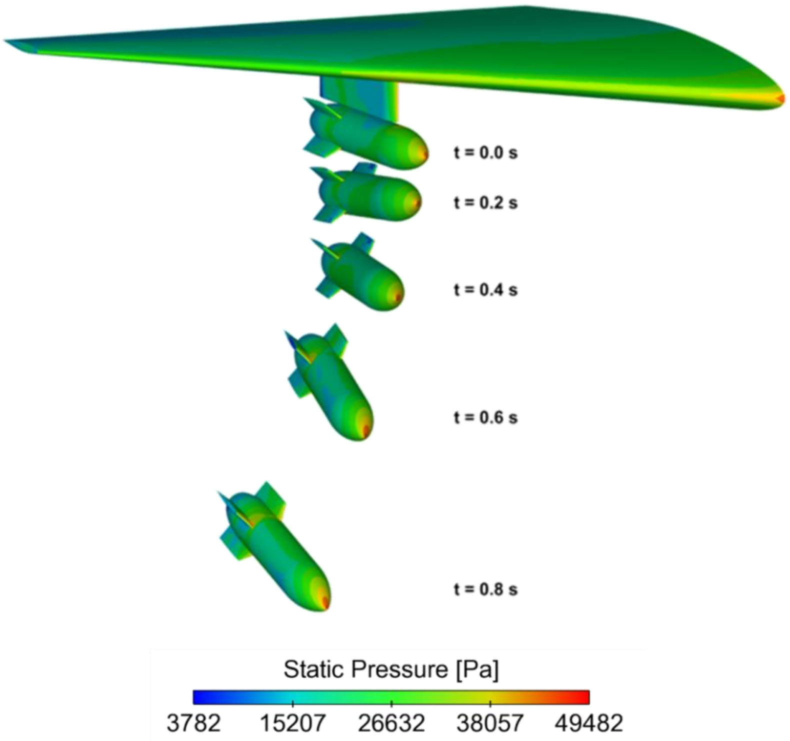

Figure 3.20 Pressure Distribution with Respect to Time for Store Separation

CHAPTER 4

CFD ANALYSIS OF MISSILE SHROUD SEPARATION

In this part of the thesis, CFD analysis of shroud separation on generic missile is performed to investigate safe separation of the shroud covers from missile for different parameters which are altitude, Mach number, angle of attack, side-slip angle and ejection moment. Selected generic missile geometry has conical nose with cylindrical body. Basic dimensions of the generic missile with respect to body diameter are presented in Figure 4.1. Selected shroud geometry has tangent-ogive nose appropriate for conical generic missile nose. Basic dimensions of the shroud geometry with respect to body diameter are given in Figure 4.2.

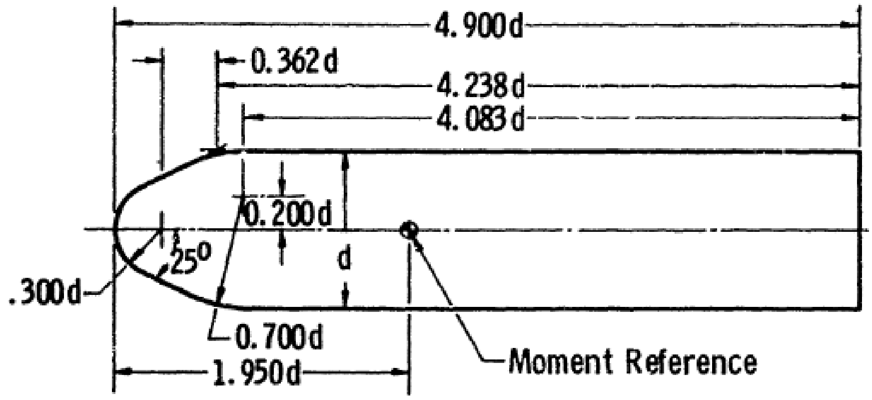

Figure 4.1 Geometry Specification of Generic Missile

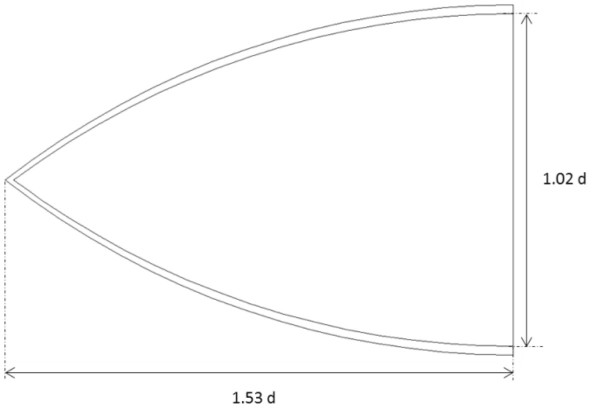

Figure 4.2 Geometry Specification of Shroud Model

4.1 Numerical Simulation

The corresponding numerical simulation of the shroud separation is performed for a transient, compressible and turbulent flow using CFD++ with chimera grid methodology.

4.2 Solid Model and Grid Generation

Solid model of the generic missile geometry with shroud is created by using GAMBIT commercial software. The generated solid model is shown in Figure 4.3.

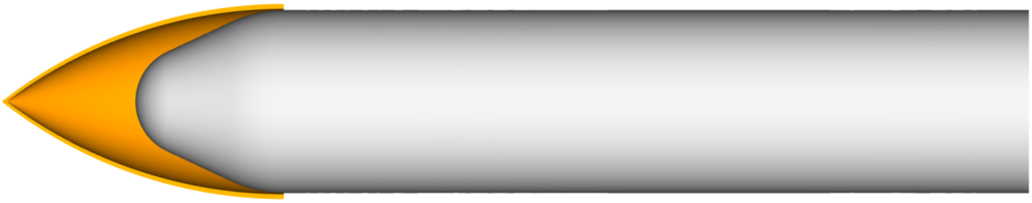

Figure 4.3 Solid Model of the Generic Missile with Shroud (Side View)

The surface, boundary layer and domain grid generation of missile with shroud is similar with HB-1 test case. Surface, domain grid and Chimera grid system are given in Figure 4.4, Figure 4.5 and Figure 4.6.

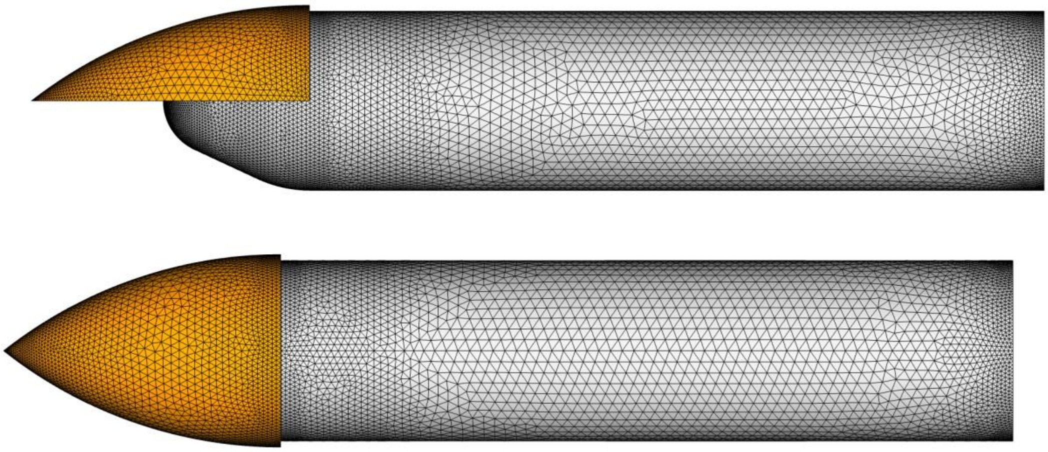

Figure 4.4 Surface Grid for Generic Missile with Shroud (Top View and Side View)

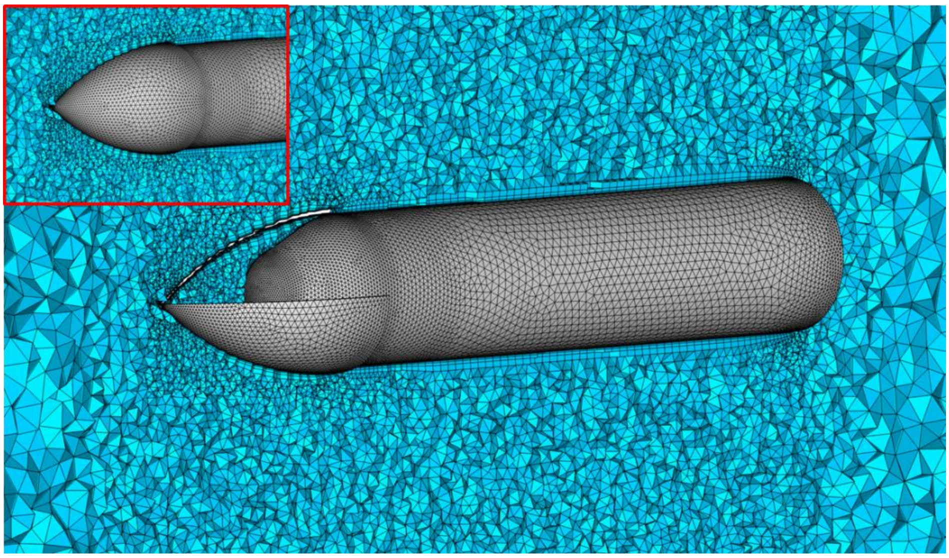

Figure 4.5 Surface and Volume Grids for Generic Missile with Shroud

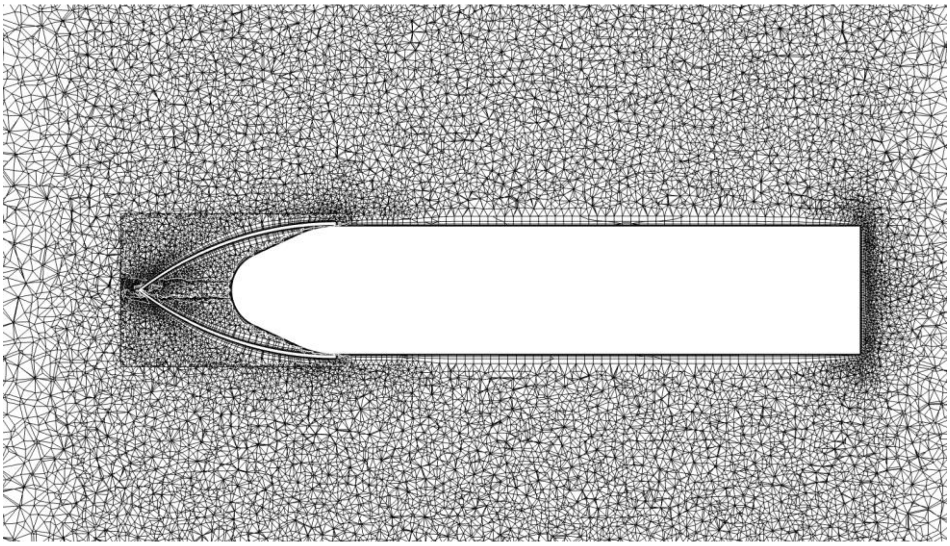

Figure 4.6 System of Chimera Grid

4.3 Boundary Conditions and Material Properties

The solid surfaces were defined as no-slip wall boundary condition. The outer surfaces of fixed fluid domain were defined as pressure far field boundary condition with constant freestream static pressure, static temperature and velocity. Solution domain and defined boundary conditions are shown in the Figure 4.7.

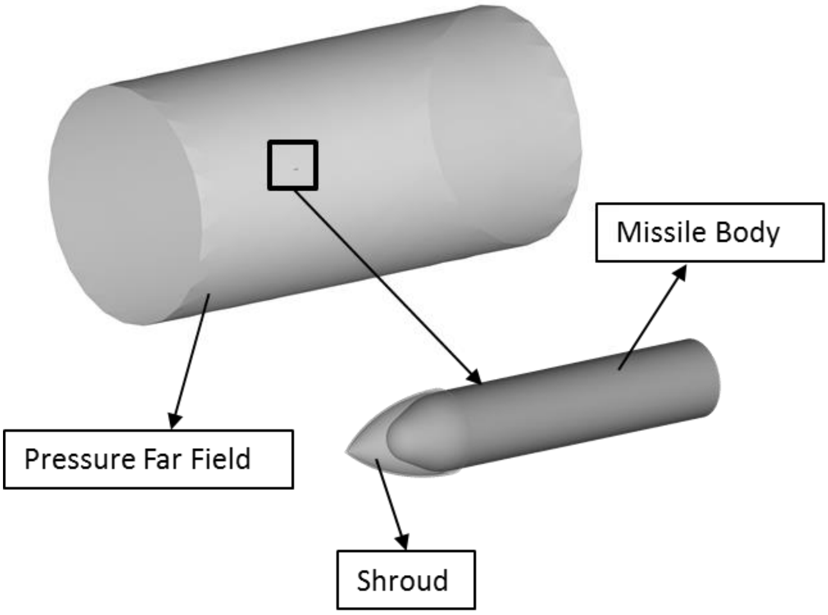

Figure 4.7 Solution Domain Boundary Condition

The material of shroud model was chosen as steel. Therefore, material properties and moment of inertia of shroud models can be found in Table 4.1. The value of moment of inertia for shroud models were given with respect to both center of gravity (CG) and hinge point (HP).

Table 4.1 Material Properties For Shroud Model

Shroud Model (Half)			
Mass	3.917913 [kg]		
Moment Of Inertia (CG)	Ix [kg.m^2]	Iy [kg.m^2]	Iz [kg.m^2]
	0.023513	0.031706	0.046233
Moment Of Inertia (HP)	0.037201	0.109247	0.110086

4.4 Shroud Release Procedure

The shroud release procedure consists of two stages. At the first stage, the shroud is hinged to the main body and can rotate only about the hinge axis up to 30°. At the second stage, the shroud is released from the hinge and can move in space 6DOF. Schematic drawing of the shroud release procedure is presented in Figure 4.8.

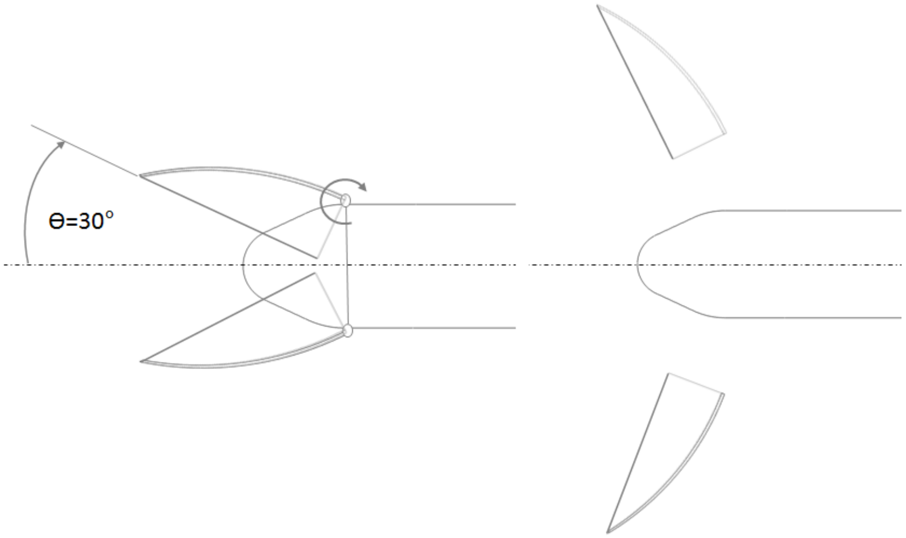

Figure 4.8 Schematic drawing of the Shroud Release Procedure

In addition, the flow chart of shroud release procedure can be seen in Figure 4.9.

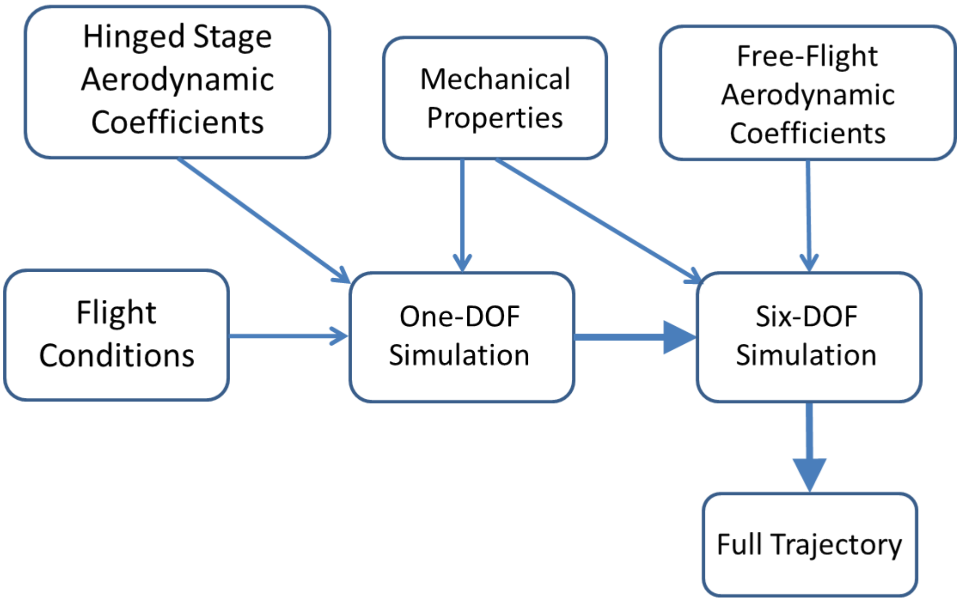

Figure 4.9 The Flow Chart of Shroud Release Procedure

Also, steady CFD analysis was performed for missile with shroud to determine aerodynamic forces acting on the shroud at flight condition of 5000 m altitude, 2.0 Mach number and 0° angle of attack. Therefore, an ejection moment was assumed to overcome aerodynamic forces acting on shroud and to initialize the separation.

In addition all ejection moment values applied on shroud covers along 10 milliseconds to initialize the shroud separation.

4.5 Turbulence Model Selection

CFD analyses are performed for three different turbulence models which are Spalart-Allmaras, Realizable k-ε and k-ω SST to investigate effect of turbulence model for missile shroud separation. Flight condition and applied ejection moment is given in Table 4.2 for this study.

Table 4.2 Flight conditions and Ejection Moment for Turbulence Model Selection

Altitude [m]	5000
Mach Number	2
Angle of Attack [°]	0
Ejection Moment [Nm]	1000

CFD results (shroud trajectories) are compared with each other and given in Figure 4.10.

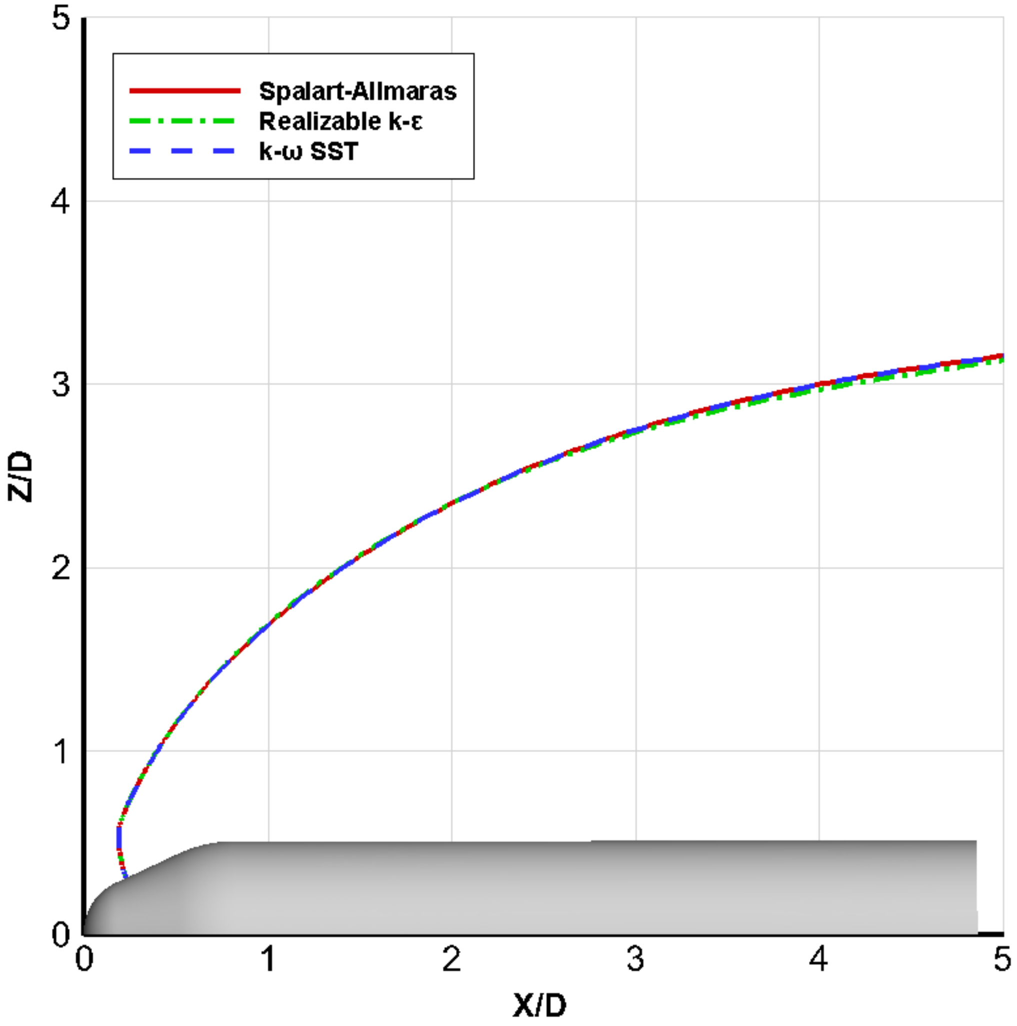

Figure 4.10 Shroud Trajectories for Different Turbulence Models

As presented in figure, all turbulence models give similar results for the missile shroud separation. This study was performed in supersonic velocity so turbulence model did not affect shroud trajectories dramatically. On the other hand, selection of turbulence model is important in transient region and this effect was shown in previous study which is store separation. Therefore for the rest of the analyses k-ε turbulence model is used.

4.6 CFD Analysis Results

CFD analysis is performed in order to investigate safe separation of the shroud covers from missile for different parameters which are altitude, Mach number, angle of attack, side-slip angle, ejection moment and analysis results presented in this part. In addition CFD analysis is initialized as a steady analysis and after convergence of steady run transient CFD analysis is continued on steady CFD analysis data file to make convergence easy. Time step is selected as 0.0001 and 25 sub-iterations are made for transient CFD analysis. Approximately overall clock time of only one analysis is about 6 days for 40 CPU.

4.6.1 Effects of Altitude

In this part, effects of altitude are investigated. Shroud separation analyses are performed at five different altitudes by keeping the Mach number, angle of attack and ejection moment constant. Flight conditions and applied ejection moment are given in Table 4.3 for this part.

Table 4.3 Flight conditions and Ejection Moment for Effects of Altitude

Altitude [m]	0	3500	5000	7500	10000
Mach Number	2				
Angle of Attack [°]	0				
Ejection Moment [Nm]	1000				

Shroud trajectories belonging to four different altitudes are given in Figure 4.11. These trajectories reflect position change of center of gravity of shroud.

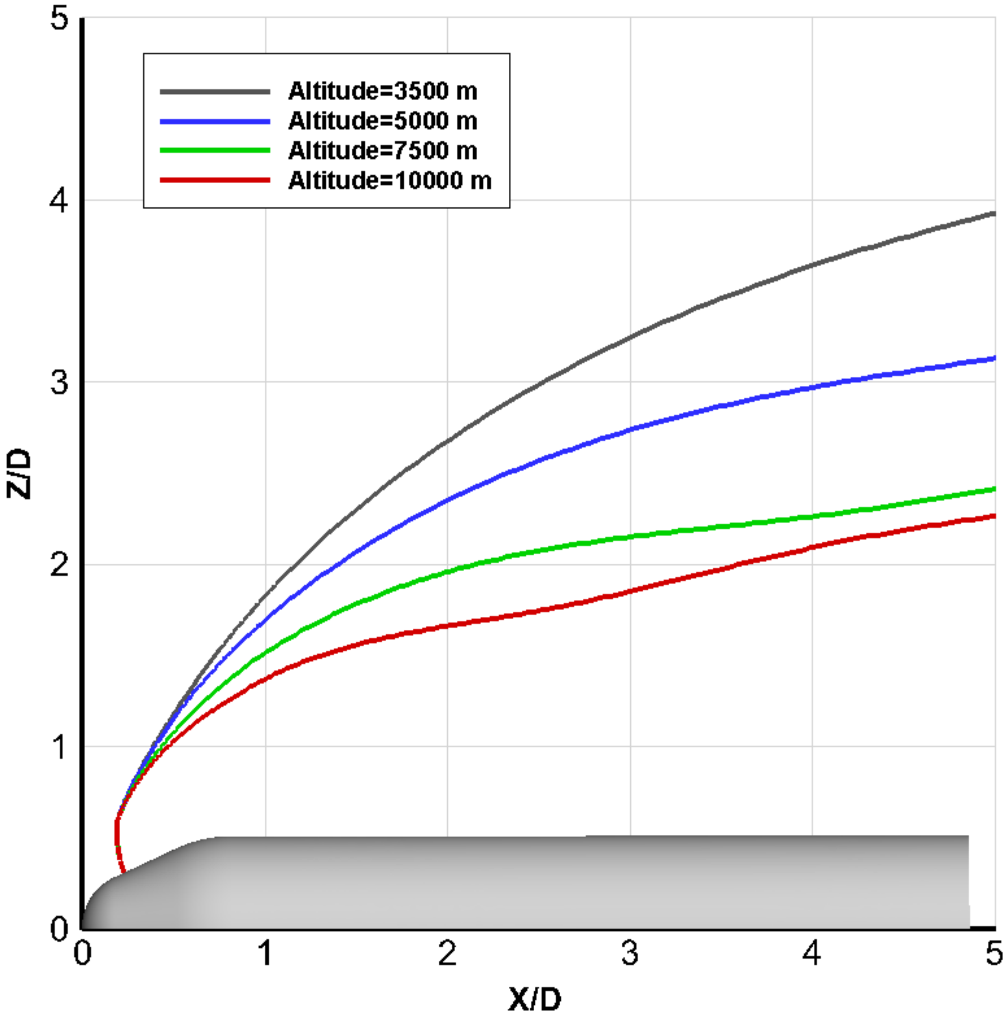

Figure 4.11 Shroud Trajectories for Different Altitudes

As it is shown in above figure, shroud separation is performed safely for the specified flight conditions and ejection moment at four different altitudes which are 3.5 km, 5 km, 7.5 km and 10 km. Also, 3500 m altitude is the minimum altitude, for which shroud separation can be initialized with 1000 Nm ejection moment. The shroud does not separate at sea level because the ejection moment is not enough for the initialization of the separation at this flight condition. Besides, the closest shroud trajectory is followed at maximum altitude level and the furthest shroud trajectory is followed at minimum altitude level where shroud can be separated. As the reason for this, it can be shown that Z-force with respect to time for different altitudes in Figure 4.12.

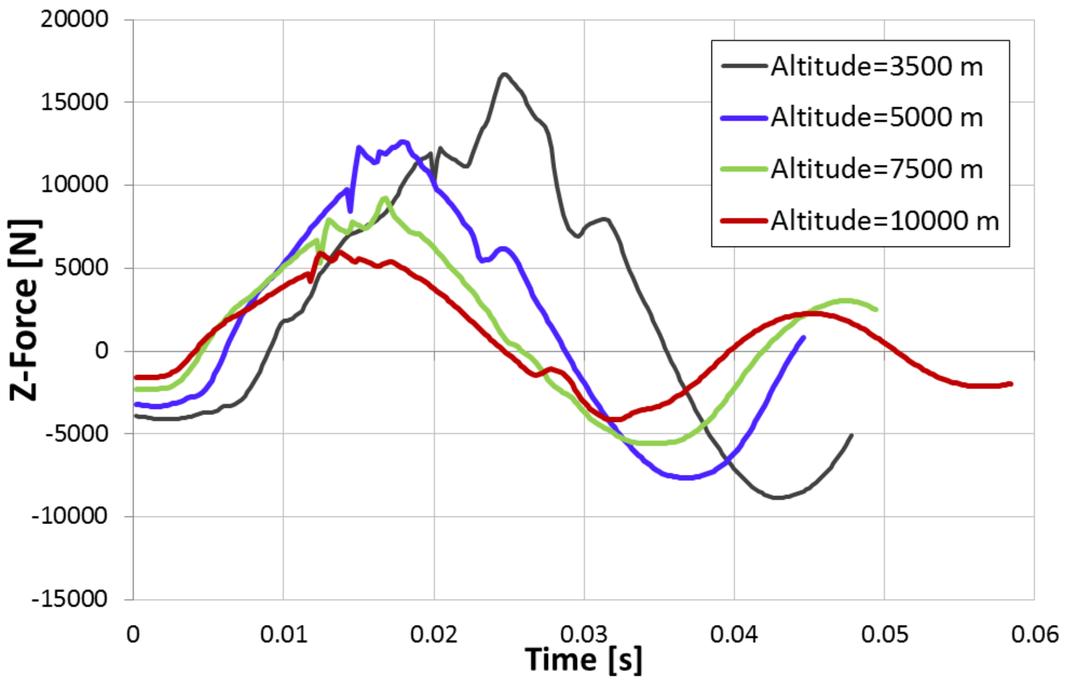

Figure 4.12 Z-Force Acting on the Shroud with Respect to Time for Different Altitudes

As the altitude increases, density of the air decreases leading to lower aerodynamic forces acting on the shroud. In the same manner, it can be seen from Figure 4.12 that an increased Z-Force which is acting on the Z direction of the shroud covers determines with decreasing altitude. This phenomenon affects the trajectory of the shroud covers during separation. When the Z-Force change of the shroud is higher, force acting on the Z direction that separates the shroud from the missile becomes larger. Therefore, maximum separation distance for the shroud is obtained when Z-force change of the shroud is the highest. Besides, decreasing of the altitude leads to increasing of the X-Force which is acting on the X direction in Figure 4.13. Therefore, shroud covers reach the same position along the X direction in the shorter time.

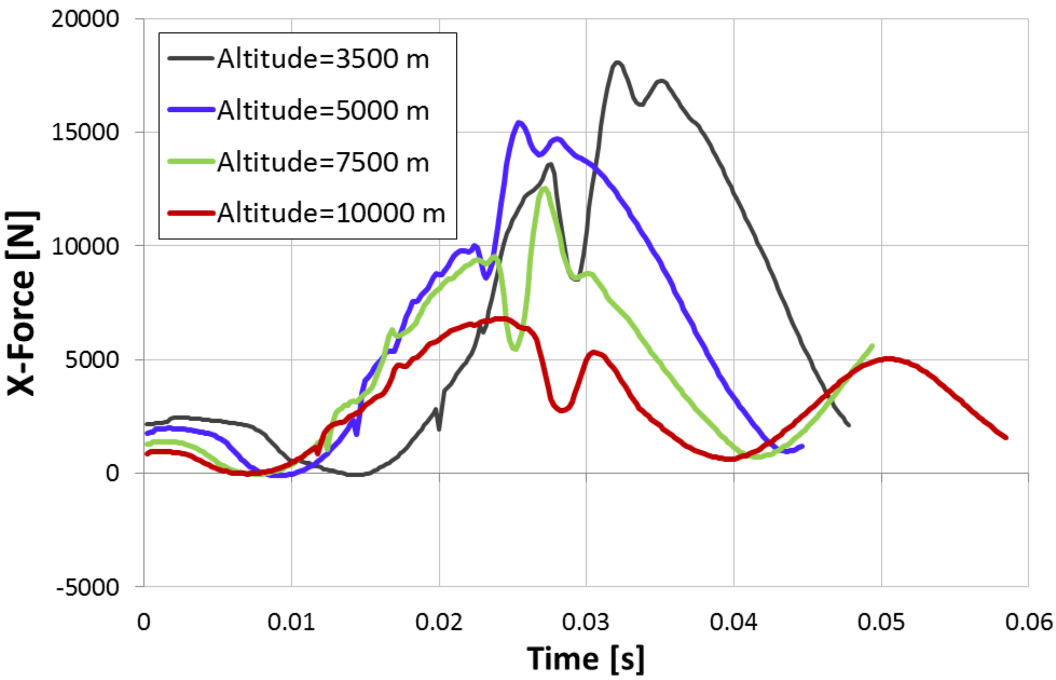

Figure 4.13 X-Force Acting on the Shroud with Respect to Time for Different Altitudes

These analyses show that under these conditions minimum altitude for the safe separation of shroud is determined. In addition to that the analysis shows that larger ejection moment are desired for safe separation of shroud as seen with decreasing altitude. Also, summary of the shroud separation for effect of altitude can be seen in Table 4.4.

Table 4.4 Summary of the Shroud Separation for Effect of Altitude

Altitude=0 m	Shroud Separation Failed
Altitude=3500 m	Safe Separation
Altitude=5000 m	Safe Separation
Altitude=7500 m	Safe Separation
Altitude=10000 m	Safe Separation

4.6.1.1 Solution Domain Flow Visualization

Mach number and static pressure contours for shroud separation are given in below figures.

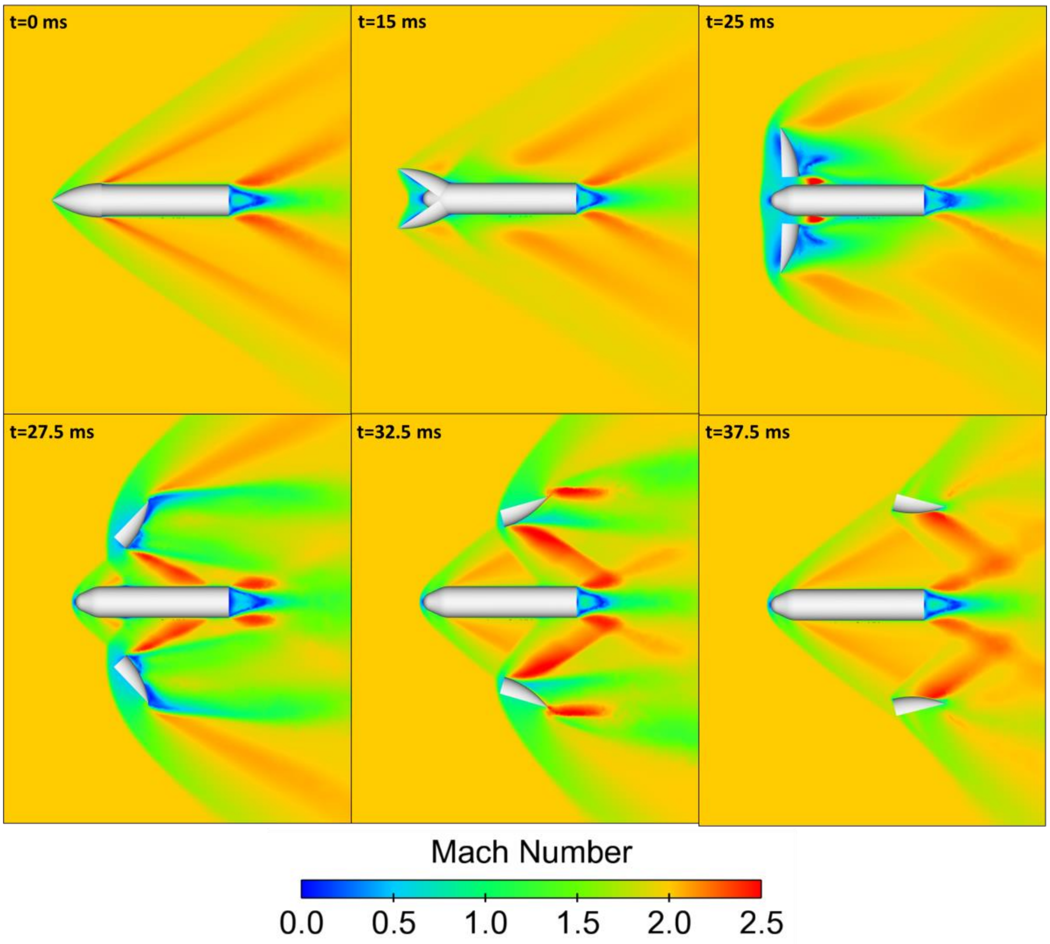

Figure 4.14 Top Views of Mach Number Contour for Shroud Separation (Altitude=5000 m, M=2.0, AOA=0° and Moment=1000 Nm)

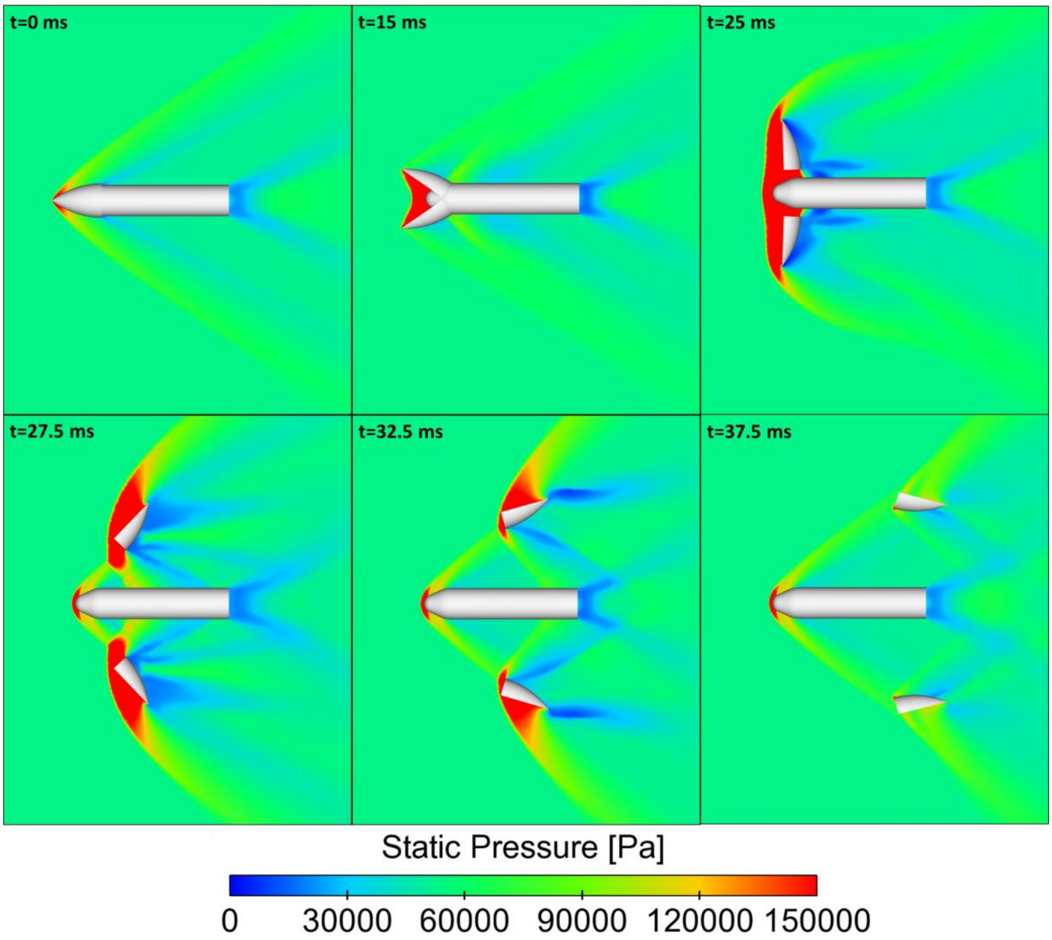

Figure 4.15 Top Views of Static Pressure Contour for Shroud Separation (Altitude=5000m, M=2.0, AOA=0° and Moment=1000 Nm)

After the shroud is released, it is strongly influenced by the flow field that is induced by the missile body. Pressure gradient distributions clearly show the complex shockwave interactions on the shroud and missile body and it can be seen in Figure 4.15. The influence is considerable at the area close to the missile's front. This implies that the influence is mostly due to shock waves created by the missile nose. In the near body case, sharp increase in pressure is observed at the missile nose area as opposed to the free-body case and a pressure decrease is observed at the same region. Consequently, a forward pushing force is acting on the shroud near the missile body, whereas the flow pressure at free flight produces significant drag.

Also similar shock pattern is observed in all other analyses results.

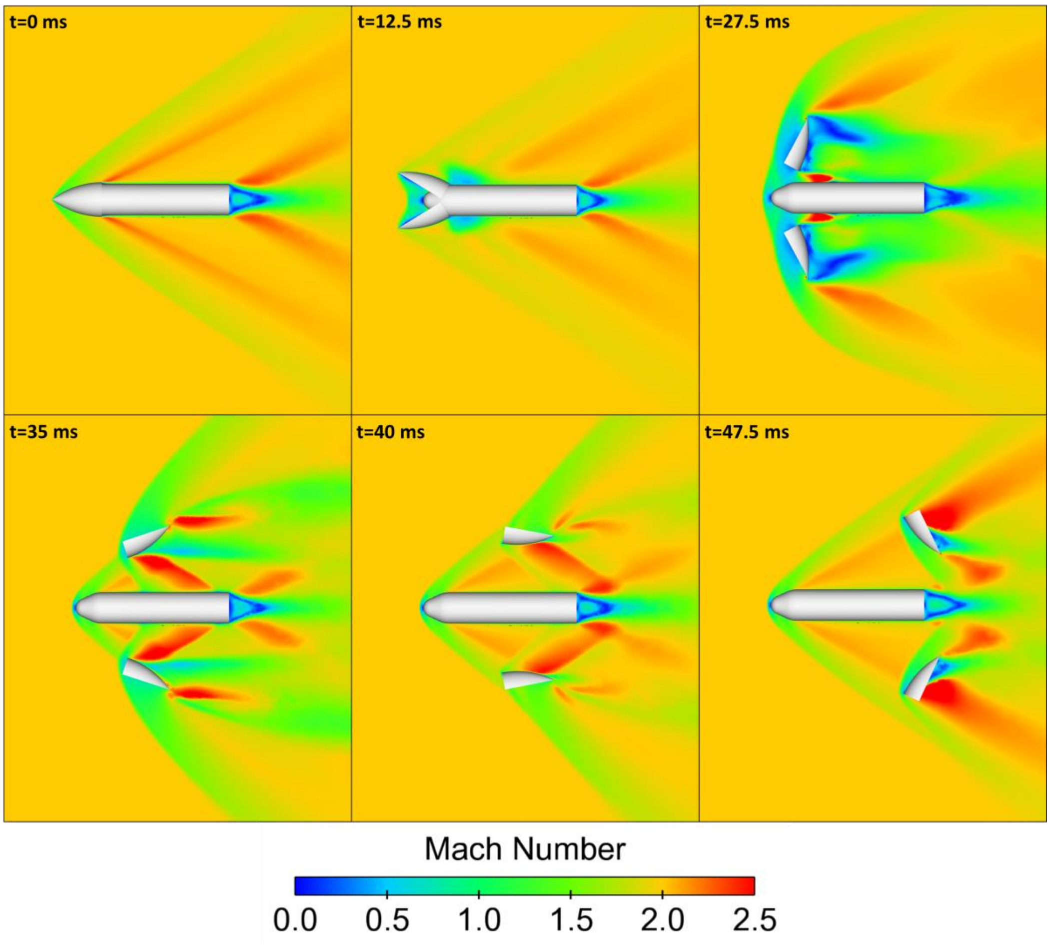

Figure 4.16 Top Views of Mach Number Contour for Shroud Separation (Altitude=7500 m, M=2.0, AOA=0° and Moment=1000 Nm)

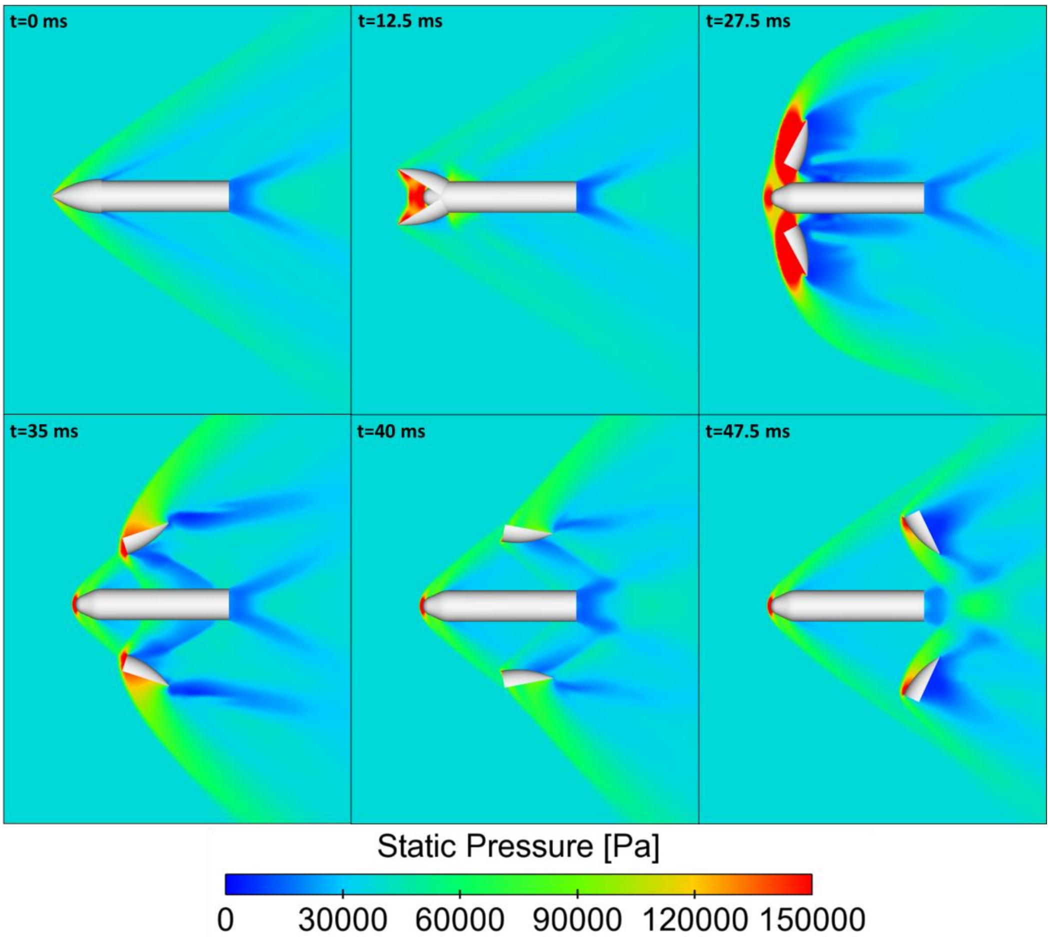

Figure 4.17 Top Views of Static Pressure Contour for Shroud Separation (Altitude=7500m, M=2.0, AOA=0° and Moment=1000 Nm)

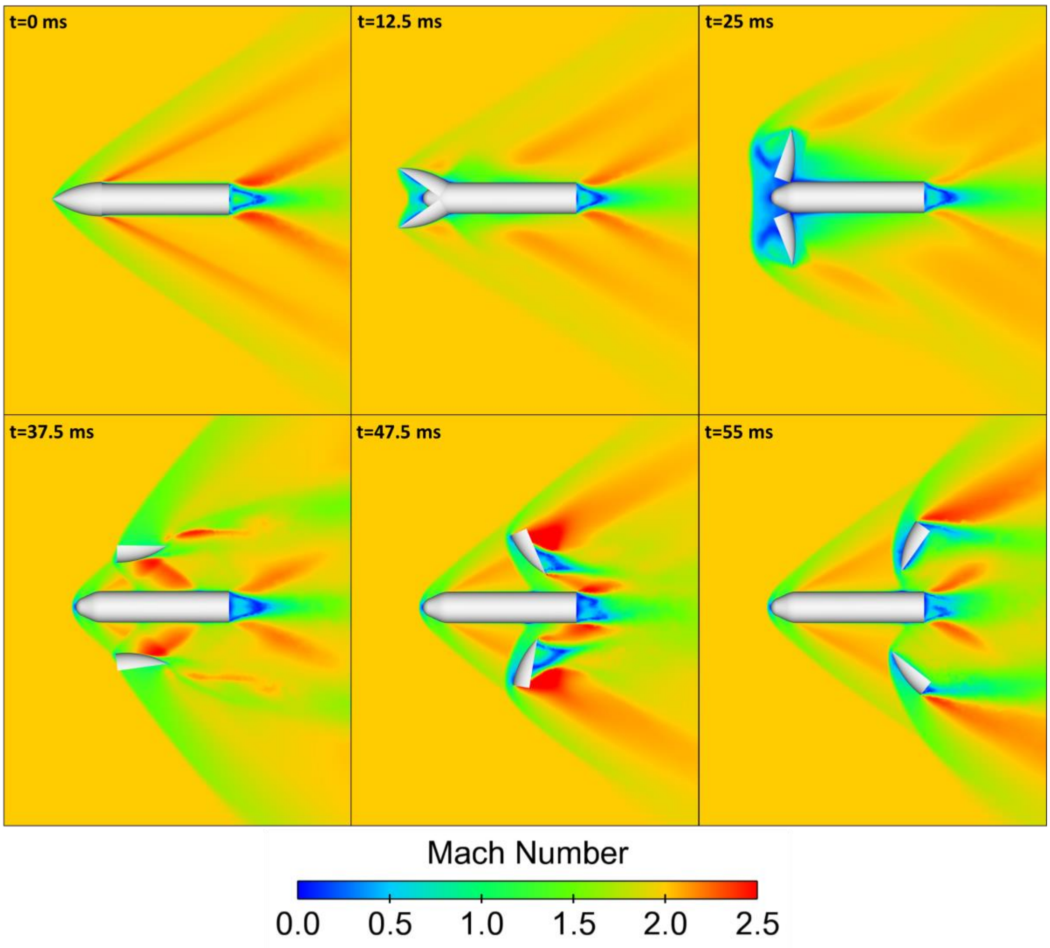

Figure 4.18 Top Views of Mach Number Contour for Shroud Separation (Altitude=10000 m, M=2.0, AOA=0° and Moment=1000 Nm)

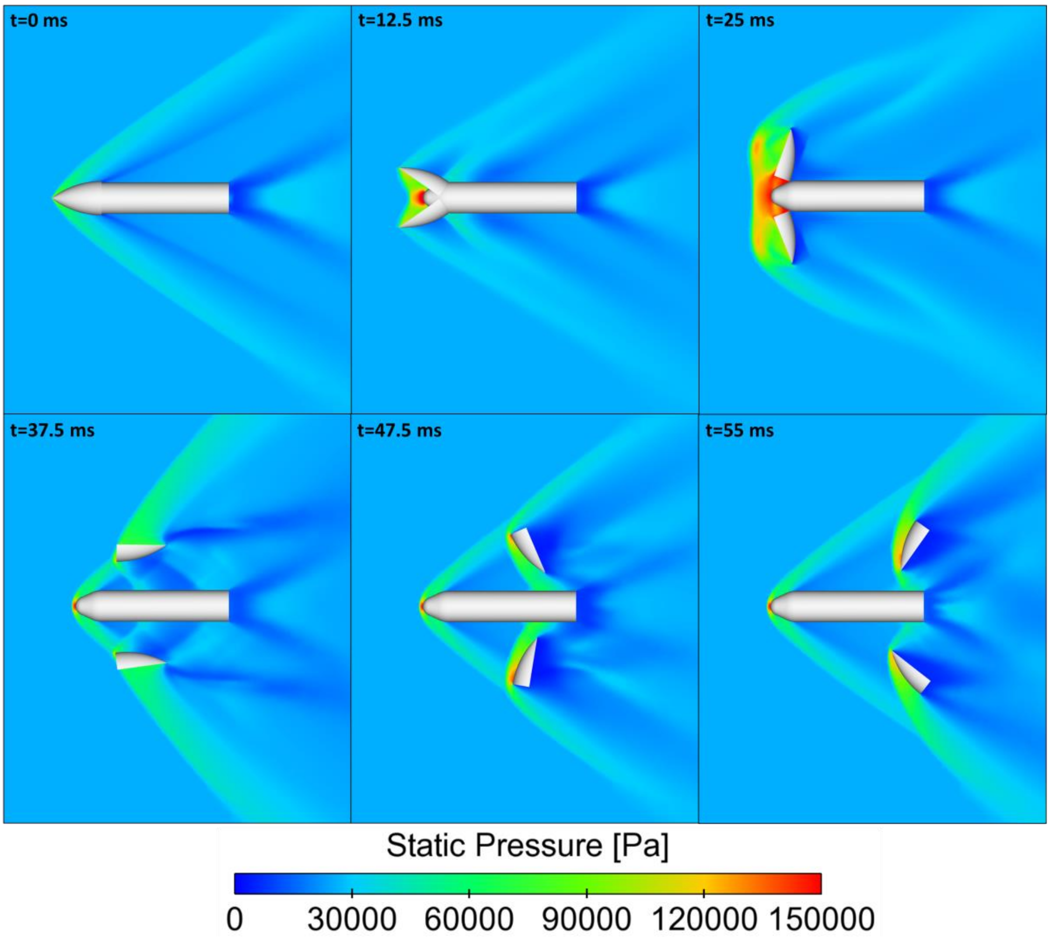

Figure 4.19 Top Views of Static Pressure Contour for Shroud Separation (Altitude=10000m, M=2.0, AOA=0° and Moment=1000 Nm)

4.6.2 Effects of Mach Number

In this part, effects of Mach number are investigated for the shroud separation. Shroud separation analyses are carried out for four different Mach numbers by keeping the altitude, angle of attack and ejection moment constant. Flight conditions and applied ejection moment are given in Table 4.5.

Table 4.5 Flight Conditions and Ejection Moment for Effect of Mach number

Altitude [m]	5000			
Mach Number	1.2	2	2.2	2.5
Angle of Attack [°]	0			
Ejection Moment [Nm]	1000			

Shroud trajectories belonging to three different Mach number are given in Figure 4.20. These trajectories show position change of center of gravity of shroud.

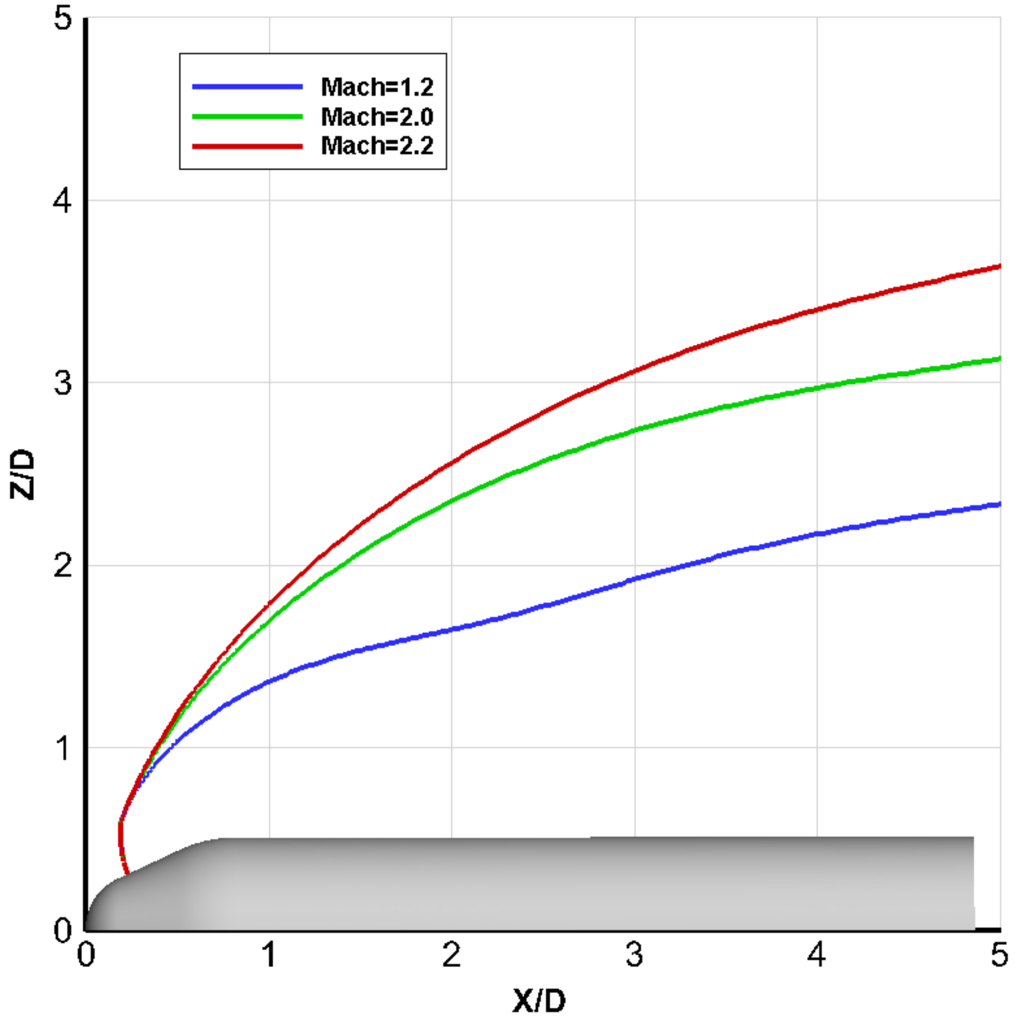

Figure 4.20 Shroud Trajectories for Different Mach Numbers

As it is shown in Figure 4.20, shroud separation is performed safely for the specified flight conditions and ejection moment at three different Mach numbers which are 1.2, 2.0 and 2.2. Also, 2.2 Mach number is the maximum Mach number, for which shroud separation can be initialized with 1000 Nm ejection moment. The shroud does not separate 2.5 Mach number because the ejection moment is not enough for the initialization of the separation. Besides, the closest shroud trajectory is followed for minimum Mach number and the furthest shroud trajectory is followed for maximum Mach number at which shroud can be separated. As the reason for this, it can be shown that Z force with respect to time for different Mach numbers in Figure 4.21.

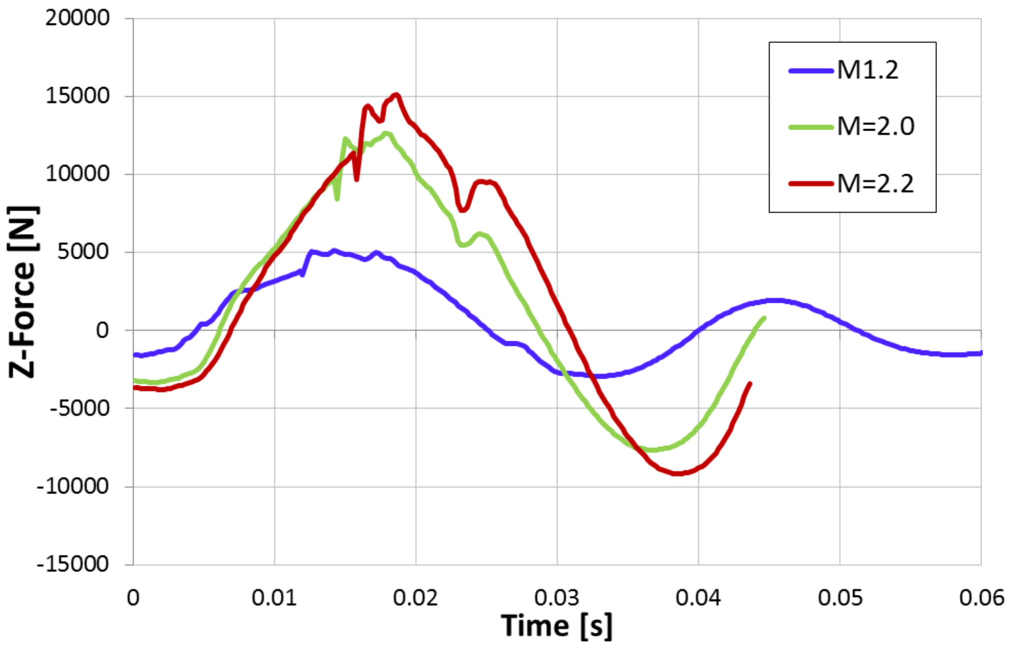

Figure 4.21 Z-Force Acting on the Shroud with Respect to Time for Different Mach Numbers

It is known that, as the Mach number decreases aerodynamic forces acting on the shroud covers decreases. In other words, it can be seen from Figure 4.21 that an increased Z force acting on the Z direction of the shroud covers determines with increasing Mach number. This phenomenon affects the trajectory of the shroud during separation. When the Z-Force of the shroud is higher, force acting on the Z direction that separates the shroud from missile becomes larger. Therefore, maximum separation distance for the shroud is obtained when Z-force of the shroud is the highest. Besides, increasing of the Mach number leads to increasing of the X-force acting on the X direction in Figure 4.22. Therefore, shroud covers reach the same position along the X direction in the shorter time.

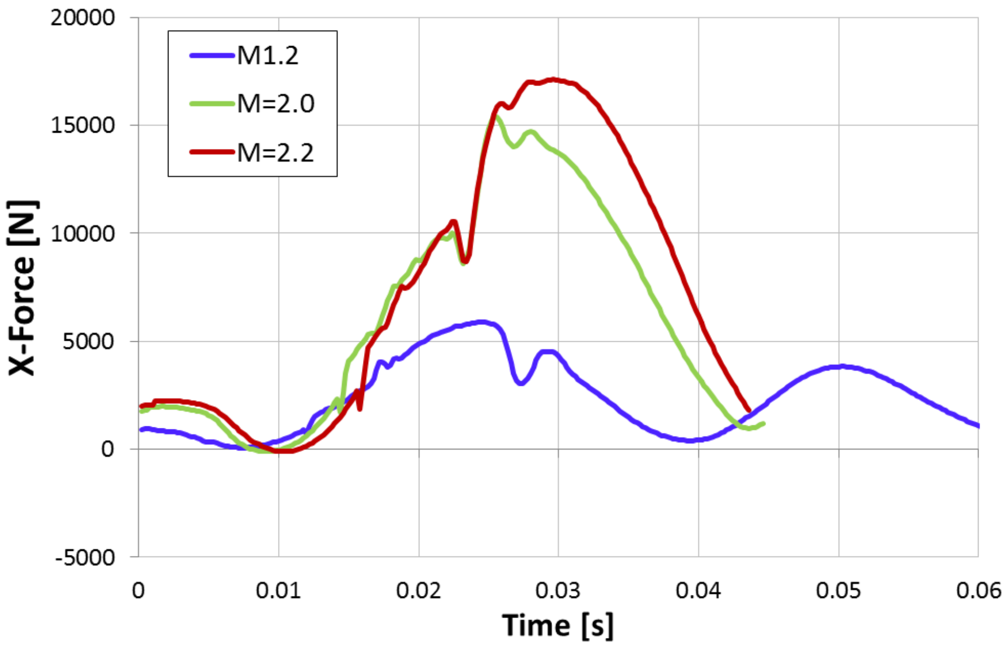

Figure 4.22 X-Force Acting on the Shroud with Respect to Time for Different Mach Numbers

These analyses show that under these conditions maximum Mach number for the safe separation of shroud is determined. In addition to that analyses show that larger ejection moment is desired for safe separation of shroud as seen with increasing Mach number. Also, summary of the shroud separation for effect of Mach number can be seen in Table 4.6.

Table 4.6 Summary of the Shroud Separation for Effect of Mach number

Mach Number=1.2	Safe Separation
Mach Number=2.0	Safe Separation
Mach Number=2.2	Safe Separation
Mach Number=2.5	Shroud Separation Failed

4.6.2.1 Solution Domain Flow Visualization

Mach number and static pressure contours for shroud separation are given in below figures.

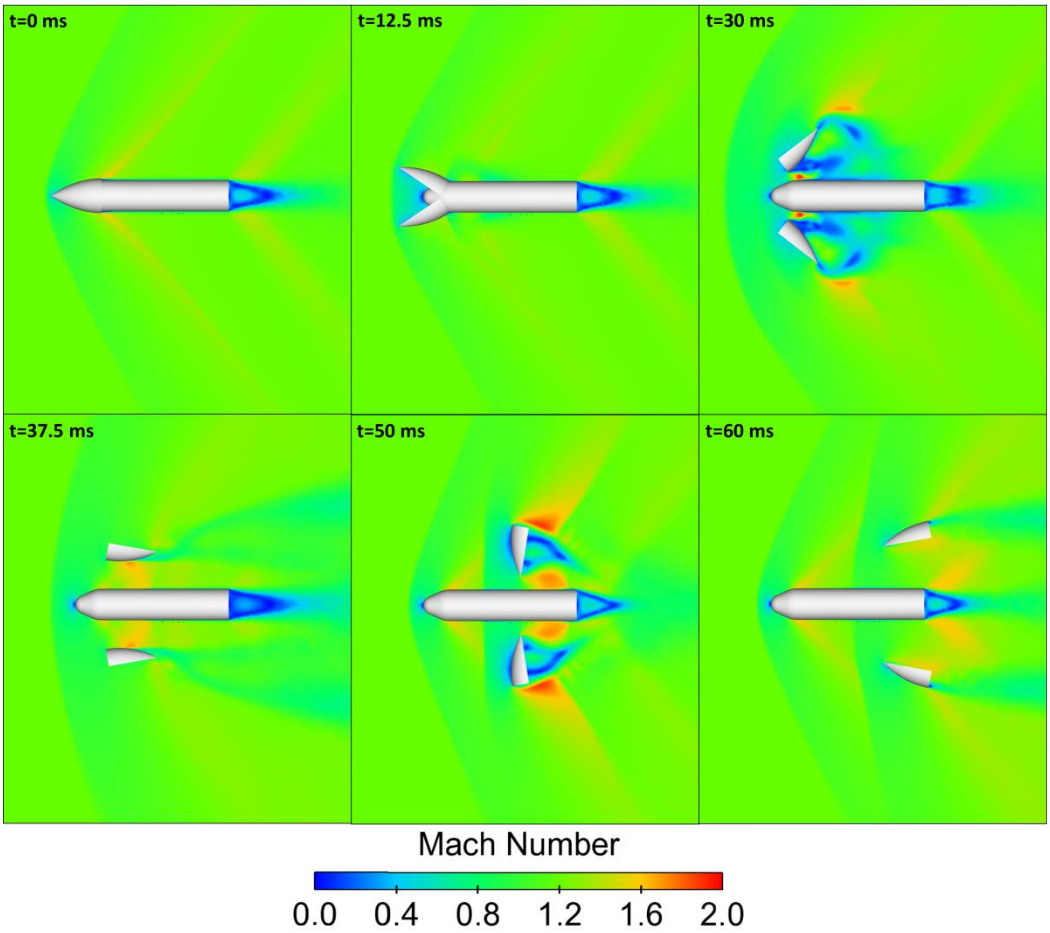

Figure 4.23 Top Views of Mach Number Contour for Shroud Separation (Altitude=5000m, M=1.2, AOA=0° and Moment=1000 Nm)

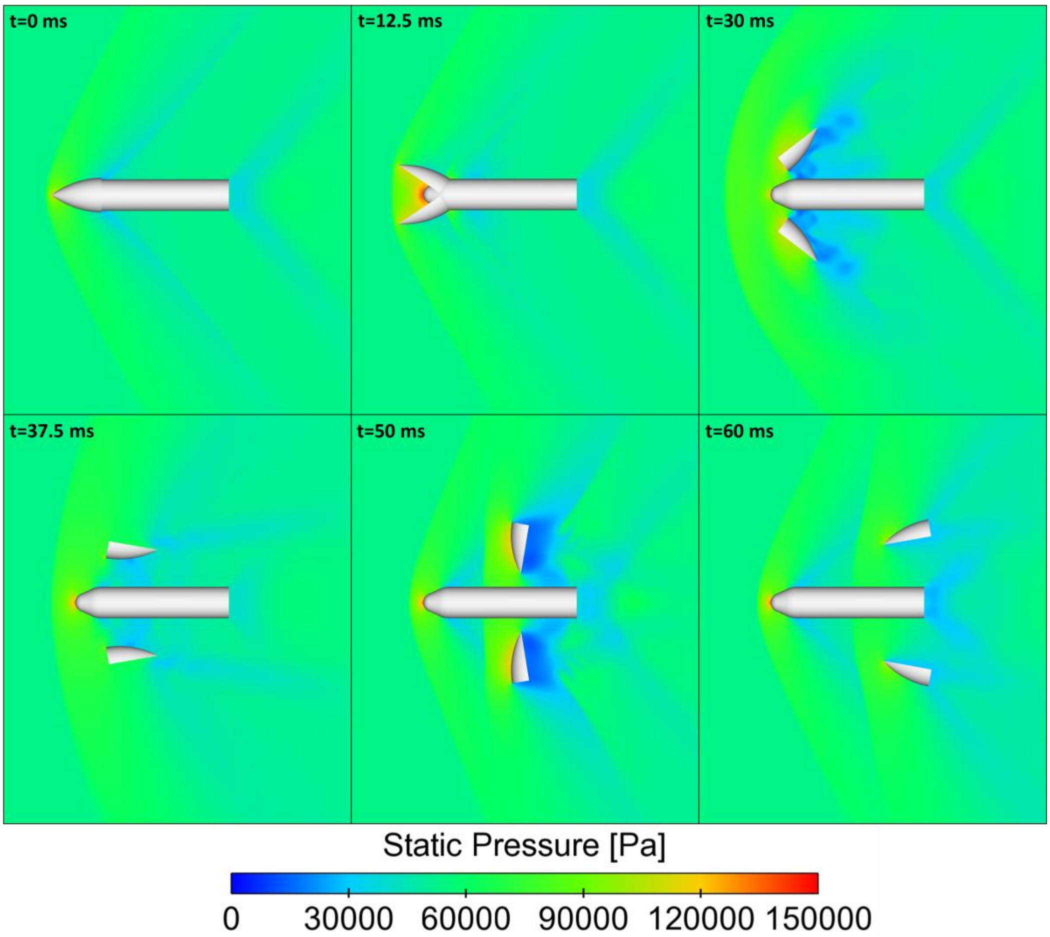

Figure 4.24 Top Views of Static Pressure Contour for Shroud Separation (Altitude=5000m, M=1.2, AOA=0° and Moment=1000 Nm)

4.6.3 Effects of Angle of Attack

In this part, effects of angle of attack are investigated for the shroud separation. Shroud separation analyses are carried out for three different angle of attacks by keeping the altitude, Mach number and ejection moment constant. Flight conditions and applied ejection moment are given in Table 4.7 for this part.

Table 4.7 Flight Conditions and Ejection Moment for Effect of Angle of Attack

Altitude [m]	5000		
Mach Number	2		
Angle of Attack [°]	0	10	20
Ejection Moment [Nm]	1000		

Shroud trajectories belonging to three different angle of attacks are given in Figure 4.25. These trajectories indicate position change of center of gravity of shroud.

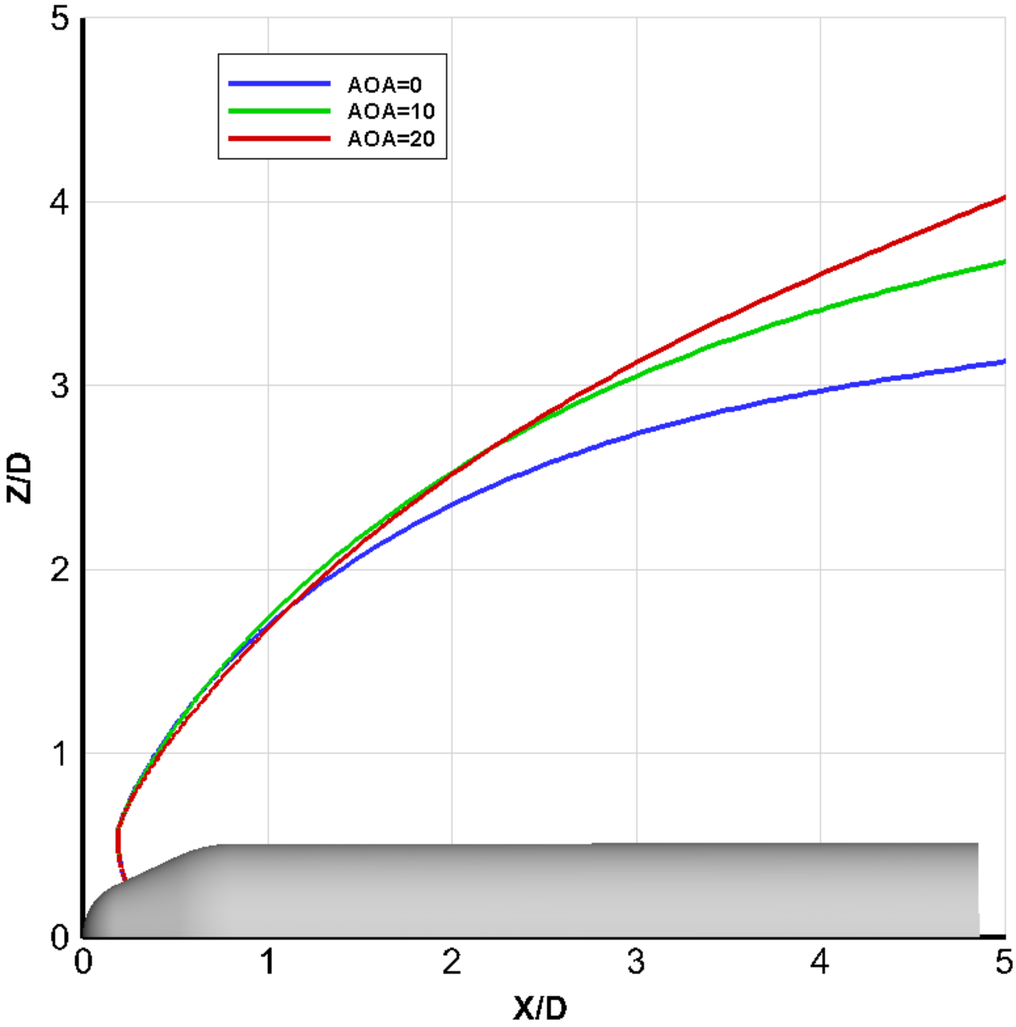

Figure 4.25 Shroud Trajectories for Different Angle of Attacks

As it is shown in above figure, in all angle of attacks shroud separation is performed safely for the specified flight conditions and ejection moment. Since angle of attack changes depending on the Y direction, it does not affect the shroud trajectories on Z direction dramatically. Therefore, shroud trajectories for different angle of attacks are similar up to 2 missile diameter in Z direction. In addition, as it is seen in Figure 4.26 and Figure 4.27, Z force and X force values with respect to time for different angle of attack are the similar during the separation.

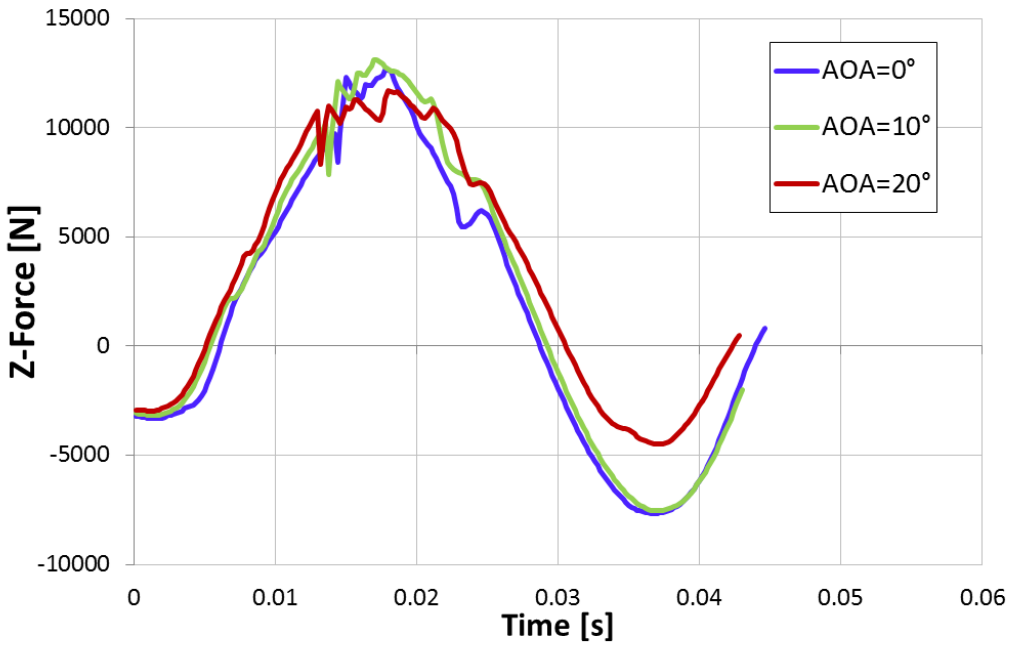

Figure 4.26 Z-Force Acting on the Shroud with Respect to Time for Different Angle of Attacks

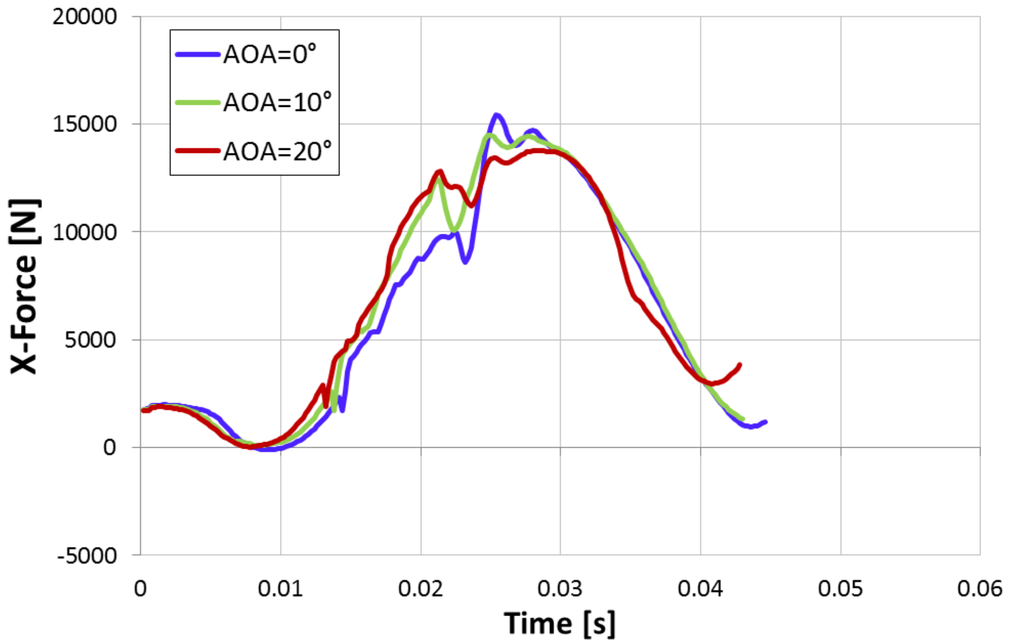

Figure 4.27 X-Force Acting on the Shroud with Respect to Time for Different Angle of Attacks

Also, summary of the shroud separation for effect of angle of attack can be seen in Table 4.8.

Table 4.8 Summary of the Shroud Separation for Effect of Angle of Attack

Angle of Attack=0°	Safe Separation
Angle of Attack=10°	Safe Separation
Angle of Attack=20°	Safe Separation

4.6.3.1 Solution Domain Flow Visualization

Mach number and static pressure contours for shroud separation are given in below figures.

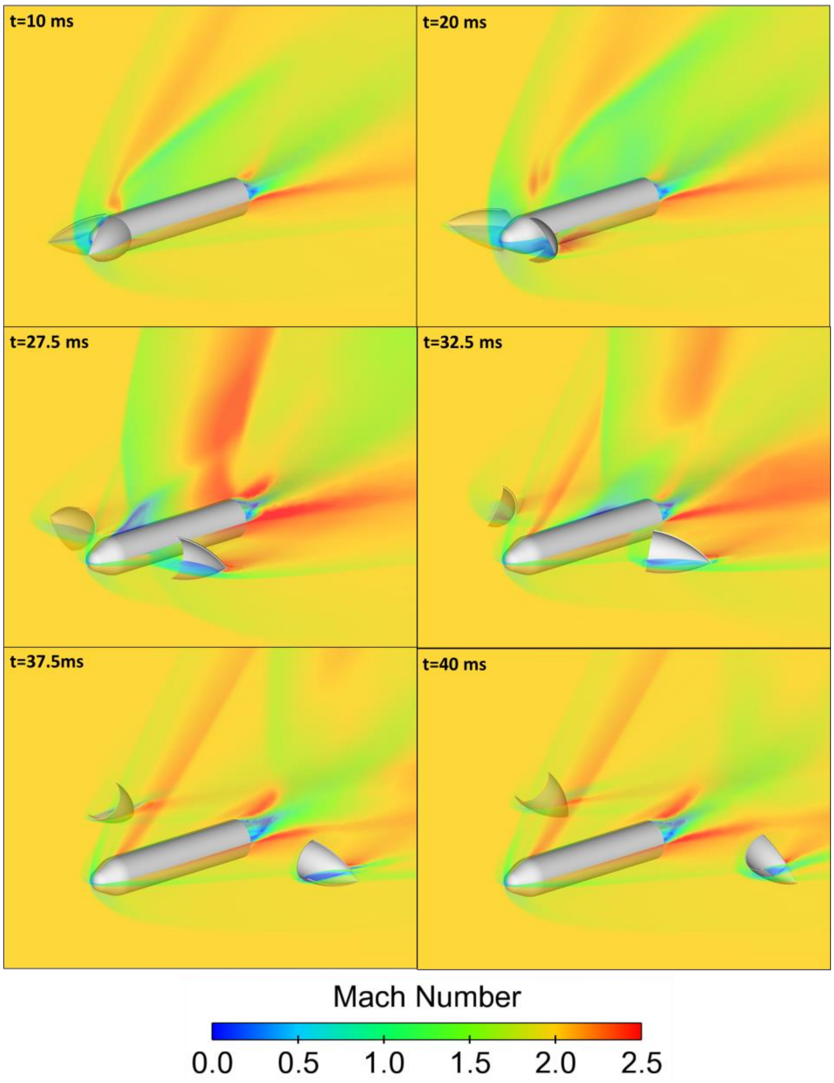

Figure 4.28 Perspective Views of Mach Number Contour for Shroud Separation (Altitude=5000 m, M=2.0, AOA=20° and Moment=1000 Nm)

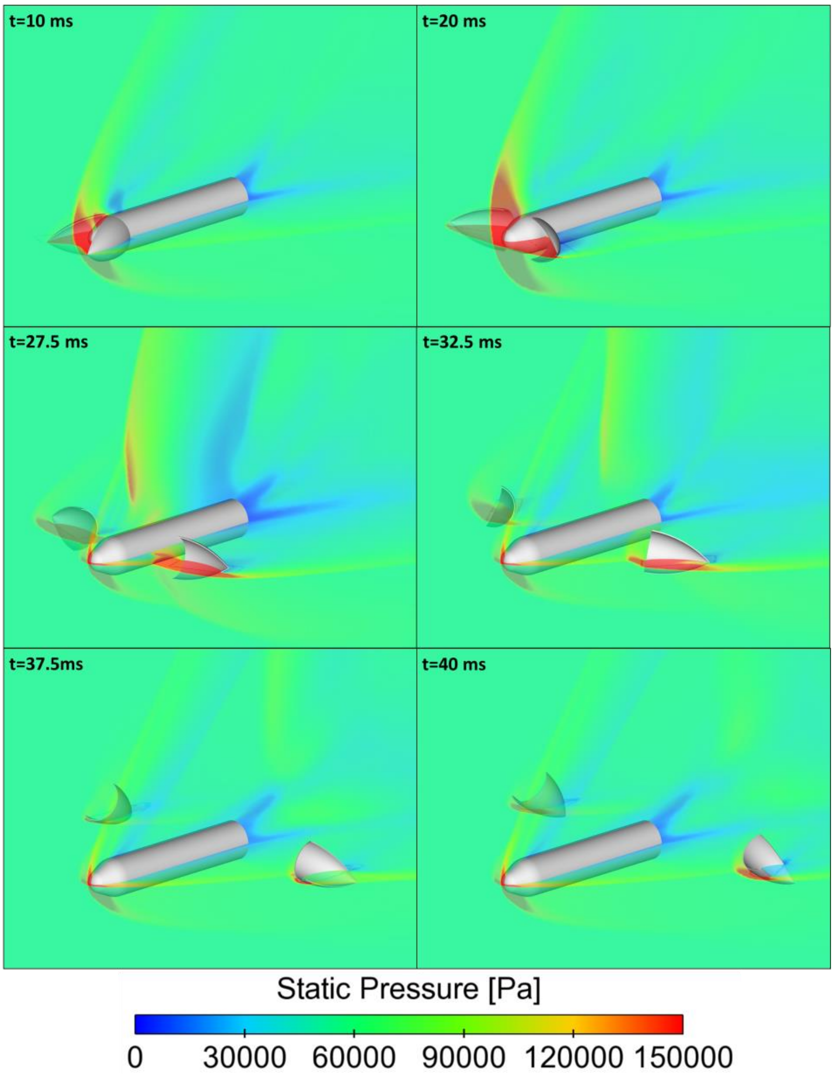

Figure 4.29 Perspective Views of Static Pressure Contour for Shroud Separation (Altitude=5000 m, M=2.0, AOA=20° and Moment=1000 Nm)

4.6.4 Effects of Ejection Moment

In this part, effects of ejection moment are investigated for the shroud separation. Shroud separation analyses are performed for four different ejection moment by keeping the flight conditions constant. Flight conditions and applied ejection moment are given in Table 4.9 for this part.

Table 4.9 Flight Condition and Ejection Moments for Effect of Ejection Moment

Altitude [m]	5000			
Mach Number	2			
Angle of Attack [°]	0			
Ejection Moment [Nm]	500	800	1000	1500

Shroud trajectories belonging to three different ejection moments are given in Figure 4.30. These trajectories display position change of center of gravity of shroud.

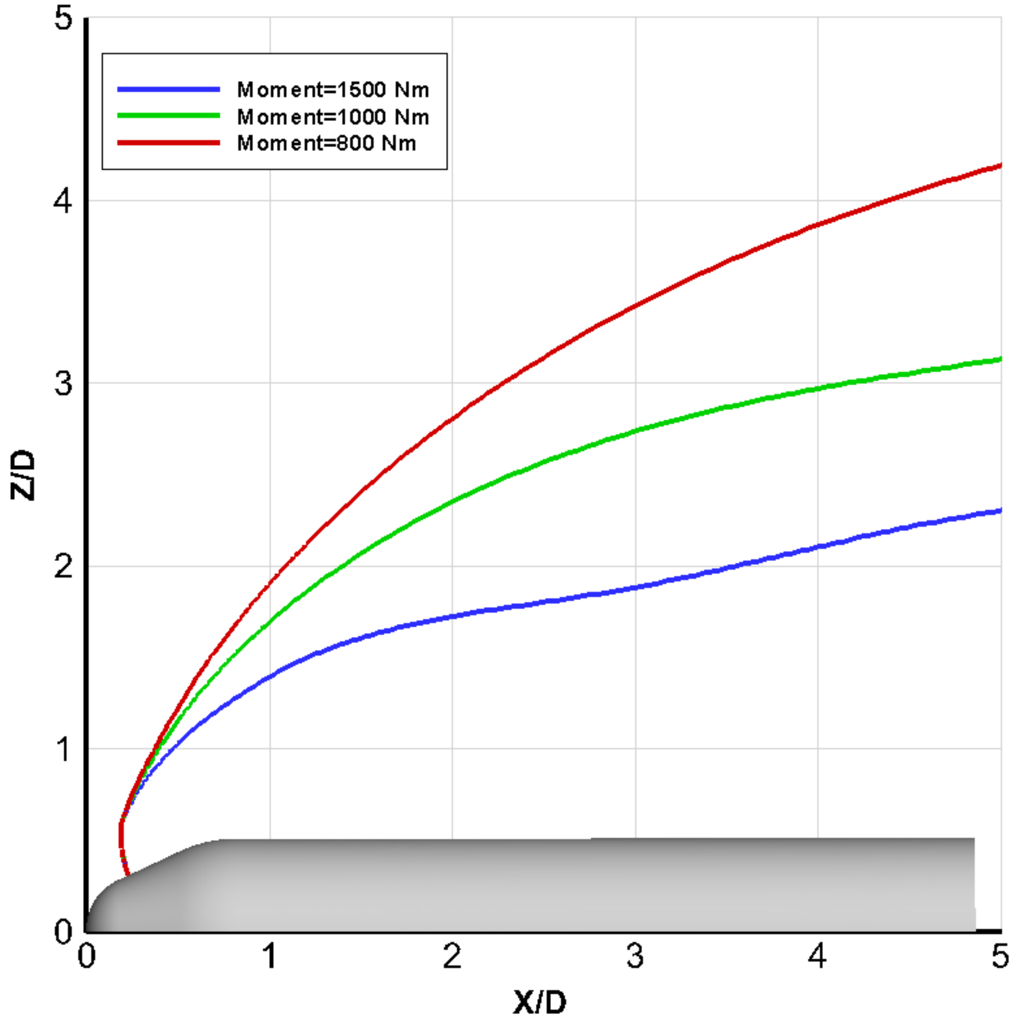

Figure 4.30 Shroud Trajectories for Different Ejection Moments

As it is shown in Figure 4.30, shroud separation is performed safely for the specified flight conditions and three different ejection moments which are 800 Nm, 1000 Nm, 1500 Nm. Also, 800 Nm ejection moment is the minimum ejection moment, for which shroud separation can be initialized at the respective flight condition. The shroud does not separate with 500 Nm ejection moment because the ejection moment is not enough for the initialization of the separation at this flight condition. Besides, the closest shroud trajectory is followed for maximum ejection moment and the furthest shroud trajectory is followed for minimum ejection moment which shroud can be separated. As the reason for this, it can be shown that pitch angle changes with respect to time for different ejection moments in Figure 4.31.

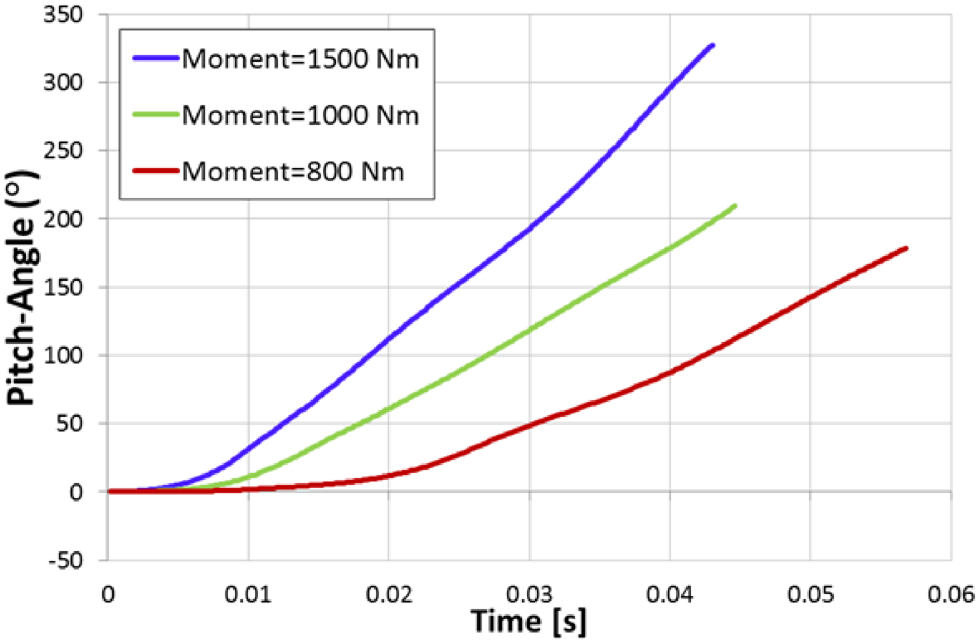

Figure 4.31 Shroud Pitch Angle Change with Respect to Time for Different Ejection Moments

As it is shown in above figure, higher pitch rate creates higher rotational inertia on the shroud covers. Therefore shroud covers which were separated with greater ejection moment, rotate faster. In this way, aerodynamic forces acting on the shroud on the Z-direction decreases faster and it can be seen in Figure 4.32. This phenomenon affects the trajectory of the shroud during separation.

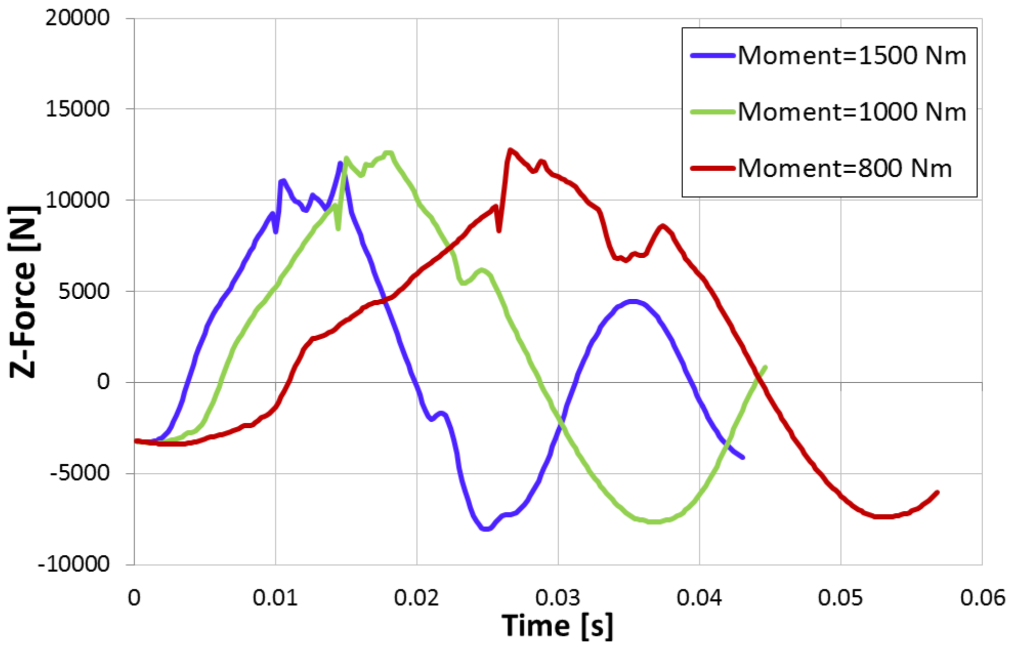

Figure 4.32 Z Force Acting on the Shroud with Respect to Time for Different Ejection Moments

As a result increasing the ejection moment leads to shroud covers following a close trajectory. Also, summary of the shroud separation for effect of angle of attack can be seen in Table 4.10.

Table 4.10 Summary of the Shroud Separation for Effect of Ejection Moment

Ejection Moment=500 Nm	Shroud Separation Failed
Ejection Moment=800 Nm	Safe Separation
Ejection Moment=1000 Nm	Safe Separation
Ejection Moment=1500 Nm	Safe Separation

4.6.4.1 Solution Domain Flow Visualization

Mach number and static pressure contours for shroud separation are given in below figures.

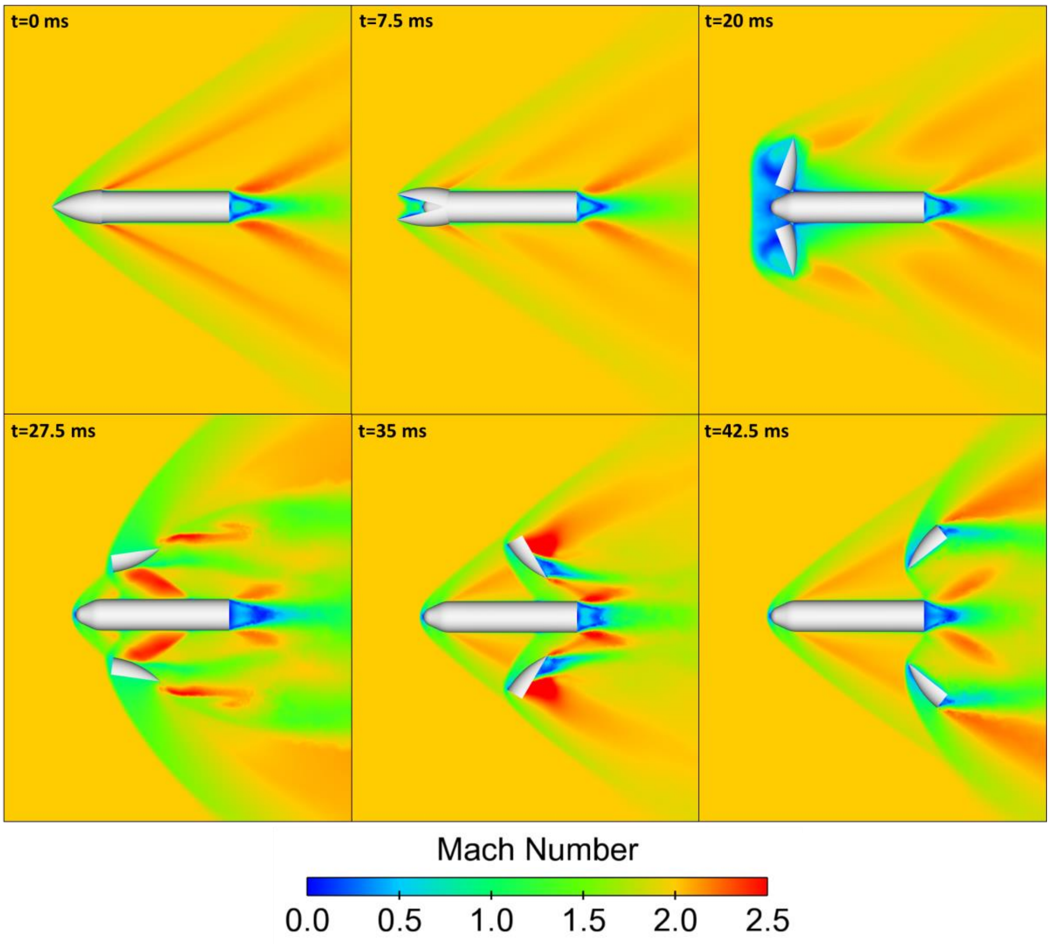

Figure 4.33 Top Views of Mach Number Contour for Shroud Separation (Altitude=5000 m, M=2.0, AOA=0° and Moment=1500 Nm)

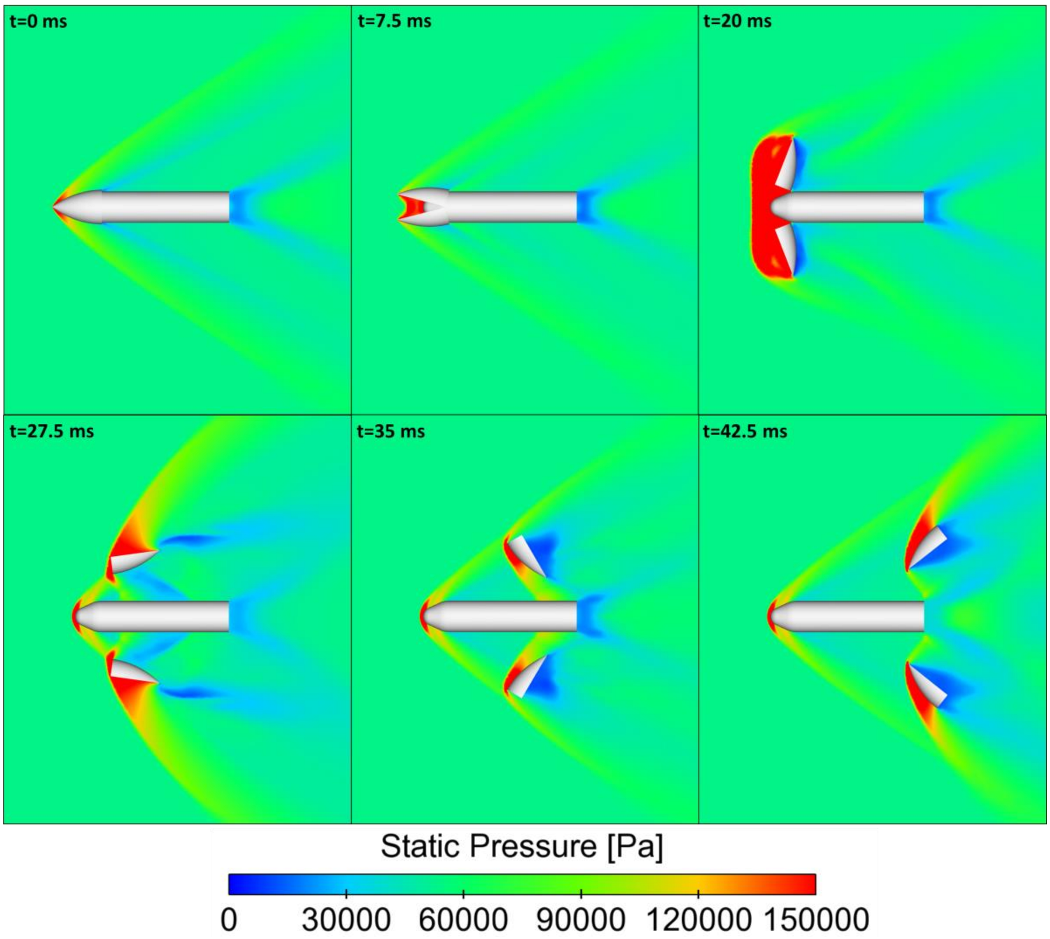

Figure 4.34 Top Views of Static Pressure Contour for Shroud Separation (Altitude=5000 m, M=2.0, AOA=0° and Moment=1500 Nm)

4.6.5 Effects of Side-Slip Angle

In this part, effects of side-slip angle are investigated for the shroud separation. Shroud separation analyses are carried out for two different side-slip angles by keeping the altitude, Mach number and ejection moment constant. Flight conditions and applied ejection moment are given in Table 4.11 for this part.

Table 4.11 Flight Conditions and Ejection Moment for Effects of Side-Slip Angle

Altitude [m]	5000	
Mach Number	2	
Side-Slip Angle [°]	0	5
Ejection Moment [Nm]	1000	

Shroud trajectories belonging to two different side-slip angles are given in Figure 4.35. These trajectories reflect position change of center of gravity of shroud.

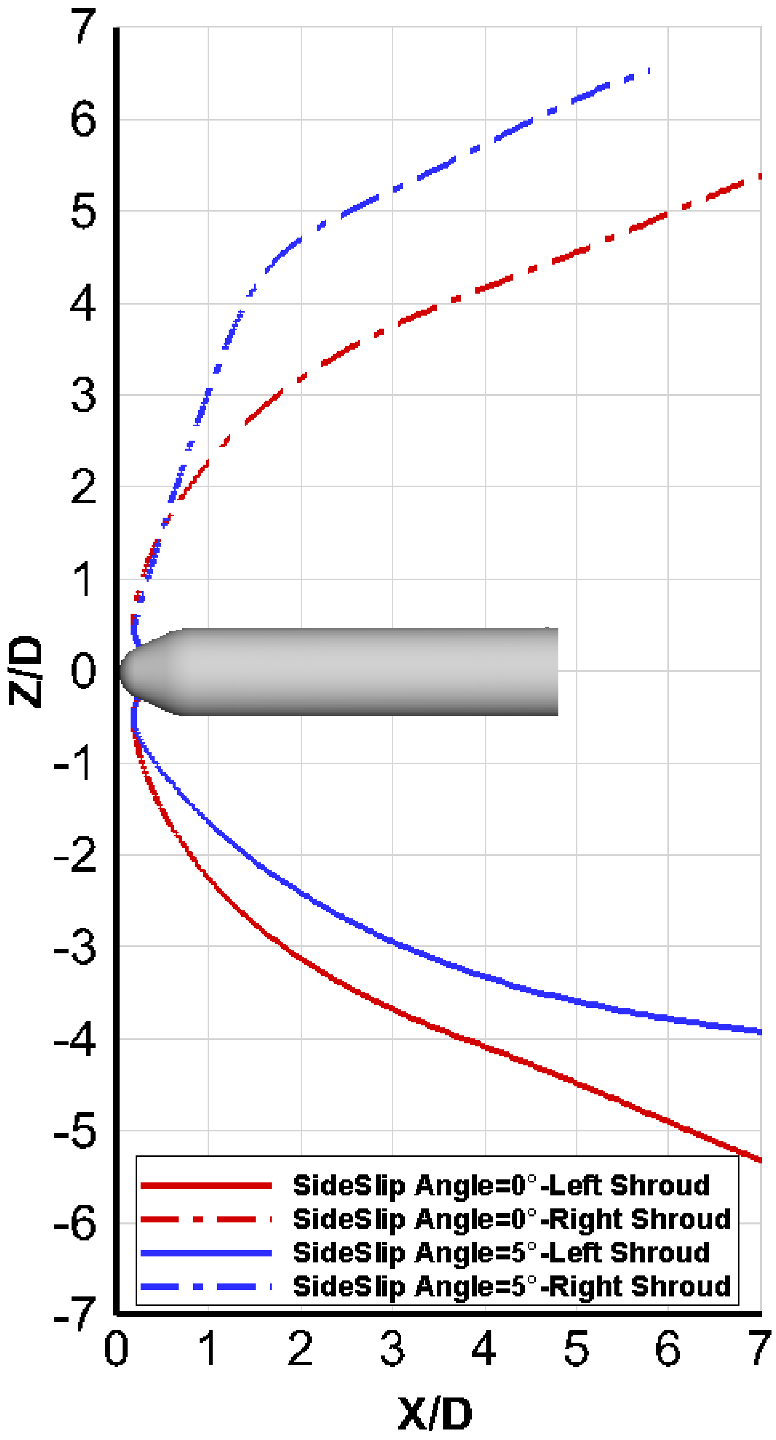

Figure 4.35 Shroud Trajectories for Different Side-Slip Angles

As it is shown in Figure 4.35, in all side-slip angles shroud separation is performed safely for the specified flight conditions and ejection moment. Since side-slip angle changes depending on the Z direction, it affects the shroud trajectories on Z direction dramatically. When the missile has side-slip angle, shroud trajectories are not symmetrical. In addition, as it is seen in Figure 4.36 and Figure 4.37, Z force and X force values with respect to time are asymmetrical for each shroud component (left/right) at non-zero side-slip angle whereas symmetrical Z-force and same X-force values are obtained at zero side-slip angle.

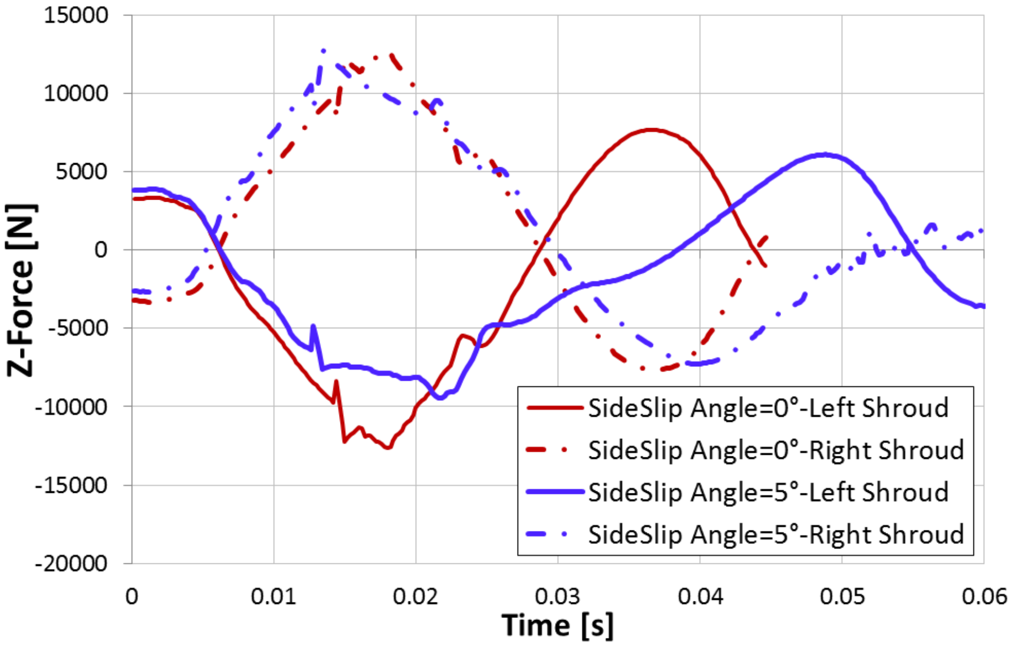

Figure 4.36 Z-Force Acting on the Shroud with Respect to Time for Different Side-Slip Angle

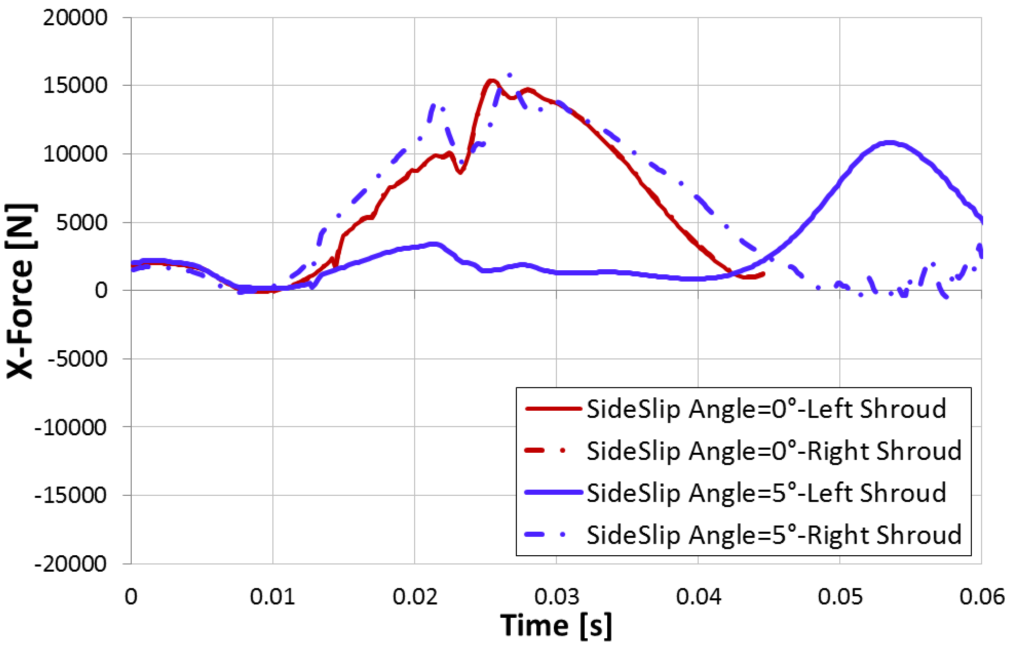

Figure 4.37 X-Force Acting on the Shroud with Respect to Time for Different Side-Slip Angle

Also, summary of the shroud separation for effect of side-slip angle can be seen in Table 4.12.

Table 4.12 Summary of the Shroud Separation for Effect of Side-Slip Angle

Side-Slip Angle=0°	Safe Separation
Side-Slip Angle =5°	Safe Separation

4.6.5.1 Solution Domain Flow Visualization

Mach number and static pressure contours for shroud separation are given in below figures.

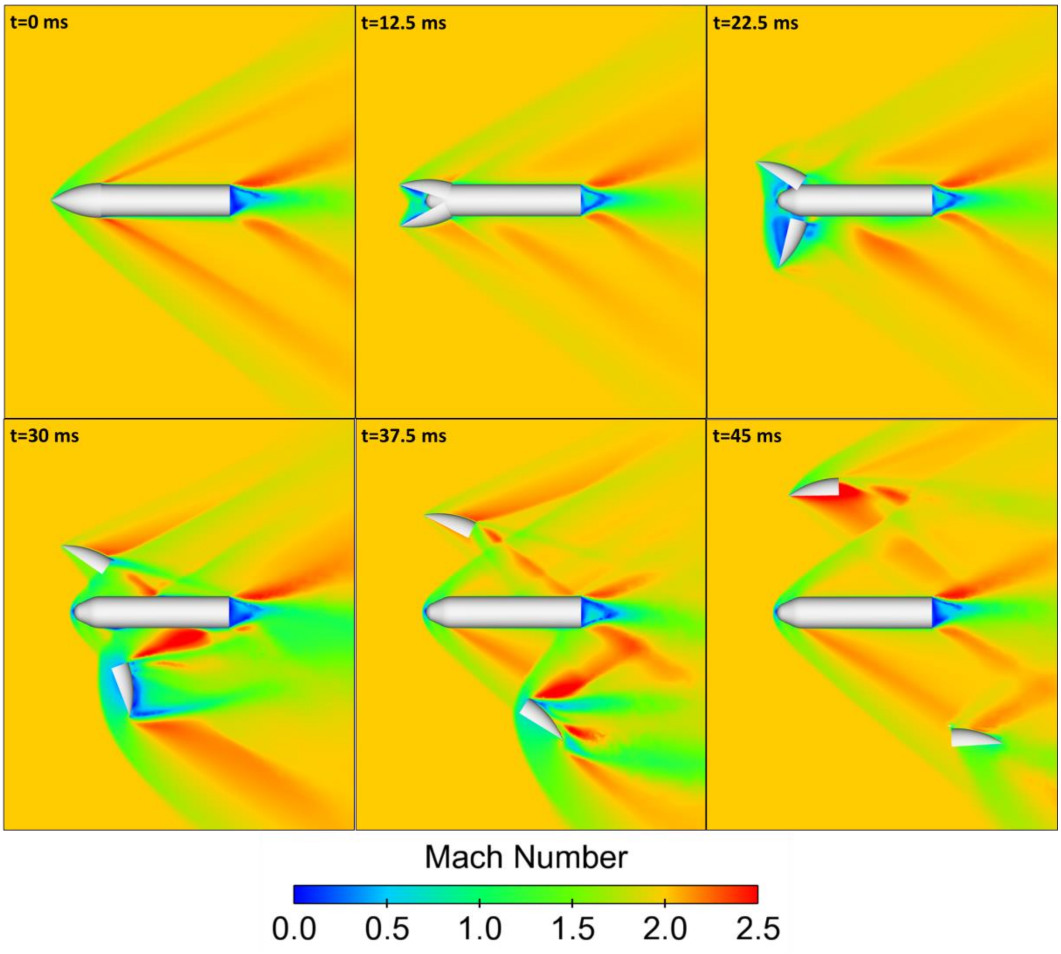

Figure 4.38 Top Views of Mach Number Contour for Shroud Separation (Altitude=5000 m, M=2.0, Side-Slip Angle=5° and Moment=1000 Nm)

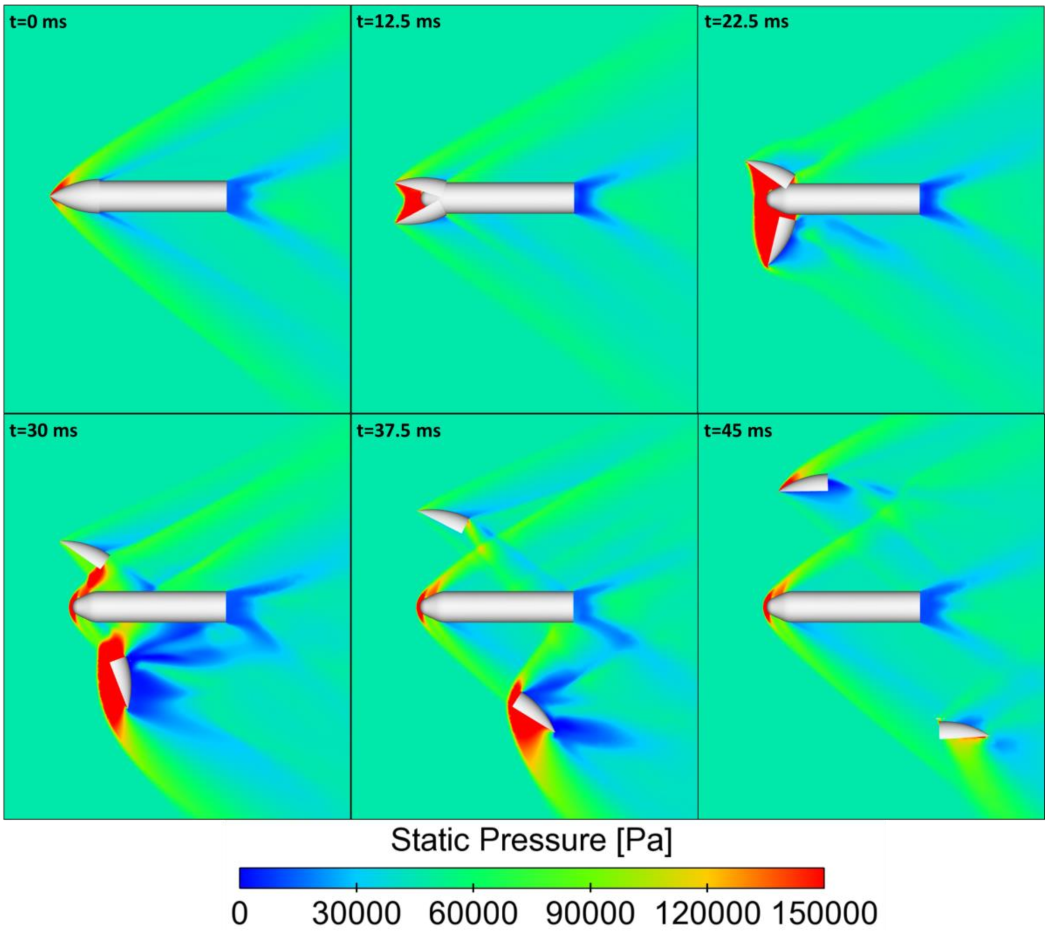

Figure 4.39 Top Views of Static Pressure Contour for Shroud Separation (Altitude=5000 m, M=2.0, Side-Slip Angle=5° and Moment=1000 Nm)

4.6.6 Effects of Aerodynamic Loads Acting on the Missile During Separation

The effects of time dependent variation of aerodynamic forces and moments on missile during shroud separation are investigated. CFD analysis results were used to investigate these changing effects on the missile for a definite flight condition and ejection moment. Applied ejection moment and flight condition can be given in Table 4.13 for this study.

Table 4.13 Flight Conditions and Ejection Moment for Effects of Aerodynamic Loads Acting on the Missile During Separation

Altitude [m]	5000
Mach Number	2
Angle of Attack [°]	0
Ejection Moment [Nm]	1000

X-force changing acting on each component of missile and total X-force in time was given below figure.

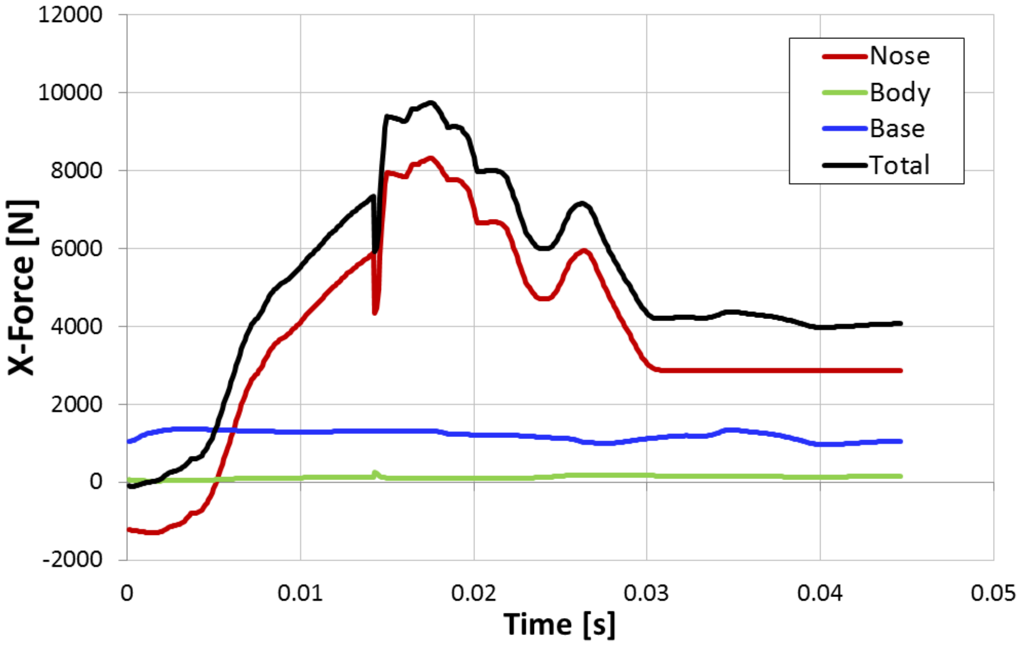

Figure 4.40 X-Force Acting on the Missile Part During Separation with Respect to Time

As seen in Figure 4.40, missile nose is most affected compared to missile body and base during separation. Therefore X-force acting on missile nose becomes more important for structural analysis during separation. These results should be taken into account in the structural analysis of the missile nose.

In addition it is mentioned that shroud covers decrease axial force acting on missile and shroud covers protect the missile nose from significant aerodynamic heating and high recovery temperature. Also X-force acting on missile with/without shroud is given in Figure 4.41.

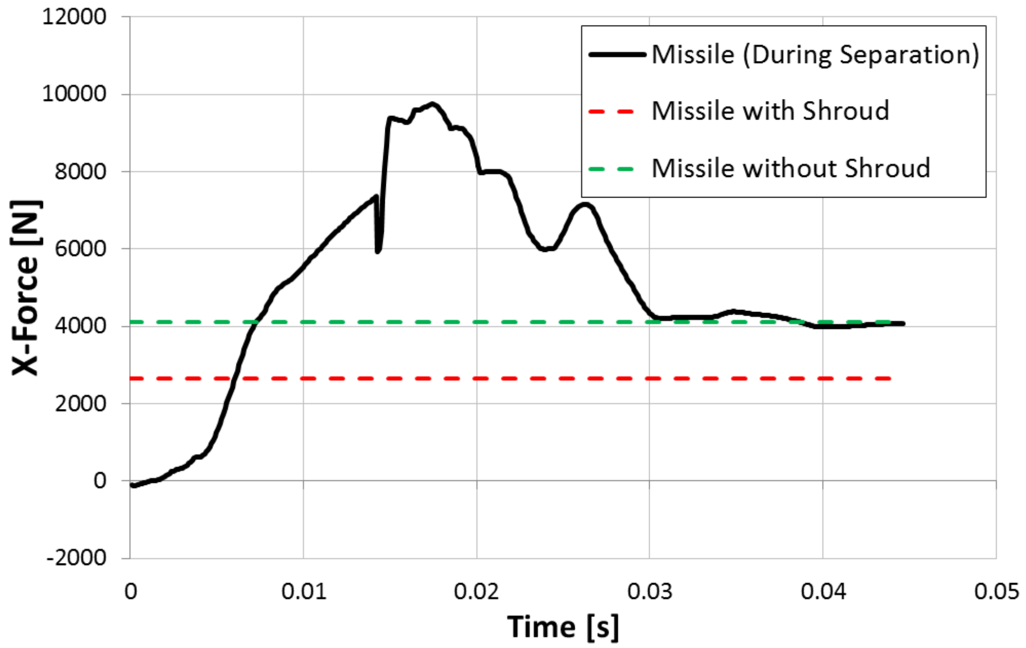

Figure 4.41 X-Force Acting on the Missile with Respect to Time

As seen in above figure, missile with shroud has lower axial force compared to missile without shroud. Therefore missile with shroud is useful for range of missile for same missile system. Variation of axial force acting on missile during separation is also given in Figure 4.41.

CHAPTER 5

CONCLUSION

In this thesis, CFD analysis of shroud separation on a generic missile was performed to investigate safe separation of the shroud covers from missile for different parameters which are altitude, Mach number, angle of attack, side-slip angle and ejection moment by using commercial code CFD++. Firstly the subject was introduced secondly methodology and governing equations used in the study were clarified, thirdly analysis for test cases was carried on and compared with experiment and finally a multi body CFD analysis approach was applied to shroud separation on generic missile.

EGLIN store separation and HB test cases were used for CFD solver validation analyses. Prior to shroud separation analyses, grid independence and turbulence model selection studies were performed to get accurate results for multi body CFD analyses. Aerodynamic coefficients were compared with experimental data for the HB test case. Normal force coefficient, pitch moment coefficient and axial force coefficient were in good agreement with the experimental data. Also the store separation analysis results were compared with experimental data. Store position and store angle were in very good agreement with experiment. Solution of these two test cases and the compared results showed that the commercial CFD++ solver could be applicable for multi body CFD analysis problems.

As a result of all this validation, the parametric study for shroud separations from generic missile was studied and results of CFD simulation were presented. Shroud trajectories were examined for different flight conditions and ejection moments.

Flight conditions and ejection moments for safe separation were determined for the model used in analyses. Analyses results show that as the altitude increases, shroud follows a trajectory close to missile body because of the decreasing aerodynamic force. As the Mach number increases, shroud follows a trajectory that is further away from missile body because of increasing the aerodynamic force. Angle of attack does not affect shroud separation trajectory dramatically because angle of attack and separation axis are different. Side-slip angle affects shroud separation trajectory because side-slip angle and separation axis are same. Therefore, side-slip angle effects should be taken into account while defining the ejection moment for safe separation. As the ejection moment value increases, shroud follows a trajectory close to missile body for same flight condition. Finally, effects of aerodynamic loads acting on the missile during separation are important for structural analysis of the missile nose. Therefore, these effects should be taken into account in the design phases.

In conclusion, by using modeling techniques applied in this study, it is possible to determine necessary ejection moment and separation trajectory of an arbitrary shroud design with different shapes and materials at given flight conditions. In the same manner for a given ejection moment, the flight envelop that enables safe separation of shroud from missile can be determined.

REFERENCES

[1] Y. Dagan and E. Arad, "Analysis of Shroud Release Applied for High-Velocity Missiles," *Journal of Spacecraft and Rockets,* 2014.

[2] M. Oswald, D. S. Eder, K. Weinand, D. Stern and W. Zeiss, "Shroud Separation Study Using The Six-Degree-of-Freedom Approach For High Mach Numbers," AIAA Multinational BMD Conference and Exhibition, Honolulu, 8-11 September, 2008.

[3] L. E. Lijewski and N. E. Suhs, "Time-Accurate Computational Fluid Dynamics Approach to Transonic Store Separation Trajectory Prediction," *Journal of Aircraft,* vol. 31, pp. 886-891, July 1994.

[4] J. D. Garay, "Summary Report On Aerodynamic Characteristics Of Standart Models HB-1 and HB-2," July 1964.

[5] I. Whalley, "Development of the STARS II Shroud Separation System," 37th AIAA/ASME/SAE/ASEE Joint Propulsion Conference, Utah, 8-11 July, 2001.

[6] A. D. Panetta, H. T. Nagamatsu, L. N. Myrabo, M. A. Minucci, D. G. Messitt and T. E. Dominick, "Drag of Shroud Deployment Bladder at Mach Numbers of 8 to 20," AIAA, 1999.

[7] K. Anandhanarayanan, "Grid-Free Kinetic Upwind Solver on Chimera Cloud of Points," West-East Speed Flow Field Conference, Moscow, 19-22 November, 2007.

[8] S. B. Lumb, "Transient Aerodynamics of a High Dynamic Pressure Shroud Separation for a Ground-Based Interceptor Missile," Alabama, 19-21 May 1992.

[9] L. Resch, C. Decesaris and E. Hedlund, "The Naval Surface Warface Center Hypervelocity Wind Tunnel 9 Hypersonic Shroud Separation Testing Capability," AIAA 30th Aerospace Sciences Meeting and Exhibit, Nevada, 6-9 January, 1992.

[10] P. A. Cavallo and S. M. Dash, "Aerodynamics of Multi-Body Separation Using Adaptive Unstructured Grids," AIAA 18th Applied Aerodynmamics Conference, Denver, 14-17 August, 2000.

[11] M. Hughson, "A 3-D Unstructured CFD Method for Maneuvering Vehicles," Mississippi State University, December, 1998.

[12] F. M. White, "Viscous Fluid Flow," McGraw and Hill, 1991.

[13] "CFD++ User Manual-Version 10.1".

[14] J. Blazek, "Computational Fluid Dynamics: Principles and Applications," 2001.

[15] E. N. Ferry, J. Sahu and K. R. Heavey, "Navier-Stokes Computations of Sabot Discard Using a Chimera Scheme," AIAA, 1998.

[16] Ö. H. Demir, "Computational fluid Dynamics Analysis of Store Separation," Ms. Thesis, METU, 2004.

[17] S. J. Zhang and S. F. Owens, "A Parallel Unstructured Chimera Grid Method," AIAA 17th Computational Fluid Dynamics Conference, Toronto, 6-9 June, 2005.

[18] S. J. Zhang, J. Liu, Y. S. Chen and X. Zhao, "Numerical Simulation of Stage Separation with an Unstructured Chimera Grid Method," AIAA 22nd Applied Aerodynamics Conference and Exhibit, Providence, 16-19 August 2004.

[19] E. R. Heim, "CFD Wing/Pylon/Finned Store Mutual Interference Wind Tunnel Experiment," September 10-17 1990.